SURFACTANT-ENHANCED GALLIUM ARSENIDE (111) EPITAXIAL GROWTH FOR QUANTUM PHOTONICS

SURFACTANT-ENHANCED GALLIUM ARSENIDE (111) EPITAXIAL GROWTH FOR QUANTUM PHOTONICS

BY

AHMED M. HASSANEN, B.Sc.

A THESIS
SUBMITTED TO THE DEPARTMENT OF ENGINEERING PHYSICS
AND THE SCHOOL OF GRADUATE STUDIES
OF MCMASTER UNIVERSITY
IN PARTIAL FULFILMENT OF THE REQUIREMENTS
FOR THE DEGREE OF
MASTER OF APPLIED SCIENCE

© Copyright by Ahmed M. Hassanen, September 2021

All Rights Reserved

Master of Applied Science (2021) McMaster University
(Engineering Physics) Hamilton, Ontario, Canada

TITLE:	Surfactant-enhanced Gallium Arsenide (111) Epitaxial Growth for Quantum Photonics
AUTHOR:	Ahmed M. Hassanen B.Sc. (Ain Shams University, Egypt)
SUPERVISOR:	Dr. Ryan B. Lewis
NUMBER OF PAGES:	xix, 156

Abstract

In this thesis, the effect of surfactants (Bi /Sb) on GaAs(111) is explored, particularly in regards to modifying the surface morphology and growth kinetics. Both molecular beam epitaxy (MBE) and metal-organic chemical vapour deposition (MOCVD) techniques are discussed in this context. InAs/GaAs(111) quantum dots (QDs) have been promoted as leading candidates for efficient entangled photon sources, owing to their high degree of symmetry (c_{3v}). Unfortunately, GaAs(111) suffers from a defect-ridden homoepitaxial buffer layer, and the InAs/GaAs(111) material system does not natively support Stranski–Krastanov InAs QD growth. Surfactants have been identified as effective tools to alter grown surface morphologies and growth modes, potentially overcoming these obstacles, but have yet to be studied in detail in this context. For MBE, it is shown that Bi acts as a surfactant when employed in GaAs(111) homoepitaxy, and eliminates defects/hillocks, yielding atomically-smooth surfaces with step-flow growth, and RMS roughness values of 0.13 nm. The effect is more pronounced as the Bi flux increases, and Bi is suggested to be increasing adatom diffusion. A novel reflection high energy electron diffraction (RHEED)-based experiment was also designed and performed to measure the desorption activation energy (U_{Des}) of Bi on GaAs(111), yielding $U_{Des} = 1.74 \pm 0.38$ eV. GaAs(111) homoepitaxy was also investigated using MOCVD, with GaAs(111)B exhibiting RMS

roughness values of 0.09 nm. Sb is shown to provoke a morphological transition from plastically-relaxed 2D to 3D growth for InAs/GaAs(111)B, showing promise in its ability to induce QDs. Finally, simulations for GaAs-based quantum well (QW) photoluminescence were conducted, and such QWs are shown to potentially produce very sharp linewidths of 3.9 meV. These results enhance understanding of Bi surfactant behaviour on GaAs(111) and can open up its use in many technological applications, paving the way for the realization of high efficiency/viable QD entangled photon sources.

Acknowledgements

All praise is due to ALLAH the most gracious, the all-knowing and the most wise.

It is impossible to truly express the level of gratitude I have for all those who have aided me in this endeavour, and without whom this work would certainly have not come to fruition. I am deeply grateful for having had the opportunity to carry out this work, and for all the interactions and opportunities I have had at McMaster. The skills, knowledge, and memories acquired here will be cherished for the remainder of my research career.

I am of course indebted to my advisor, Dr. Ryan Lewis, for all of his help, guidance, and support throughout the duration of my masters degree and while conducting this research work. Thank you for affording me the opportunity to work under your guidance, and for always having your door open for help and discussion, despite the COVID-19 pandemic. The knowledge I gained from our discussions on epitaxial growth is invaluable to me, and I have learned immensely from your example of how to think critically as a researcher.

I would also like to thank my lab colleagues Spencer, Trevor, and Chris for their collective help and friendship, which was felt amidst this pandemic. Being the second student to join Dr. Lewis' nascent research group, I am of course particularly

grateful for our senior PhD student, Spencer, and his continuous help with training and consultation.

Thanks are also in order to Dr. Manu Hegde who helped with the MOCVD growths in this thesis. Many thanks for sharing your expertise and for our valuable discussions. I would also like to thank all the staff at the Centre for Emerging Device Technologies (CEDT) for their contributions to this work. Thanks also to Dr. Shahram Tavakoli for his assistance with the MBE growths. Thanks to Doris Stevanovic for all her help, and for maintaining a safe research environment. Thanks also to all the staff at the Department of Engineering Physics. Thanks also to my thesis committee members, Dr. LaPierre and Dr. Mascher for taking the time to read this thesis, and Dr. Mascher especially for his solid state electronics course, which I learned a lot from. Thanks to my friends for their camaraderie and support during these trying times, especially Hesham, Khaled, Hossam, and Ganzoury.

Finally and above all, thanks to my parents, my brother, and sister for their tremendous, incalculable, and unconditional support and encouragement.

Contents

Abstract **iii**

Acknowledgements **v**

1 Introduction **1**

1.1 Gallium Arsenide (GaAs) & III-V Optoelectronics 1

1.2 GaAs substrate orientations and GaAs(111) 6

1.3 Quantum Dots on GaAs(111) for Quantum Photonics 8

1.4 Surfactant-mediated Growth on III-V Semiconductors and GaAs(111) 16

1.5 Thesis Outline & Scope 20

2 Background & Experimental Methods **22**

2.1 Epitaxial growth 22

2.2 Molecular Beam Epitaxy (MBE) 45

2.3 Metal-organic Chemical Vapour Deposition (MOCVD) 47

2.4 Atomic Force Microscopy (AFM) 50

2.5 Reflection High Energy Electron Diffraction (RHEED) 53

3 Bi as a Surfactant for MBE of GaAs(111) **59**

3.1 Calibration of the Bi source . . . 59
3.2 GaAs(111)A homoepitaxy . . . 64
3.3 Bi-assisted growth on GaAs(111)A . . . 67
3.4 Bi Desorption RHEED experiment . . . 80
3.5 Conclusion . . . 98

4 MOCVD Growth on GaAs(111) 100

4.1 Motivation . . . 100
4.2 GaAs(111)A homoepitaxy . . . 101
4.3 GaAs(111)B homoepitaxy . . . 105
4.4 InAs/GaAs(100) QD growth . . . 106
4.5 InAs/GaAs(111)B growth . . . 110
4.6 Sb-enhanced InAs/GaAs(111)B growth . . . 112
4.7 Conclusion . . . 114

5 Modeling of GaAs Quantum Well Photoluminescence 116

5.1 Motivation . . . 116
5.2 Theory & methodology . . . 118
5.3 QW modeling results . . . 123
5.4 Conclusion . . . 132

6 Conclusion & Future Work 134

6.1 Summary . . . 134
6.2 Future Work . . . 137

List of Figures

1.1 A simplified 1D projection of the energy diagram of both Si and GaAs as a function of momentum ($k - space$), also known as the band-structure. The black circles represent the carriers (electrons in the conduction band and holes in the valence band). The image is taken from I. Matthews "High-Efficiency Photovoltaics through Mechanically Stacked Integration of Solar Cells based on the InP Lattice Constant", PhD thesis, University College Cork (2014)[1] and shared under a (CC BY-NC-ND 3.0) license (`https://creativecommons.org/licenses/by-nc-nd/3.0/legalcode`). 3

1.2 A graph illustrating the interdependence and variability of both the energy bandgap E_g and the lattice parameter. The image is taken from M. Bayo "Theory of elasticity and electric polarization effects in the group-III nitrides", PhD thesis, University College Cork (2013)[2] and shared under a (CC BY-NC-ND 3.0) license (`https://creativecommons.org/licenses/by-nc-nd/3.0/legalcode`). 4

1.3 GaAs zinc-blende structure. Adapted and shared under the Pixabay License (`https://pixabay.com/service/license/`). 7

1.4 A zinc-blende(111) surface as an estimate of the GaAs(111) surface. The atomic radii for Ga and As are similar and thus for GaAs the atoms in the image would be of similar sizes. Image taken from SURFACE EXPLORER Version 2 visualization tool[3]. 8
1.5 Diagram illustrating crystallographic planes/orientations and the associated Miller indices. Atoms that exist in the planes are shown in red. 9
1.6 An illustration of the dependence of the density of states on the shape and dimensionality of the structure, a) bulk, b) QW c) quantum wire, d) QD. This image used has been taken from E. M. Sala "Growth and characterization of antimony-based quantum dots in GaP matrix for nanomemories", PhD thesis, TU Berlin (2018)[4] and shared under a (CC BY-NC-ND 4.0) license (`https://creativecommons.org/licenses/by-nc-nd/4.0/legalcode`). 11
1.7 An energy diagram demonstrating the bi-exciton exciton cascade scheme used in QDs for entangled photon pair emission. Dotted lines represent non-degenerate paths and levels (resulting from high FSS), leading to distinguishable photons as a result of non equal energies, and hence no detectable entanglement. 14
1.8 Simplified diagram for the ES barrier at the edge of a nucleating island. Adatoms are allowed to diffuse up but not down. Figure adapted from Wikipedia commons under a free license. 19
2.1 Sketch of different vapour pressure regimes vs. inverse temperature. . 26

2.2 A demonstration of the conditions imposed by the three temperature method for the growth of stoichiometric AB (III-V) films. P shown is the BEP (equivalent to deposited fluxes). 28
2.3 Graphical demonstration of the types of strained layer epitaxy. An elastically strained "coherent" film is shown on the left, while a plastically relaxed film with dislocations is shown on the right. In and out of plane strain is shown for strained layers. 30
2.4 Epitaxial growth modes for different surface energy combinations . . 32
2.5 Diagram comparing FM vs SK growth for a material system following SK growth such as InAs/GaAs(100), with respect to energy vs. film monolayers grown[5] 34
2.6 Arrhenius plot for thermally activated processes such as desorption and diffusion. 36
2.7 Illustration of the different kinetic and Arrhenius processes (diffusion and desorption) experienced by adatoms on the surface. 37
2.8 Illustration of adatoms interactions on the surface, particularly types of incorporation. The ES barrier can also be observed inhibiting step downhill diffusion. 38
2.9 The process of step-flow growth as the growth progresses. This occurs at $W_t < \lambda_{Diff}$ 40
2.10 A rough sketch and comparison of the coverage as predicted by the Langmuir model as a function of BEP. 42

2.11 A rough diagram detailing an example of a (2×) surface reconstruction and a relaxation of the surface layer. The $\vec{b}$ direction points out of the page. 44
2.12 A schematic of an MBE system. 47
2.13 A comparison of the growth chambers of a) MOCVD, b) SSMBE, and c) GSMBE. Figure adapted from Wikipedia commons under a free license. 50
2.14 A block diagram illustrating the components of a typical AFM tool. Figure adapted from Wikipedia commons under a free license. 52
2.15 3D sectional view sketch of intersection of Ewald sphere with lattice rods, yielding spots on the screen. 56
2.16 RHEED intensity variation as the growth progresses. A) symbolizes a fully formed smooth surface/epilayer (blue), B) symbolizes a growing epilayer with partial coverage, and C) represents the low point for the intensity at peak surface roughness. After C) the intensity climbs as the layer forms into a complete one, returning to A) once more and thus completing a monolayer growth cycle. 57
2.17 RHEED patterns for GaAs(111)A homoepitaxial growth, which will be elaborated upon in chapter 3. A 2×2 reconstruction, meaning the periodicity of the surface is twice the bulk, is shown on the left and a (1×1) pattern implying a surface reconstruction (during Bi deposition on GaAs(111) with identical surface periodicity to the bulk is shown on the right. 58
3.1 Single Figure Environment Listed Title 61

3.2 Arrhenius plot of the flux from the Bi cell vs. the applied temperature after calibration. 64
3.3 Cleaving lines for the (111) substrate. 66
3.4 1×1 μm^2 (left) and 5×5 μm^2 (right). AFM scans for the grown homoepitaxial GaAs(111)A buffer layer. Sample #2111 67
3.5 AFM scan of the homoepitaxial GaAs(111)A buffer layer. 1×1 μm^2 3D view of morphology (top left), 5×5 μm^2 3D view of morphology (top right), 1×1 μm^2 height profile at 0.25 μm vertically (bottom left, as indicated by the blue line in the previous figure), 5×5 μm^2 height profile at 2.5 μm vertically (bottom right, as indicated by the blue line in the previous figure). 68
3.6 Summary of the effect of Bi on the GaAs(111)A surface, inducing smoother surfaces with increased Bi flux. 69
3.7 Bi-covered sample as a result of bulk condensation. Sample #2157. . 70
3.8 Bi-covered sample magnified 100 times (left) and 500 times (right) using an optical microscope. 71
3.9 AFM scan of Bi-enhanced GaAs(111) buffer layer at Bi = 0.28 $^{ML}/_{s}$. 10×10 μm^2 AFM image (top left), 2 ×2 μm^2 AFM image (top right), 10×10 μm^2 3D view of the morphology (middle left), 2×2 μm^2 3D view of the morphology (middle right), 10×10μm^2 height profile at 2 μm vertically (bottom left, as indicated by the blue line), 2×2 μm^2 height profile at 1 μm vertically (bottom right, as indicated by the blue line). Sample # 2172. 72

3.10 AFM scan of Bi-enhanced GaAs(111) buffer layer at Bi = 0.28 $^{ML}/_{s}$. 1×1 μm^2 AFM image (left), 1×1 μm^2 3D view of the morphology (middle), 1×1 μm^2 height profile at 0.5 μm vertically (right, as indicated by the blue line). Sample # 2172. 74

3.11 AFM scan of Bi-enhanced GaAs(111) buffer layer at Bi = 1 $^{ML}/_{s}$. 5×5 μm^2 AFM image (top left), 2 ×2 μm AFM image (top right), 5×5 μm^2 3D view of the morphology (middle left), 2×2 μm^2 3D view of the morphology (middle right), 5×5 μm^2 height profile at 2.5 μm vertically (bottom left, as indicated by the blue line), 2×2 μm^2 height profile at 1 μm vertically (bottom right, as indicated by the blue line). Sample # 2181. 75

3.12 AFM scan of Bi-enhanced GaAs(111) buffer layer at Bi = 1 $^{ML}/_{s}$. 1×1 μm^2 AFM image (left), 1×1μm^2 3D view of the morphology (middle), 1×1μm^2 height profile at 0.5 μm vertically (right, as indicated by the blue line). Images processed using Gwyddion. Sample # 2181. 76

3.13 Demonstration of the surface energetics relevant to adatom diffusion leading to step-flow growth. There is a clear driving force for step-antibunching owing to the ES barrier. 79

3.14 Demonstration of how τ_{Des} is observed from the experiment (depositing Bi, allowing it to desorb, and observing RHEED changes). 84

3.15 RHEED pattern (1 × 1) as Bi is being deposited (left) and RHEED pattern (2 × 2) after 60 seconds when Bi deposition is halted and Bi desorbs (right). 84

3.16 Intensity rises vs. time for both the reappearing RHEED streak and the central one. 85
3.17 Intensity rises vs. time for the reappearing RHEED streak (2×2). Rise times for the intensities are an indication of τ_{Des} (inset is the plotted $2 \times 2 streak$). 86
3.18 Reappearing RHEED streak intensity data fitted with exponential equation in order to extract τ_{Des}. 88
3.19 Arrhenius plot (desorption rate vs. inverse temperature). $R^2 = 0.9735$. 90
3.20 Reappearing (2 × 2) RHEED streak intensity plotted versus time. Quick and gradual rises are outlined. 93
3.21 Intensity rises vs. time for the reappearing RHEED streak as an estimate of τ_{Des}. 94
3.22 Reappearing RHEED streak intensity data fitted with exponential equation in order to extract τ_{Des}. Quick initial rises are used. $R^2 = 0.996$, 0.9906, 0.9814 for 485, 515, 530 °C respectively. 95
3.23 Arrhenius plot for second experiment (desorption rate vs. inverse temperature) in order to calculate U_{Des}. $R^2 = 0.93766$. 96
3.24 Arrhenius plot for combined data from both experiments (desorption rate vs. inverse temperature) in order to calculate U_{Des}. $R^2 = 0.977$. . 97
3.25 Arrhenius plot for both experiments (desorption rate vs. inverse temperature), and for all the combined data, giving the final values. . . . 99

4.1 AFM scan of GaAs(111)A homoepitaxial buffer layer. $0.5 \times 0.5\ \mu m^2$ AFM scan (left), a 3D image of the morphology (right) and the height profile (bottom) for the vertical 0.25 μm line for the GaAs(111)A homoepitaxial growth at $T_{Sub} = 600$ °C and V/III = 15. Sample S24. . . 103
4.2 AFM scan of GaAs(111)A homoepitaxial buffer layer. $0.5 \times 0.5\ \mu m^2$ AFM scan (left) $1 \times 1\ \mu m^2$ scan (right) for the GaAs(111)A growth. Sample S24. 104
4.3 AFM scan of GaAs(111)B homoepitaxial buffer layer. $1 \times 1\ \mu m$ AFM scan (left), a 3D image of the morphology (right) and the height profile (bottom left) for the vertical (blue) 0.5 μm line for the GaAs(111)B homoepitaxial growth at $T_{Sub} = 720$ °C and V/III = 40. The bottom right image shows a $10 \times 10\ \mu m^2$ scan of the sample. Sample S26. . . 105
4.4 Structure grown for InAs/GaAs(100) QDs. 107
4.5 AFM scan of InAs/GaAs(100) QDs. $0.5 \times 0.5\ \mu m^2$ AFM scan (left), a 3D image of the morphology (right) and the height profile (bottom left) for the vertical 0.25 μm line for the InAs/GaAs(100) QD growth for this scan size. Another scan of the sample ($1 \times 1\ \mu m^2$) is shown on the bottom right. Sample S33. 109
4.6 PL spectrum for the InAs/GaAs(100) QD sample. 110
4.7 AFM scan of InAs/GaAs(111) layer. $0.5 \times 0.5\ \mu m^2$ AFM scan (left), a 3D image of the morphology (right) and the height profile (bottom left) for the vertical 0.25 μm^2 line for the InAs/GaAs(111)B growth for this scan size. Another scan of the sample ($2 \times 2\ \mu m^2$) is shown on the bottom right. Sample S37. 111

4.8 Sb:InAs/GaAs(111)B (Growth A): 1×1 μm AFM scan (left), a 3D image of the morphology (right) and the height profile (bottom left) for the vertical 0.5 μm line for this scan size as shown by the blue line. Another scan of the sample (5×5 μm) is shown on the bottom right. Sample S46. 113
4.9 Sb:InAs/GaAs(111)B (Growth B): 1×1 μm^2 AFM scan (left), a 3D image of the morphology (right) and the height profile (bottom left) for the horizontal 0.7 μm line for this scan size. Another scan of the sample (5×5 μm^2) is shown on the bottom right. Sample S24. 114
5.1 Flowchart of how the self consistent Schrödinger–Poisson solver works. 121
5.2 Schematic of simulated QW using Nanohub 1D Schrödinger–Poisson solver tool. 123
5.3 Properties for configuring the Nanohub simulation. 124
5.4 Simulated self-consistent energy levels and wavefunctions using Nanohub. 125
5.5 Simulated InGaAs QW structure. 126
5.6 InGaAs QW structure simulated wavefunctions and energy levels for the condcution band using tiberCAD. 127
5.7 InGaAs QW structure simulated wavefunctions and energy levels (top) for both the conduction (bottom left) and valence (bottom right) bands using Crosslight APSYS. 128
5.8 Spontaneous emission rate as an estimate of photoluminescence. . . . 130

5.9 Simulated photoluminescence for AlGaAs/GaAs QWs for 3 nm QW (top left), 5 nm (top right), 10 nm (bottom left), 15 nm (bottom right). In the same order, the FWHMs are 25, 25, 40, 40, and 55 nm for the highest excitation curve. 131
5.10 Simulated photoluminescence for AlGaAs/GaAs QWs for 20 nm QW for room temperature (left) and low temperature (6°K) (right). The FWHMs are around 45 nm and 22 nm respectively. 132
5.11 Peak emission energies for AlGaAs/GaAs QWs in Figure 5.9 vs. QW widths. 133
6.1 An example of a rough QW interface. The large rough QW is divided into many small QWs with varying widths. 140

List of Tables

1.1 Summary of growth of InAs/GaAs QDs on different GaAs orientations. 20

3.1 Ion gauge BEP (Torr) readings for the Bi cell at different temperatures. 60

3.2 Mask threshold parameters for estimating deposited Bi volume. . . . 62

3.3 τ_{Des} values from fitting. 89

3.4 U_{Des} and ν values from fitting for second experiment with uncertainties. 89

3.5 τ_{Des} values from fitting for second experiment. 93

3.6 Final U_{Des} and ν values from fitting combined data from both experiments with uncertainties (95% confidence bounds). 96

Chapter 1

Introduction

1.1 Gallium Arsenide (GaAs) & III-V Optoelectronics

The ubiquity and influence of semiconductors in our modern lives cannot be overstated. Serving as the cornerstone of a myriad of key industries in the 21st century, from computing to healthcare, semiconductors have heralded the advent of the information age. Photonics and optoelectronics have been key enabling technologies in recent decades for a wide range of sectors, particularly telecommunications. Optical/photonic communication provides significant advantages over its electronic counterpart, including being more robust against noise and electromagnetic interference, less power-hungry, and crucially, providing increased bandwidth[6] .

Silicon has dominated the microelectronics industry since the development of the integrated circuit by Texas Instrument's Jack Kilby in 1958, owing to its abundance

and favourable physical properties, such as its high thermal conductivity and the quality of its native oxide (SiO_2). Silicon has also proven to be a viable platform for photonic integrated circuits, with Si components buried in SiO_2 being capable of supporting guided electromagnetic modes thanks to total internal reflection ($n_{Si} = 3.4$, $n_{SiO_2} = 1.4$), and Si having low-loss and low-dispersion windows around the telecommunication wavelengths 1.3 μm and 1.55 μm, making Si-photonic integrated circuits a perfect and compact solution for interfacing with silica based optical fibres. However, while silicon has remained as the preeminent platform for the electronics industry, it is not a natural fit for the burgeoning and increasingly important optoelectronics industry. It suffers from fundamental physical limitations barring it from being solely relied upon as a monolithic photonic platform. Si possesses an indirect bandgap (the conduction band minima and the valence band maxima are not aligned in momentum space) as is evident in Figure 1.1. Therefore for conservation of momentum to hold, an emitted photon must be accompanied by the momentum contribution of a phonon for the emission process to occur, rendering emission a slow and inefficient process. For this reason, other semiconductors must be sought to act as photon sources and emitters. In this capacity, compound III-V semiconductors (semiconductors comprising elements from group III and V of the periodic table) have been widely regarded as the prototypical material used for the fabrication of viable light sources, a consequence of their direct bandgap. The ability to tweak the composition of the constituent elements (mole fraction) of the compound (as well as prepare ternary and quaternary compounds), altering the bandgap for variable energy photon emission, also gives great flexibility for the platform to target different applications. As a result however, these varying compounds yield a plethora of different lattice constant values

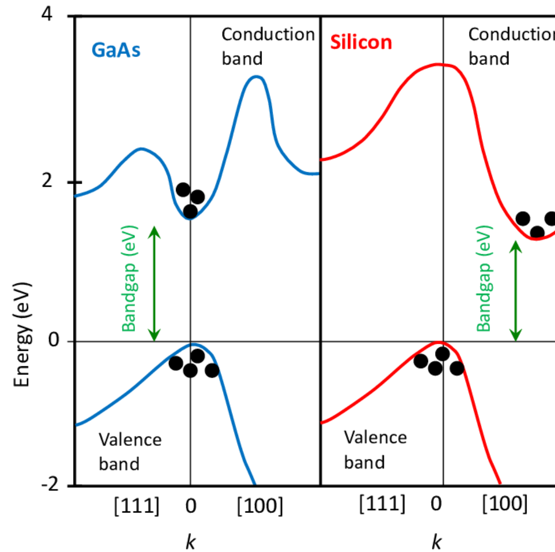

Figure 1.1: A simplified 1D projection of the energy diagram of both Si and GaAs as a function of momentum ($k - space$), also known as the bandstructure. The black circles represent the carriers (electrons in the conduction band and holes in the valence band). The image is taken from I. Matthews "High-Efficiency Photovoltaics through Mechanically Stacked Integration of Solar Cells based on the InP Lattice Constant", PhD thesis, University College Cork (2014)[1] and shared under a (CC BY-NC-ND 3.0) license (https://creativecommons.org/licenses/by-nc-nd/3.0/legalcode).

depending on compound composition, hampering integration with other materials (by causing defects, strain etc.), and can be seen as a key drawback of III-V as a platform. This fact is clearly showcased in Figure 1.2. Another primary advantage of III-V compound semiconductors is the ability to grow them in heterostructure configurations (different III-V thin films with varying bandgaps grown epitaxially atop each other) to make use of bandgap engineering. This fact sheds light on the importance of GaAs as a platform and substrate for photonics, as it can be seen from Figure 1.2 that GaAs is unique in the fact that a higher direct bandgap ternary compound (AlGaAs) shows very little lattice constant variation with GaAs, making AlGaAs/GaAs a powerful

combination for the visible region. This concept of bandgap engineering allows for the realization of devices relying on specifically tailored optical properties thanks to, for example, the ability to trap carriers in potential wells, exploiting the change in the density of states and Coulomb interactions between carriers. This has paved the way for quantum-well (QW) devices (such as QW lasers). These devices along with others are grown using several different epitaxial growth techniques, of which Molecular Beam Epitaxy (MBE) and Metal-Organic Chemical Vapor Deposition (MOCVD) will be investigated in this thesis. Of the many III-V semiconductors that have been used,

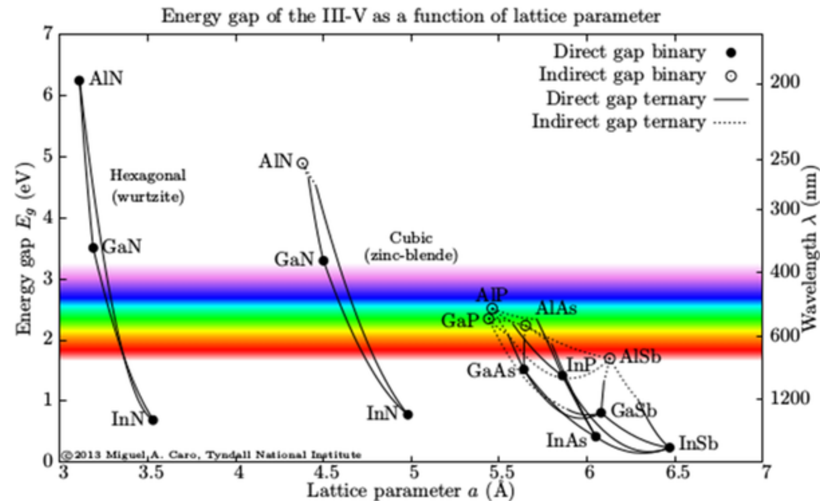

Figure 1.2: A graph illustrating the interdependence and variability of both the energy bandgap E_g and the lattice parameter. The image is taken from M. Bayo "Theory of elasticity and electric polarization effects in the group-III nitrides", PhD thesis, University College Cork (2013)[2] and shared under a (CC BY-NC-ND 3.0) license (`https://creativecommons.org/licenses/by-nc-nd/3.0/legalcode`).

GaAs and InP have traditionally stood out as having the most commercial success, (with GaN recently emerging as well for use in lighting and high power RF electronics [7]), lending themselves to a variety of high-speed applications, particularly in optoelectronic and radio frequency/microwave (RF/MW) applications[8]. GaAs

dominates the current market when it comes to RF and microwave components and amplifiers. GaAs high-speed transistors are readily used today for mobile phone RF components, and can also be found in microwave point-to-point links, and in satellite communication equipment, such as power amplifiers. This is due to GaAs' high carrier mobility, which allows operation of high frequency components in the RF/MW regime. GaAs is also extensively used in the photonics industry for a wide array of applications, including but not limited to: lighting (LED and laser fabrication), for photodetectors in the data communication industry, and for solar cells. GaAs-based Vertical Cavity Surface Emitting Lasers (VCSELs) in particular are used for 3D sensing applications such as in LiDAR (short for Light Detection and Ranging), the adoption of which is rapidly increasing for use in autonomous vehicles and mobile phones[9]. This is thanks to GaAs being an efficient photon emitter. Physically, these capabilities arise from the shape and nature of the bandstructure, a simplified 1D projection of which (for GaAs and Si) is shown in Figure 1.1. Upon inspection of the carriers at the band edges in the diagram (the ones pertinent to recombination and generation processes important for optoelectronic devices), it can be seen that GaAs possesses a direct bandgap, as well as a high electron mobility (μ_e) (up to $8500 cm^2/V.s$[10]) owing to the increased curvature of the $E - k$ diagram. This is because the effective mass (m^*) for carriers is inversely proportional to the curvature, and mobility is inversely proportional to effective mass. Both phenomena are described in Equations (1.1.1) and (1.1.2).

$$m_e^* = \hbar^2 \cdot \frac{1}{\partial^2 E / \partial k^2} \tag{1.1.1}$$

$$\mu_e = \frac{e \cdot \tau_{scat}}{m_e^*} \tag{1.1.2}$$

Where τ_{scat} is the scattering time, and e is the charge. In addition, the high saturation velocity allows for linear operation when applying moderate electric fields. In optoelectronics, GaAs is used extensively as an emitter/detector of red and near infra-red wavelengths, with a bandgap energy of 1.43 eV. Several GaAs-based alloys have been employed for longer wavelength emission and detection for telecommunications, particularly InGaAs and GaAsSb[8]. Additionally, it has been shown that the introduction of arsenic antisite point defects can help extend the emission wavelength of GaAs light sources to suitable telecommunication wavelengths[11] , facilitating easy interfacing with existing optical fibre infrastructure. These properties make GaAs a crucial material and platform for optoelectronics, especially as a light source, and hence the growth of high quality GaAs films and nanostructures, as well as the intricate study of their properties, is of paramount importance to this industry. This is what will be discussed and expanded upon in this thesis.

1.2 GaAs substrate orientations and GaAs(111)

GaAs possesses a zinc-blende structure, consisting of Ga and As atoms as shown in Figure 1.3.

There has been considerable interest in exploring the properties of heterostructures and quantum nanostructures grown on different GaAs orientations/crystallographic planes (planes shown in Figure 1.5). Ga terminated versions of the surface are denoted by the suffix A (e.g. GaAs(111)A), while As terminated surfaces are denoted with

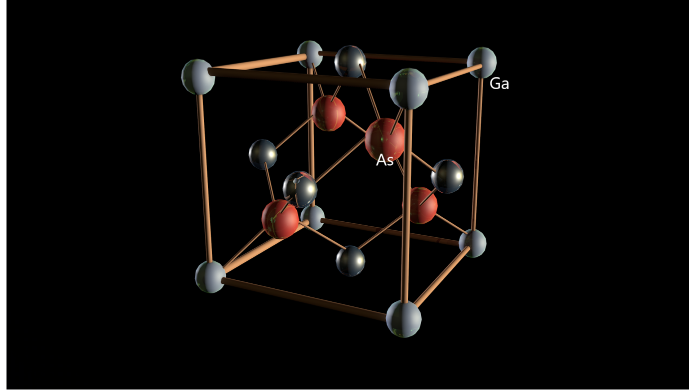

Figure 1.3: GaAs zinc-blende structure. Adapted and shared under the Pixabay License (https://pixabay.com/service/license/).

the suffix B (($\bar{1}\bar{1}\bar{1}$)). This is important to note as growth on these surfaces, and the properties of structures on these surfaces are distinct. The B surface is more reactive since it possesses two extra valence electrons. The (111) surface (surface atom density = $^4/_{\sqrt{3}a^2}$, where a is the lattice parameter) is more closely-packed than the (100) (density = $^2/_{a^2}$) plane but less than the most closely-packed (110) plane (density = $^4/_{\sqrt{2}a^2}$) when comparing the low index orientations. The surface structure itself is also highly symmetric (c_{3v} symmetry) as explained later in this chapter, and thus the diffusion of adsorbed atoms (atoms which have been deposited and stuck to the surface, participating in the growth) on the surface is thought to be isotropic[12], creating symmetric structures[13]. An illustration of the GaAs(111) surface structure can be seen in Figure 1.4.

Conventionally, the (100) orientation of GaAs has been preferred for GaAs heterostructure and device growth, and has been extensively studied[14]. One of the reasons this surface is preferred is due to the relatively smoother and more favourable surface morphologies achievable on this surface (although GaAs(100) homoepitaxy can yield mounds and deviate from smooth 2D layer growth under a multitude of

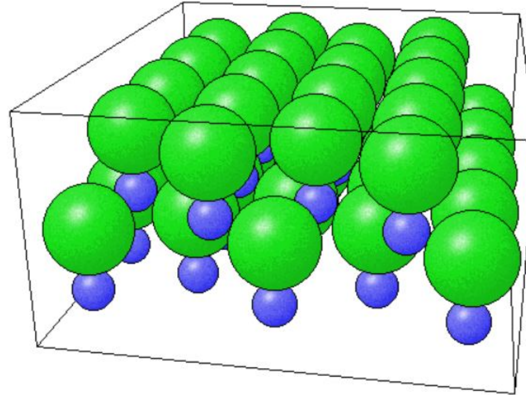

Figure 1.4: A zinc-blende(111) surface as an estimate of the GaAs(111) surface. The atomic radii for Ga and As are similar and thus for GaAs the atoms in the image would be of similar sizes. Image taken from SURFACE EXPLORER Version 2 visualization tool[3].

growth conditions)[15]. Nevertheless, GaAs homoepitaxial layers have been grown with a root mean square (RMS) roughness of 0.2 nm[16].

1.3 Quantum Dots on GaAs(111) for Quantum Photonics

Another important reason behind the popularity of GaAs(100) as a substrate is due to the Stranski–Krastanov (SK) growth mode (growth modes and other key epitaxial growth concepts are elaborated upon in chapter 2), also known as the 2D layer + islands growth mode, readily occurring on the surface when depositing InAs thin films, as opposed to solely layer growth or island growth. This is due to a confluence of factors, but the growth mode is primarily dictated by the surface energies and lattice constants (and thus strain) of the deposited material (film) and the bulk (substrate),

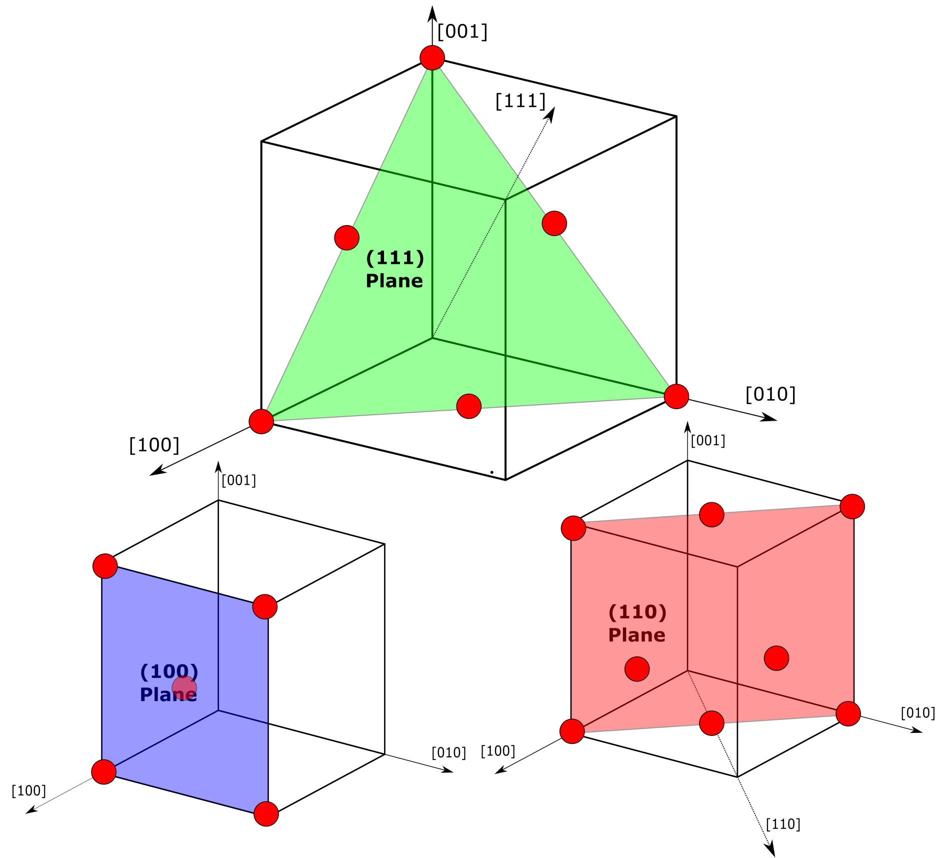

Figure 1.5: Diagram illustrating crystallographic planes/orientations and the associated Miller indices. Atoms that exist in the planes are shown in red.

which influence the behaviour of the deposited adatoms on the surface. The presence of this SK growth mode in InAs/GaAs(100) heteroepitaxy allows for the self-assembly of islands or quantum dots (QDs) after the growth of a 2D wetting layer, making this orientation the preferred platform for InAs/GaAs QD growth[17]. For other low index orientations of GaAs such as (110) and (111), this SK growth mode is not manifested during InAs deposition, and thus cannot support self-assembled QD growth. Self-assembled QDs have the advantage of ease of fabrication due to their self-organizing nature, bypassing complicated patterning procedures for selective area

epitaxial growth of these structures[18], but lack specificity and uniformity. These exceedingly relevant and important quantum nanostructures have the potential to be employed extensively in a wide variety of industries and technologies, particularly in the context of photonics. Some types of QDs (such as colloidal QDs) are already seeing mainstream commercial adoption in displays[19], while epitxially grown QDs (such as InAs/GaAs), have shown remarkable potential as QD lasers, and as quantum photonic sources, such as entangled photon sources[20][21]. QDs have garnered considerable interest[22] owing to their atom-like properties, possessing a quantized density of states for carriers as a result of three-dimensional quantum confinement as seen in Figure 1.6, with dimensions approaching the excitonic Bohr radius. Another key property of QDs is the ability to tailor many pertinent optical properties such as the the emission energy (depending on the confinement), by altering the shape and size of the QD. This can be understood in light of the particle in a box quantum mechanical model, where a change in the width of the well results in a change of the energy level due to the confinement. Other properties, such as the bandgap, can be varied by choosing different material systems, providing several parameters to tune. Other material systems have also exhibited self-assembled QD growth (e.g. Ge/Si QDs)[23]. This tunability that QDs have, relating to size and materials, enables the fabrication of a myriad of useful optoelectronic devices operating at a range of different wavelengths. For example, QD lasers have been shown to be more resilient against temperature fluctuations and are more energy efficient[24]. QDs have also been widely used for solar cells and displays with more efficient filtering and purer colours, among other applications[19][25] .

Arguably the most exciting and emerging application for QDs is in their use as a

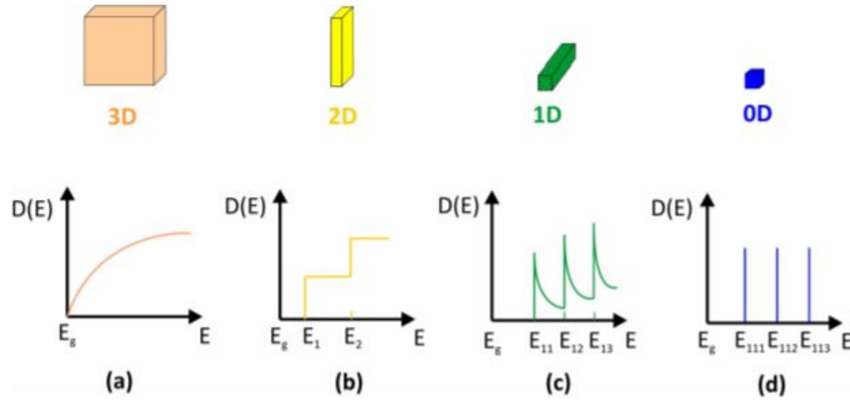

Figure 1.6: An illustration of the dependence of the density of states on the shape and dimensionality of the structure, a) bulk, b) QW c) quantum wire, d) QD. This image used has been taken from E. M. Sala "Growth and characterization of antimony-based quantum dots in GaP matrix for nanomemories", PhD thesis, TU Berlin (2018)[4] and shared under a (CC BY-NC-ND 4.0) license (https://creativecommons.org/licenses/by-nc-nd/4.0/legalcode).

platform for quantum computing, as well as quantum light sources, including single and entangled photon sources[26]. These are crucial for the rapidly expanding field of quantum communication and information.

Since the dawn of the new millennium, a second quantum revolution has been brewing, with advances allowing us to manipulate quantum particles for useful potential applications in quantum information and sensing. The realization of viable quantum optical networks would have profound implications for society, bringing about an era of secure communication and a quantum internet[27]. While quantum computing relies on the manifestation of quantum properties like superposition in the form of qubits for exponentially faster computation, quantum communication relies on the ability to exploit entanglement of quantum states as random encryption keys which are immune to tampering and eavesdropping. Within this framework, photons have a key role to play in this quantum future, as photonics forms the backbone of

communication and is a mature technological platform. Additionally, photons can be relatively reliably employed as "flying qubits" thanks to their relative lack of interaction with their environment (minimizing crosstalk and decoherence), their ease in manipulation and detection compared to other matter-based qubits, and their ability to operate at room temperature[28]. They can also be used to interface with other physical manifestation of qubits, such as solid-state spin-based qubits like electrons in semiconductor defects[29]. In light of this, it is thus crucial to realize efficient, and commercially viable entangled photon pair sources to reify the promise of quantum technology.

Epitaxially grown III-V QDs are of special interest for quantum information applications (such as entangled photon emitters) owing to the aforementioned advantages of both QDs and III-V semiconductors, and have already begun to see successful commercialization[30]. In this context, GaAs(111) has exhibited remarkable promise as a substrate for quantum photonics[26][31]. It has been posited that if SK growth for InAs/GaAs could somehow be induced on non-(100) GaAs surfaces, growing on other low index surfaces such as (110) and (111) could produce QDs with unique and useful properties as a consequence of their symmetries, with point group symmetries of C_s and C_{3v} respectively[26]. For the C_{3v} point group symmetry, this means the structure can be rotated $2\pi/3$ on the vertical axis and still be in an equivalent configuration. Consequently, QDs on (110) GaAs surfaces have been identified as ideal candidates for single photon sources owing to their linearly polarized emission[32], while QDs on (111) surfaces' three-fold symmetry and vanishingly small fine structure splitting (FSS) make them a very promising platform for polarization-entangled photon emitters[31][26][20]. This is not the case for InAs/GaAs(100) QDs, as they

exhibit low symmetry and large FSS values which are detrimental to entangled photon generation as will be elucidated later in this section. Therefore, the crux of the dilemma of QD growth for quantum light sources is the fact that self-assembled InAs QDs can only be grown on GaAs(100), which has poor symmetry, and the surfaces which do promise properties conducive to efficient quantum light source operation (such as high symmetries) have not been able to support QD growth as SK growth does not arise natively on them.

Entangled photon sources have been realized before using the χ^2 nonlinearity in nonlinear crystals, (such as periodically-poled lithium niobate)[33], and semiconductor QDs. QDs benefit from a significant advantage over other methods as they can generate entangled photons on demand (do not rely on probabilistic processes), can leverage existing semiconductor processing technology for integration (not using bulky components), and enjoy near-unity quantum efficiency[34]. The disadvantage of the QD method has historically been the lack of symmetry in the QDs grown using the SK method on (100), and the high degree of FSS. FSS arises as a result of electron-hole pair exchange interactions, spin-orbit coupling, the asymmetry of the structure, the nature of the confining potential, and the asymmetry of piezoelectric fields. For QD-based entangled photon emission, the carriers are excited to a higher energy state (triggered) on demand by a laser pulse, and subsequently a bi-exciton-exciton cascade recombination to the ground state occurs as outlined in Figure 1.7 ($|XX\rangle \rightarrow |X\rangle \rightarrow |0\rangle$)[34]. After this process, the XX photon ($|XX\rangle \rightarrow |X\rangle$) is entangled with the ($|X\rangle \rightarrow |0\rangle$) photon and both are indistinguishable, emitted with opposing and entangled circular polarization directions (left (L) and right (R) as shown in Figure 1.7).

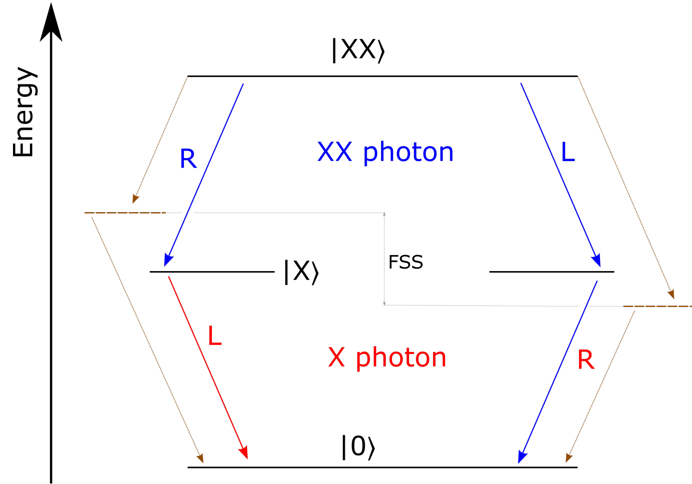

Figure 1.7: An energy diagram demonstrating the bi-exciton exciton cascade scheme used in QDs for entangled photon pair emission. Dotted lines represent non-degenerate paths and levels (resulting from high FSS), leading to distinguishable photons as a result of non equal energies, and hence no detectable entanglement.

Thus, it is clear the high degree of FSS causes a splitting of the energy levels/states, which is detrimental to the production of entangled photon pairs as in order to be entangled, the photons must be emitted with complete indistinguishably in all degrees of freedom (energy, polarization etc.). There can be no difference in the path they were produced by (FSS < 10 μeV), with the maximum tolerable FSS linked to the natural linewidth of the emission. Therefore it is imperative that the intermediate excitonic states $|X\rangle$ for both paths are degenerate. These issues have been mitigated before by implementing complex setups and post-processing of QDs, such as manual selecting symmetric QDs post-growth, applying electromagnetic fields, and using strain to ameliorate the FSS, thus forcing degenerate energy levels[26]. Finding a way to create highly symmetric self-assembled QDs would allow for the realization of an ideal entangled photon emitter (which thus far has remained elusive), as the QD-based emitter would be capable of producing highly entangled, on demand, easily

extractable (using nanophotonic lenses and cavities), and indistinguishable photons, ticking all the traditional boxes needed for an ideal entangled photon emitter[35], while also facilitating integration with mature semiconductor platforms. These properties undergird the true potential of GaAs(111) as a platform for quantum photonics, with highly symmetric pyramidal QDs shown to form on this surface[20]. Notably however, while previous attempts at forming GaAs(111)-based QDs have been explored [20][36], most have used droplet epitaxy to circumvent the lack of a native SK growth mode and thus QDs for InAs/GaAs(111). Unfortunately droplet epitaxy has some inherent drawbacks, such as poor structural quality of the QDs grown due to the crystallization of metal droplets at low temperatures, and complex fabrication procedures[37]. Tensile strained GaAs(111) QDs grown on InAlAs(111) barriers on a InP(111) substrate have recently been demonstrated as one of the only manifestations of (111) QDs induced during SK growth[38], but InAs/GaAs(111) QDs have remained unattainable.

While highly symmetric QDs for entangled photon emission are the most prominent prospective application for GaAs(111), GaAs(111) has also been shown to be a useful substrate for spintronics applications, with AlGaAs/GaAs(111) QWs exhibiting high spin relaxations times[39][40] when applying an electric field, suppressing spin dephasing. Additionally, GaAs(111)B has also been used to grow GaAs/Ge/GaAs QWs, which have exhibited topological insulator transitions, allowing for the realization of topological insulators using common and commercially available semiconductor materials[41]. Investigating the smooth growth of GaAs(111) and the role of surfactants to this end could also play an important role in realizing these applications.

1.4 Surfactant-mediated Growth on III-V Semiconductors and GaAs(111)

In general, surfactants are surface segregating elements/compounds which alter surface energies (such as detergents and wetting agents). In the context of epitaxial growth they have proven to be effective in altering surface properties (such as surface and adatom energetics and kinetics) and thus how deposited adatoms behave on substrates/surfaces, also changing diffusion lengths of adatoms on the surface and nucleation rates. Consequently, surfactants can help cause morphological changes in the deposited layers, by altering the kinetics and thermodynamics of the growth, facilitating heightened control on how growth occurs at the surface level. Surfactants tend to float atop the growing epilayer (most stable, least energy configuration), avoiding incorporation into the bulk of the material and thus alloying and altering material properties intrinsically, while passivating surface dangling bonds.

Historically, the first reported use of a surfactant for epitaxial growth was by Copel et al. in 1989[42], in which As was used to provoke smooth 2D layer growth of Ge sandwiched in a Si/Ge/Si heterostructure, rather than SK growth. As was shown to float atop the heterolayer, and not incorporate. As, Sb, Pb have been used as surfactants for IV growth (Si, Ge etc.), primarily for creating smooth layers [43]. The concept was extended to III-V materials[44] when Pb was used to induce 2D GaAs growth at significantly lower temperatures. Pb was found to increase diffusion length while Te was found to decrease it. Conventionally for III-V epitaxy, surfactants can be classified into non-reactive (III and IV elements) surfactants, which typically

reside in interstitial sites due to their size, and reactive surfactants, which slot substitutionally into surface sites (V and VI elements) and swap positions with adatoms to remain afloat (as confirmed by density functional theory calculations[45]). Non-reactive elements tend to increase the diffusion length of adatoms (inducing smoother surfaces as adatoms can reach far away islands) while reactive surfactants tend to inhibit diffusion[46]. For III-V MBE and MOCVD, Bi and Sb has been identified as ideal surfactants, owing to their electronically neutral nature with group V elements (isoelectronic), so as not to act as a dopants if incorporated in the film. Bi in particular is an attractive option as it especially does not tend to incorporate, rendering it an ideal surfactant. While traditionally surfactants have been used to induce smooth 2D growth where SK 2D + island growth exists[44][47] as discussed, surfactants have also been used to decrease interfacial surface roughness in III-V QWs [48], and more recently for enhancing optical emission/photoluminescence[49], and have been used to decrease diffusion lengths in order to facilitate the growth of uniform InGaAs nanoridges on patterned Si wafers facilitating easier III-V integration[50], where this selective area epitaxy technique limits defect formation. Sb especially has been used for its tendency to incorporate in small quantities under certain conditions to lower bandgap in InAs heterostructures, extending QW and QD operation into telecommunication wavelengths (1.3+ μm)[47][51]. Sb has also been used to increase dopant incorporation for doped films[52], while Bi has been found to enhance surface morphology and increase adatom diffusion[53].

.

Perhaps the most recent and emerging application for surfactants has been to

alter and even induce QD and SK growth, rather than inhibit it for smoother surfaces. Of the assorted material systems, InAs/GaAs has exhibited the most potential in inducing SK growth and thus dislocation-free optically active QDs, along with Si/Ge. While this is true for GaAs(100) QDs, this cannot be said however for the highly sought after GaAs(111) QDs, as well as GaAs(110) QDs. Unfortunately, several obstacles hinder growth on these surfaces. As the issue of principal concern, these surfaces are not conducive to QD growth; the SK growth mode cannot be observed on these surfaces with InAs deposition as previously stated. Another hurdle inhibiting such growth is that GaAs(111) homoepitaxy does not yield smooth 2D layer growth, but rather defect-ridden layers with large surface roughness, and large hillocks on the order of microns wide, as a result of stacking faults during growth and the influence of the Ehrlich-Schwöbel (ES) barrier[54], shown in Figure 1.8. The ES barrier is an energy barrier introduced empirically in epitaxial growth models to model how the surface morphology emerges on certain surfaces. Metal (111) surfaces have been known to exhibit large ES barriers, driving 3D growth and the creation of mounds for homoepitaxial growths. The ES barrier essentially acts as a unidirectional diffusion barrier, allowing uphill diffusion but inhibiting downhill diffusion, promoting the nucleation of tall mounds[54]. This is in contrast to GaAs(100), where this barrier is suggested to be small and negative, encouraging net downhill diffusion and inhibiting 3D growth[55]. For non-diffusion limited conditions, the ES barrier is seen as the primary contributor to the rough surface morphology witnessed for GaAs(111)[54].

This means that buffer layers and InAs wetting layers grown on such unfavourable morphologies will not be able to support coherent, optically-active QDs. It is thus imperative to tackle first the problem of rough GaAs(111) homoepitaxial surfaces,

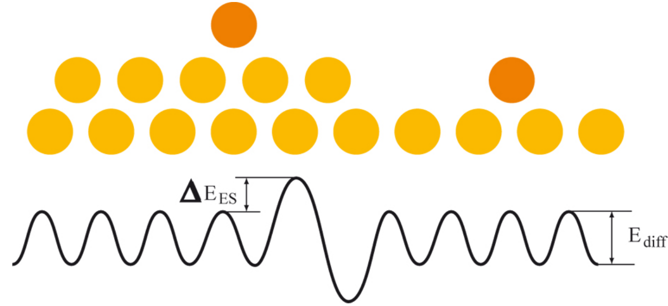

Figure 1.8: Simplified diagram for the ES barrier at the edge of a nucleating island. Adatoms are allowed to diffuse up but not down. Figure adapted from Wikipedia commons under a free license.

and subsequently the issue of inducing the SK growth mode on such surfaces, before being able to harness the potential on InAs/GaAs(111) QDs for entangled photon sources. As a side-note, it is important to note however that relatively smooth layers can be grown on GaAs(111)B in particular using MOCVD [56][57], albeit at very precise and narrow growth conditions.

For QDs, there is precedent for the employment of surfactants during both MBE and MOCVD growth. On GaAs(100), where SK growth readily occurs, Bi and Sb have been used to improve QD uniformity and control QD density preventing QDs from getting too large (coalescence), ensuring optically active QDs[58][51][59][60]. For this case, it is posited that In adatom diffusion is decreased as a result of Bi surfactant action, although this fact is subject to some debate[58][59][60]. Recently, QD growth was successfully achieved on GaAs surfaces where SK growth was previously unattainable using Bi and Sb, such as GaAs(110)[61][62][63][64]. Preliminary investigations have suggested this could occur on GaAs(111) as well[65], but despite this flurry of promising research activity, no in depth studies have been carried out for Bi/Sb-mediated QD growth on GaAs(111), and GaAs(111) heteroepitaxy using these surfactants has not been discussed. These are the gaps in the literature which this

GaAs:	(100)	(110)	(111)
State of Growth	2D + island (SK mode)	2D (FM mode)	defects (+ homoepitaxy) (MBE)[54] 2D (MOCVD)[56]
Bi/Sb action	uniform QDs QD density control[58][51][60]	inducing QD (SK mode) [63][62]	**contribution of this thesis**
Application	QD growth (lasers etc.)	QD single photon sources (C_s)	entangled photon sources (C_{3v})

Table 1.1: Summary of growth of InAs/GaAs QDs on different GaAs orientations.

thesis aims to address. A summary of the current state of InAs/GaAs QD surfactant-mediated growth on different GaAs orientation is presented in Table 1.1.

1.5 Thesis Outline & Scope

Principally, the scope of the thesis is the investigation of the behaviour of Bi as a surfactant on GaAs(111) using MBE, investigating its properties and inducing smooth surfaces where previously not possible for GaAs(111) buffer layers. This thesis also aims to explore the use of Sb as a surfactant on GaAs(111) as well as inducing SK growth of QDs on the surface.

Chapter 2 of this thesis reviews the pertinent theoretical background on epitaxial growth and thin film deposition and characterization, with a particular focus on the techniques used extensively to carry out the work in this thesis; namely MBE and MOCVD. Reflection High Energy Electron Diffraction (RHEED) and the Langmuir adsorption isotherm model for monolayer growth will also be elaborated upon as they both play a key role in this thesis, allowing the characterization of how GaAs(111) homoepitaxial growth proceeds with Bi, as well as the estimation of the desorption energy barrier for Bi on GaAs(111), which has not yet been reported in the literature. Discussion of adatom kinetics such as diffusion and desorption is also presented. Epitaxial growth modes, surface reconstructions, and the three temperature method

for III-V epitaxial growth are also touched upon.

Chapter 3 will present the first novel work of the thesis, that being the use of Bi as a surfactant to induce atomically-smooth surface morphologies and atomic steps on MBE-grown GaAs(111). The chapter will also examine the influence of different growth conditions like substrate temperature and Bi flux on the grown surface. A procedure to calibrate the Bi source is also covered. Another novel contribution, namely the measurement of the desorption barrier of Bi on GaAs(111), is presented. The design of the RHEED-based experiment will be elaborated upon in detail, as well as the implementation, comprising a camera to record RHEED fluctuations, and image analysis and processing to plot RHEED streak intensity changes with time as an indication of Bi desorption at various temperatures. The growths and experiments shed light on how Bi alters the adatoms kinetics on the surface.

Chapter 4 will explore the investigation and growth of homoepitaxial GaAs(111) layers and the novel used of Sb to induce InAs QDs on these surfaces using MOCVD.

Chapter 5 covers the modelling portion of this thesis. The Schrodinger-Poisson equation/model for calculating energy levels in quantum wells (QWs) is discussed, and applied to GaAs/AlGaAs and InGaAs/GaAs QWs. An estimate of the spontaneous emission or photoluminescence from the structure is also calculated. Finally, the effect of interface roughness on the optical emission is also investigated.

Chapter 6 provides the conclusion of the work presented in the thesis, as well as identifying areas of future work and improvement.

Chapter 2

Background & Experimental Methods

In this chapter the necessary background needed to understand the work in this thesis will be presented, as will a brief overview of the experimental tools used to carry out and characterize the growths done. The chapter will touch upon the different types of epitaxial growth modes possible for thin film epitaxial growth, as well as the surface dynamics/kinetics and how they can influence these growths.

2.1 Epitaxial growth

The word epitaxy has its origins in Greek words, with "epi" referring to the word "above" and "taxy" meaning "order". This accurately describes the process of epitaxial growth, which is the process of forming orderly, crystalline layers by depositing atoms of the chosen material atop a crystalline "seed" layer or substrate. The deposition of these layers is often done in the form of condensing gas precursors onto the

crystalline substrate under certain temperature and pressure conditions to achieve condensation. The subsequent epitaxial layers (epilayers) have a well-defined crystal orientation and are largely influenced by the starting seed layer as they grow on top of it, and tend to inherit the seed's order, orientation, and structural properties. Epitaxial growth can either be of the homoepitaxial variety, meaning that a material is deposited or grown atop a substrate or seed of the same material, or heteroeptaxial, meaning a different material is deposited. The latter form is the more troublesome one, as differences in crystal structures, lattice spacing, and thermal expansion coefficients among other properties, usually complicate the growth process and can lead to excessive strain and disharmony, culminating in dislocation/defect-ridden growths. Strained layer epitaxy arising from lattice parameter mismatches is perhaps the most important issue to consider for material growth and integration in heteroepitaxy, and is discussed later on in this chapter.

In epitaxy, the goal is to form or deposit these crystalline thin films on the substrate. Epitaxial growth processes can be chemical in nature such as in chemical vapour deposition (CVD) and metal-organic chemical vapour deposition (MOCVD), where a heated substrate provides the heat needed to facilitate chemical reaction between the precursor gasses on the surface (causing deposition of the chosen material), or physical, such as physical vapour deposition (PVD) techniques like molecular beam epitaxy (MBE), where the material to be deposited is heated/sublimated from an effusion cell and the atoms travel in beams onto the substrate to grow the film. Other physical deposition techniques include pulsed laser deposition (PLD), where the material to be used is ablated by a laser and turned into vapour to be deposited on the target, and sputtering, where a plasma or some sputtering gas attacks a target

(sputtering source), ejecting (sputtered) material from it onto the substrate, gradually depositing a film. PVD techniques usually necessitate operating in a vacuum in order to increase mean free path length, providing directionality (ballistic regime), and making it a line of sight technique. Chemical techniques include chemical vapour deposition (CVD), MOCVD, and plasma-enhanced CVD (PECVD), among others. While CVD has a high degree of versatility, does not require an ultra high vacuum environment (high purity environments with some level of vacuum are used), and produces a higher growth rate, it requires very high substrate temperatures to facilitate precursor reaction and deposition, and is less precise than PVD techniques such as MBE. MOCVD and MBE were both used in this thesis for GaAs(111) growth, and will be discussed in later in this chapter.

Many factors can impact the nature of the growing epitaxial layer, including the strain (due to lattice mismatch of the growing layer material and the substrate material), the surface energy difference between the growing film and substrate, and the growth conditions (temperature, flux, growth rate, ratio of fluxes, etc.) among others. Flux (z) or alternatively, impingement rate, is defined as the amount of material being deposited (e.g atoms) per unit area per second.

It can be deduced using the ideal gas law and the Maxwell velocity probability distribution[66]. The equation for impingement rate z ($^{atoms}/_{cm^2 \cdot s^2}$) can be defined as

$$z = \frac{P}{\sqrt{2\pi m k_B T}} \tag{2.1.1}$$

where m is the mass of the impinging atoms, P is the pressure, k_B is the Boltzmann constant, and T is the temperature. For directional gas beams in ultra high vacuum (UHV) systems, such as in the molecular beam epitaxy (MBE) growth technique, the

flux can be defined as a beam equivalent pressure (BEP) as intuited from Equation 2.1.1.

During deposition it is important to control the temperature and pressures of the environment to bring about orderly growth of the epitaxial films with the desired stoichiometry. Operating with substrates at low temperatures, or at high fluxes or pressures so as to reach a supersaturated vapour state with a condensate would result in the bulk condensation (adhesion of gas atoms to its own "condensate" bulk phase) of the material, which is undesirable for the intricate growth of heterostructures or superlattices for example, or thin layers such as QWs. For thin film growth it is desirable to be at equilibrium vapour conditions or below, whereby an adsorbate layer exists (surface layer of deposited molecules/atoms adhering to the surface of the substrate). The adsorbate is a distinctly surface phase phenomenon and can be seen as the fifth state of matter (after gas, liquid, solid, and plasma), with its own properties. The equilibrium vapour pressure is the pressure at which the vapour is in equilibrium (condensation and evaporation are equal) with its condensed phase. Figure 2.1 details the different regimes. The equilibrium vapour pressure of a vapour P_{eq} ($^{N}/_{m^2}$) is given as

$$P_{eq} = P_{st} \cdot e^{\frac{\Delta S}{k}} \cdot e^{\frac{-\Delta H}{kT}} \tag{2.1.2}$$

where ΔH is the heat, ΔS is the entropy of vaporization ($^{J}/_{mol}$), and P_{st} is the standard atmospheric pressure (1.013×10^5 $^{N}/_{m^2}$).

For the deposition of a thin film of a compound/alloy (e.g. GaAs), it is not sufficient to thermally evaporate a flux of GaAs to deposit it onto a substrate. This is because the more volatile component (in GaAs' case, As) is quickly depleted from

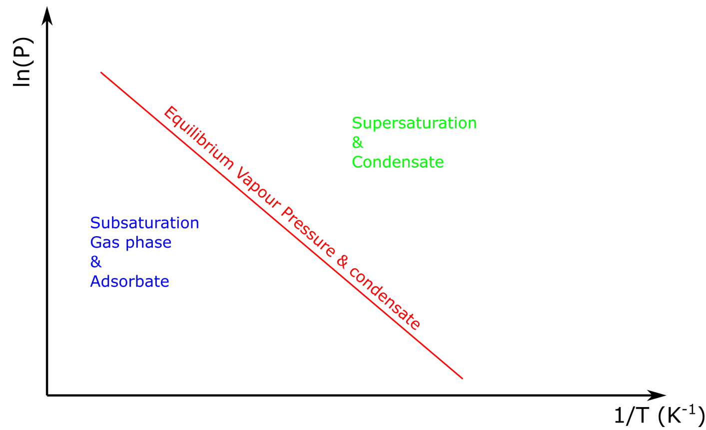

Figure 2.1: Sketch of different vapour pressure regimes vs. inverse temperature.

the source during the thermal evaporation process. This would not conserve the stoichiometry of the film, with the deposited film composition changing over time. For III-V epitaxial deposition, separate sources are used and controlled independently (e.g. sublimation of elemental III and V sources).

For III-V epitaxy (e.g. MBE), the conventional three temperature method for thermal deposition is used[67]. The method allows for the growth of extremely stoichiometric III-V films without meticulous control of the fluxes. In this method, two different sources (one for the III element and one for the V element) are used, each with a certain temperature applied to them in order to bring about the required flux via sublimation. The third temperature is that of the substrate in the growth chamber where the deposition occurs. The process is illustrated in Figure 2.2. “A” refers to the group III element, while “B” refers to the group V element, and “AB” is the III-V film (e.g. GaAs). The flux and growth rate for the group III element (e.g. Ga), which is the element with the lowest vapour pressure, is chosen as per the desired overall growth rate for AB. The temperature applied to the Ga source (T_A) is chosen so that the resultant flux (BEP) is significantly above that of the equilibrium vapour pressure

of A over AB ($VP_{A/AB}$) on the substrate (e.g. $BEP >> VP_{A/AB}$) so that that it is in the supersaturation/condensation regime. This way desorption is kept to a minimum and the group three element is deposited, covering the surface. The group V source (B, e.g. As) temperature (T_B) is chosen to get the required V/III flux ratio. A V/III ratio of greater than 1 is usually used (group V rich conditions, $BEP_B > BEP_A$), meaning exact flux specification is not an issue as the excess B (more volatile) can desorb and only the B that is needed bonds to the A covering the surface, maintaining stoichiometry and consuming all A. The substrate temperature (T_{Sub}) is then carefully selected so that pressure is greater than the equilibrium vapor pressure of A over AB and B over AB (supersaturation regime, $P > VP_{A/AB}$, $P > VP_{B/AB}$), ensuring deposition/condensation of the AB film. The pressure should be less than $VP_{B/B}$ however, so as not to condense segregated phases of B and AB. Therefore, B vapour is supersaturated with respect to AB but subsaturated with respect to B. These restrictions on T_{Sub} impose a suitable growth window (condensation window) as shown in Figure 2.2. This also shows that generally $T_A >> T_{Sub}$ when considering the A over AB and A over pure A curves. The method also necessitates that the Gibbs free energy of dissociation of AB is more than that of the vaporization of pure B.

2.1.1 Strained Layer Epitaxy

One of the most important considerations when it comes to semiconductor heterostructure growth and the growth of quantum nanostructures is the compatibility of the materials to be grown atop each other or atop the substrate, and this is chiefly

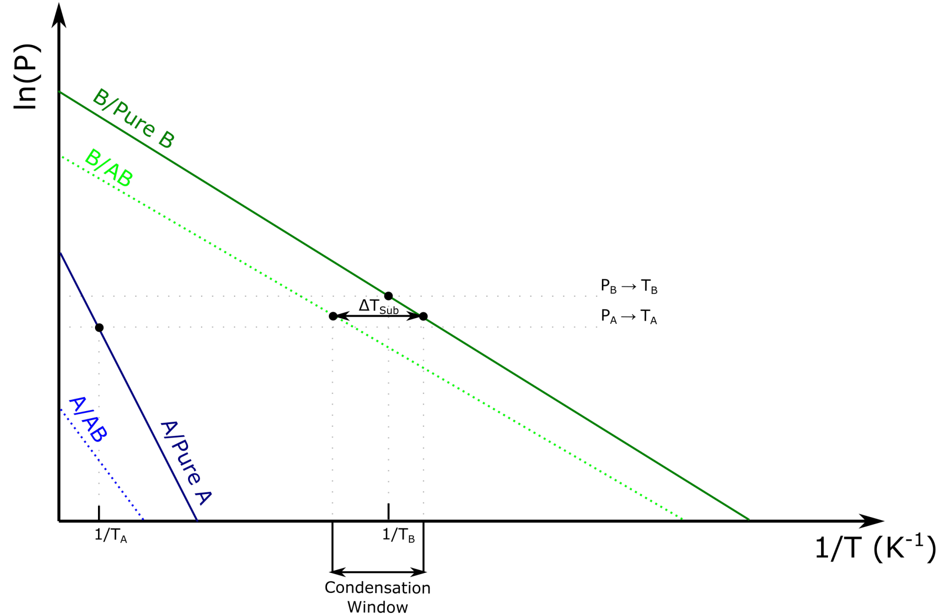

Figure 2.2: A demonstration of the conditions imposed by the three temperature method for the growth of stoichiometric AB (III-V) films. P shown is the BEP (equivalent to deposited fluxes).

manifested in the form of the matching (or lack thereof) of the lattice spacing constant (a) for the materials. Epitaxial growth of lattice mismatched layers can lead to the formation of many types of defects and dislocations in the crystal structure, introducing detrimental carrier traps and recombination centres to the material, and degrading performance. This happens due to the strain imparted on the growing epilayer (depending on the size of the lattice mismatch). The lattice mismatch f is defined as

$$f = \frac{a_{film} - a_{sub}}{a_{film}} \tag{2.1.3}$$

Whether negative or positive strain (tensile or compressive) happens is dependent

on whether the growing layer or starting (substrate) layer has the larger lattice constant (and thus the sign of f), where $a_{film} > a_{sub}$ induces compression and $a_{film} < a_{sub}$ induces expansion (tensile strain). While strain is often a deleterious effect as it is responsible for the formation of defects and dislocations, it can sometimes be desired or even purposefully introduced in order to manipulate the energy bandgap to target different applications[38][68] or to induce/drive the formation of nanostructures, among other uses. Tensile strain decreases the bandgap, while compressive strain has the opposite effect. The degree of lattice mismatch also dictates the amount of material allowed to be deposited before complete irreversible plastic relaxation (and thus dislocations) occur. Where prohibitively large lattice mismatches would mean immediate dislocation as soon as the first monolayers (single atom layers) form, more modest mismatches would allow for the growth of thin films ($\approx$ nm) before plastically relaxing, facilitating for example the growth of narrow QW heterostructures with small mismatches[69]. Growths with minimal lattice mismatches would facilitate the growth of thick films/heterostructures without significant dislocations or defects. This is because as the amount of material deposited on the starting layer/substrate grows, the strain energy steadily increases, till the tipping point where the structure plastically deforms and dislocations are formed in a bid to relax this energy. This imposes a maximum thickness allowed before plastic relaxation depending on the degree of mismatch, and is referred to as the "critical thickness" (d_c), after which dislocations occur. This regime is known as the pseudomorphic growth regime, where elastic strain relaxation exists without inducing dislocations. The strain experienced

by an epilayer (ϵ_f) is defined as

$$\epsilon_f = \frac{a_{film||} - a_{film}}{a_{film}} \tag{2.1.4}$$

where $a_{film||}$ is the in-plane lattice constant for the film, and ϵ_f is the fraction of deviation from the film lattice constant. If $\epsilon_f < f$, the film is partially relaxed. If $\epsilon_f = f$, the film is known as a "coherent" film. For these elastically strained films, the in plane strain is relieved by an out of plane strain. The types of strained layer epitaxy are shown in Figure 2.3. The dislocation shown in the figure is known as a misfit dislocation, and is commonly found in III-V epitaxy for plastically relaxed layers.

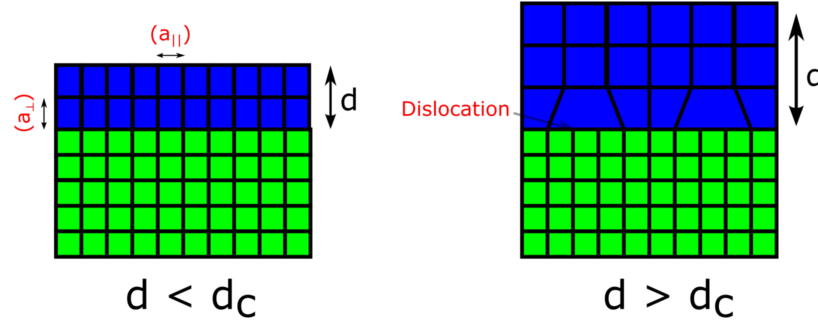

Figure 2.3: Graphical demonstration of the types of strained layer epitaxy. An elastically strained "coherent" film is shown on the left, while a plastically relaxed film with dislocations is shown on the right. In and out of plane strain is shown for strained layers.

The energy of the growing epilayer can be seen as the summation of the energy as a result of the strain and the energy as a result of the dislocations (Matthews-Blakeslee theory)[69]. In this way, strain and dislocation nucleation are coupled together, where strain energy is relieved by dislocation formation and vice versa. Dislocations generally nucleate when doing so would minimize the overall energy. Kinetic considerations

also matter for dislocation formation, such as growth temperature. Higher temperatures could supply the needed energy to form dislocations, thus decreasing d_c. It is also important to note that strain need not necessarily be translated into dislocations for strain relief. The formation of nanostructures on the surface and surface roughening could also form as manifestations of strain relief, depending on the surface energetics (increase of surface area aids in relief). This phenomenon can be observed in the formation of QDs using the SK growth mode. When forming such nanostructures (such as QDs) is desirable, it is important to make sure that they are coherent, and are not accompanied by defect/dislocation formation to maintain satisfactory optical and electrical performance.

2.1.2 Growth Modes

As mentioned, crucial parameters influencing how the growth proceeds are the surface energies of the growing film and substrate. The surface energy is defined as the work needed to create the surface from the bulk. Surfaces and interfaces are generally less energetically favourable than the bulk (excess energy), as the atoms on the surface have higher energies due to incomplete dangling bonds. Surface energy can also be defined as half the energy of cohesion when cutting a bulk sample, with each resultant surface possessing half the energy of cohesion. Depending on surface energy and strain considerations, the growth can yield 2D layer by layer growth (Frank van der Merwe or FM) growth, 3D island (Volmer-Weber or VM growth), or a hybrid 2D + 3D growth mode (Stranski-Krastanov or SK growth). The growth mode is generally dictated by a confluence of symbiotic factors, but can be summarized as a competition between surface, interface, and strain energy (for the dislocation free

growth regime). The growth mode that minimizes the overall free energy (interface + strain + surface) is the mode that occurs during growth, but generally for ($\gamma_{sub} > \gamma_{film}$) FM growth occurs, and ($\gamma_{sub} < \gamma_{film}$) induces VM growth, where γ is the surface energy. This is due to the fact that for ($\gamma_{sub} > \gamma_{film}$), the adhesion of adatoms to the substrate is stronger than its adhesion to its own species (γ can be seen as a measure of adhesion force), reducing mounds and favoring a passivation/wetting of the substrate (2D growth). For ($\gamma_{sub} < \gamma_{film}$), adhesion of adatoms to themselves is stronger, so coalescence of adatoms together to form islands is favoured and 3D growth ensues. Traditionally, the SK growth mode is the preferred mode for QD growth. The conditions for the growth modes are illustrated in Figure 2.4.

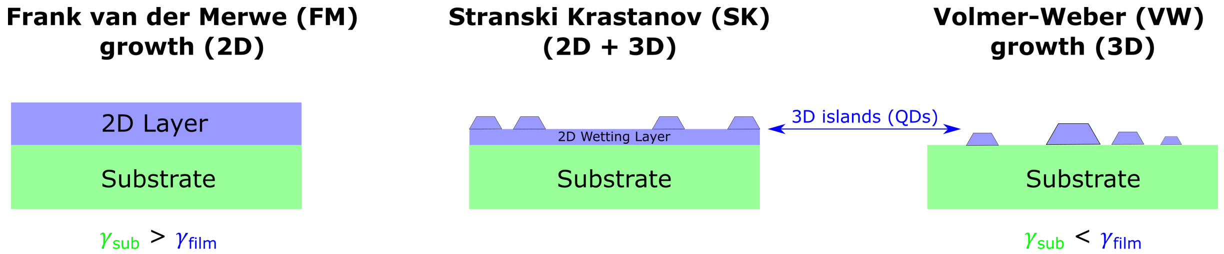

Figure 2.4: Epitaxial growth modes for different surface energy combinations

For the popular InAs/GaAs(100) material system for QD growth, the SK growth mode is readily available when depositing InAs on the GaAs substrate, with a sizable lattice mismatch ($f = 7.2$ %). The presence of this strain is an important factor in provoking SK growth, as this strain energy is relaxed by increasing the surface area and thus forming quantum nanostructures or islands. In SK growth, the first monolayer wets the surface in a 2D (FM) fashion, lowering the surface energies by passivating the dangling bonds, more than the increase in added layers does to the strain energy, so the overall energy decreases (for the InAs/GaAs(100) material system $\gamma_{film:InAs} < \gamma_{sub:GaAs(100)}$). This wetting layer strain changes the

energetics of the growth, and a VW-style island growth occurs (increased surface area) as a method of strain relief, rather than the formation of dislocations. For SK growth, the critical thickness ($d_{c(SK)}$) is the thickness after which the 3D islands start to form after the wetting layer has been established. If the critical thickness for dislocations($d_{c(dislocation)}$) is exceeded, the strain is relaxed plastically and dislocations are formed. These are competing manifestations of strain relaxation, and whichever occurs first (whichever critical thickness is lowest) will dictate the growth mode. After reaching $d_{c(SK)}$, the energy is initially decreased by the formation of islands, then steadily increases as the islands grow and the strain energy increases. For the 2D growth, after the initial wetting later, the strain from the extra layers causes an energy increase till the dislocations are formed after the critical thickness, and the energy is subsequently decreased. The process for growth on an SK mode material system such as InAs/GaAs(100) is illustrated in Figure 2.5.

For other low index GaAs surfaces mentioned in the introduction, ($d_{c(SK)} > d_{c(dislocation)}$), meaning that 2D layers form and if $d_{c(dislocation)}$ is exceeded, dislocations are formed all before any QDs are formed, meaning they are not conducive to QD growth. Bi's use as a surfactant in InAs/GaAs growth has been proven to induce QD growth on GaAs(110)[63][62], meaning Bi decreased $d_{c(SK)}$ to get $d_{c(SK)} < d_{c(dislocation)}$, allowing QD growth by reducing the energetic cost to form QDs. Bi was also found to change $d_{c(SK)}$ depending on Bi flux, and Bi can be introduced after InAs film growth to produce on-demand QDs[63], A similar behaviour and decrease of $d_{c(SK)}$ was shown in preliminary experiments for GaAs(111)[65]. This thesis will explore Bi's influence on these parameters for GaAs(111) growth.

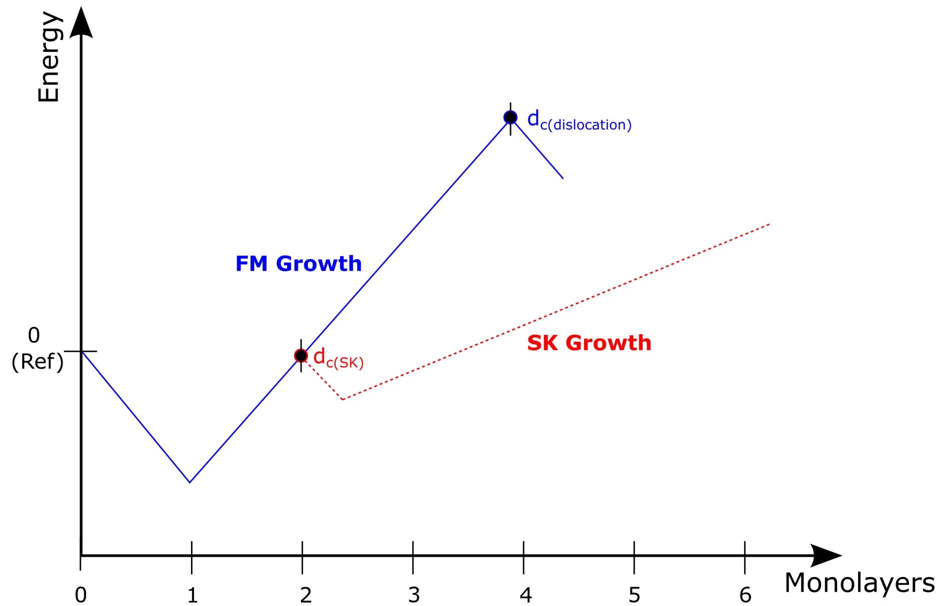

Figure 2.5: Diagram comparing FM vs SK growth for a material system following SK growth such as InAs/GaAs(100), with respect to energy vs. film monolayers grown[5]

2.1.3 Growth Kinetics & Models

To fully understand how growth proceeds and adatom behaviour on the surface, it is important to discuss adatom kinetics. This encompasses adatom interactions, adsorption, diffusion, and desorption on the surface, among other kinetic processes. The kinetics are distinct from the thermodynamics, as kinetics describe the speed or rate of the reaction or process occurring rather than the spontaneity or possibility of occurrence. In the context of the growth kinetics, the Arrhenius relationship is an important one to comprehend, as it governs the rate of many of the processes on the surface where the thermal excitation plays a crucial role (thermally activated processes), such as diffusion/migration and desorption, shown in Figures 2.7 and 2.9. Depending on the surface and growth conditions, adatoms can migrate and hop across the surface to different surface sites/free bonds if they can scale the required diffusion

energy barrier (U_{diff}) (eV) or activation energy for the Arrhenius process, which depends on the surface and crystal structure. Higher temperatures would give the adatom more thermal energy to be able to overcome such barriers and diffuse freely. A similar barrier exists for desorption from the surface (U_{des}). Adatoms bound to free bonds on the surface to minimize their energy oscillate with a characteristic frequency (dependent on the surface and size of adsorbed atom) and try to break free of the bonds in order to hop onto the next site (diffuse) or desorb from the surface with a frequency known as the attempt frequency ν, and is usually on the order of $\approx 10^{13}$ Hz. The rate of desorption and diffusion Γ_{Des} and Γ_{Diff} (s^{-1}) can be defined by an Arrhenius equation as

$$\Gamma_{Des} = \frac{1}{\tau_{Des}} = \nu \cdot e^{\frac{-U_{Des}}{k_B T}} \tag{2.1.5}$$

$$\Gamma_{Diff} = \frac{1}{\tau_{Diff}} = \nu \cdot e^{\frac{-U_{Diff}}{k_B T}} \tag{2.1.6}$$

where the exponential term is a Boltzmann/thermodynamic factor signifying probability, and τ_{Des} is the residence lifetime of the adsorbed species on the surface (or how long it takes for the adatoms to desorb).

For Arrhenius equations, it is possible to extract activation energies by varying the temperature, measuring the subsequent rates and plotting them vs. inverse temperature (Arrhenius plot) as in Figure 2.6, with the y-intercept yielding the attempt frequency ν.

Diffusion can occur in a number of ways, including hopping/jumping to free sites, atomic exchange of adatoms swapping positions, and quantum tunneling through

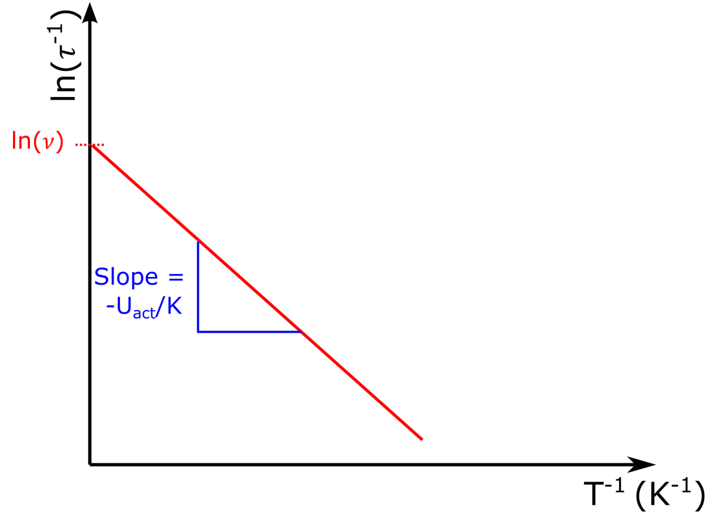

Figure 2.6: Arrhenius plot for thermally activated processes such as desorption and diffusion.

(low) diffusion barriers, even for low temperature adatoms[70]. Adatoms can also diffuse as groups. Generally, $U_{Diff} >> kT$, and therefore $\tau^{-1} << \nu$ (otherwise U_{Diff} would be irrelevant for diffusion). In general $U_{Des} > U_{Diff}$ for diffusion to occur on the surface readily, and so that desorption does not happen instantaneously and dominate the kinetics. Diffusivity is also highly dependent on the orientation, as different crystallographic planes have varying atom densities and plane spacings. Depending on the crystal direction, an anisotropy in diffusion rate can also occur. Diffusivity D ($^{m^2}/_s$) is defined as

$$D = \frac{a^2}{n\tau_{Diff}} \tag{2.1.7}$$

where a is the site spacing, and n is the number of nearest site neighbours (4 for cubic and 6 for hexagonal structures). The diffusion length λ_{Diff} (m) of the adatom on the surface is a metric extracted from random walk statistics, symbolizing the mean

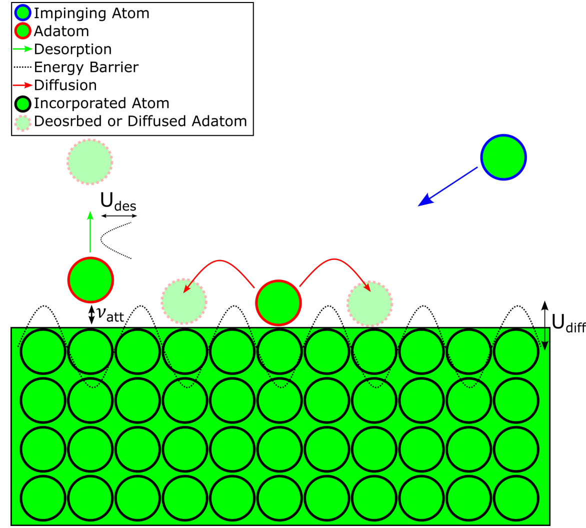

Figure 2.7: Illustration of the different kinetic and Arrhenius processes (diffusion and desorption) experienced by adatoms on the surface.

square displacement of the diffusing adatom. It is an expression of the D while taking into account the surface lifetime (τ_s), or the time the adatom remains active on the surface before desorption or incorporation.

$$\lambda_{Diff} = \sqrt{D\tau_s} \tag{2.1.8}$$

The surface lifetime is limited by both the desorption process (Equation (2.1.5)) and the incorporation process, which is the process in which the adatom sticks to a site, due to island nucleation or attaching to a step edge among other possibilities, forming bonds with several neighbours and solidifying its position, yielding longer τ_s. Depending on the position of the adatom and its surroundings, the binding energy or incorporation could be very strong due to the high number of nearest neighbours (at kinks or nucleating islands) to weak (adsorbed to a single site), as seen in Figure 2.8.

Since ($U_{Des} > U_{Diff}$), desorption is more dependent/sensitive to T, τ_s is limited

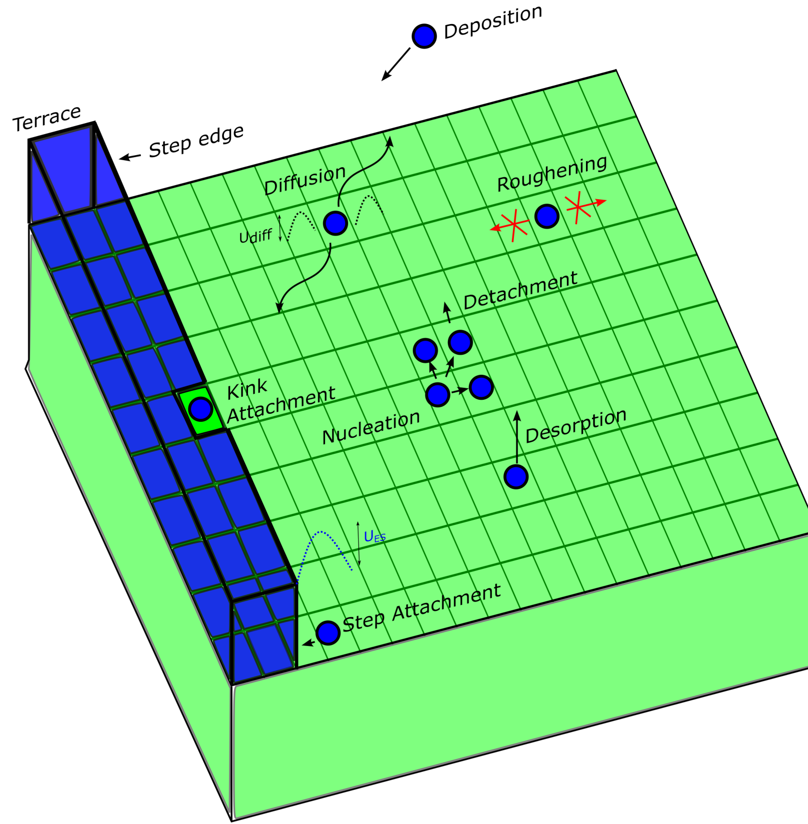

Figure 2.8: Illustration of adatoms interactions on the surface, particularly types of incorporation. The ES barrier can also be observed inhibiting step downhill diffusion.

by desorption for high temperatures ($\tau_s \approx \tau_{Des}$), whereas for low temperatures incorporation limits τ_s. To calculate the number of diffusion hops (h) for the desorption limited regime, the diffusion rate is divided by the desorption rate to get

$$h = \frac{\Gamma_{Diff}}{\Gamma_{Des}} = \frac{\tau_{Des}}{\tau_{Diff}} = \frac{\nu \cdot e^{-U_{Diff}/kT}}{\nu \cdot e^{-U_{Des}/kT}} = e^{-(U_{Diff}-U_{Des})/kT} \tag{2.1.9}$$

The diffusion length (λ_{Diff}) has a profound impact on the growth dynamics. High λ_{Diff} allows adatoms to diffuse freely across the surface and to meet other adatoms and start nucleating/forming flat 2D islands, increasing horizontally in size. With

surfaces that have a significant ES barrier, this could drive vertical growth of the island gaining height due to the stifling of downhill diffusion. Smooth 2D layers could form when these islands remain flat and expand to meet other islands, creating a flat 2D coverage of the surface and thus a monolayer. This process consisting of island formation, expansion, and coverage is repeated above the 2D layer to give 2D layer by layer FM growth. 2D monolayer formation time t_{ML} (s) can be defined as

$$t_{ML} = \frac{N_s}{z} \tag{2.1.10}$$

where N_s is the number of adsorption surface sites in the surface, and assuming the probability of the deposited adatom to adsorb and stick to the surface without desorption is 1.

Low λ_{Diff} (as a result of a low temperature for example) contributes to roughening as the adatoms stick to their positions, increasing the density of incorporated adatoms sparsely populated at random positions on the surface, resulting in roughening as coherent islands cannot be formed due to a lack of adatom mobility. Therefore the adatoms cannot reach the favorable incorporation positions at kinks, step edges, and the forming flat islands as described in the 2D layer growth process, creating rough surfaces.

For vicinal substrates with a nominal offcut (not perfectly flat, but with inherent step edges), step-flow growth could commence if λ_{Diff} is sufficiently high (Figure 2.9). For step-flow growth to occur, λ_{Diff} should be greater than the terrace width in order to facilitate incorporation to the step edges and not nucleate islands on the terraces. In this growth regime the adatoms attach to the step edges (as they are favourable binding positions) so the steps keep growing. Some steps can grow faster

and wider than others (step bunching) or the steps can grow at a uniform rate with equal widths (step-antibunching). The steps grow with a certain velocity depending on the growth rate, and in the direction of the substrate offcut. In either case the final grown epilayer is a stepped surface, like the starting substrate.

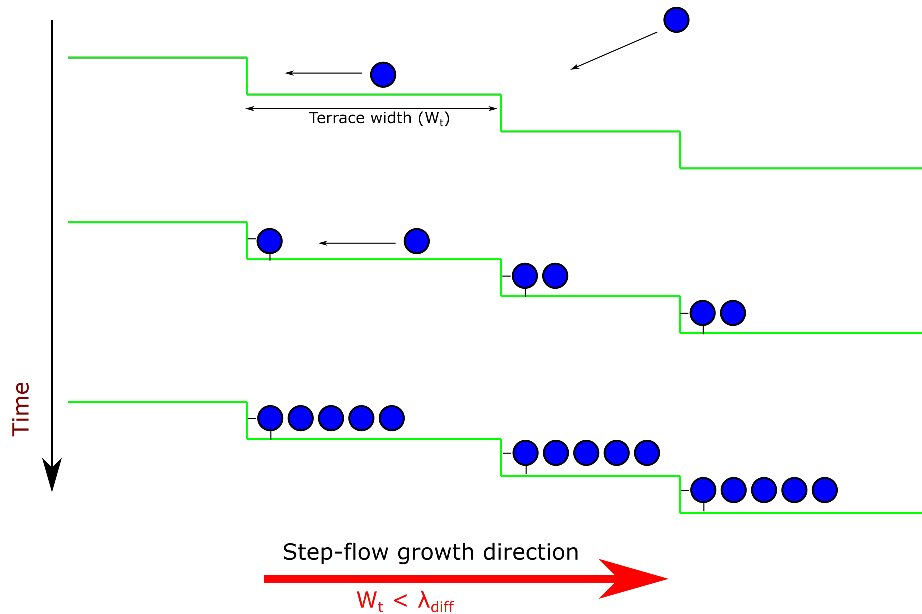

Figure 2.9: The process of step-flow growth as the growth progresses. This occurs at $W_t < \lambda_{Diff}$

To describe the coverage of deposited adatoms and the formation of monolayers on the surface, several models have been considered, the most simple and prominent of which is the Langmuir adsorption isotherm model. In this model, adsorption is considered for empty sites only, so no island nucleation or multi-monolayer structures are considered (adatoms can only adsorb to empty sites). In addition, no adatom-adatom interactions are taken into account, and diffusion is neglected. Multiple adsorption is also not allowed, and all empty sites have identical characteristics. Therefore assuming the coverage (θ) of the surface is between 0 and 1, and an impinging flux z

provides adatoms that stick with 100% probability to only empty surface sites, and that the only process working to decrease this coverage and counteracting the adsorption is the desorption processes (which is governed by an Arrhenius relationship), the rate of change of θ can be given as[71]

$$\frac{d\theta}{dt} = (\frac{(1-\theta)z}{N_s}) - \theta\nu e^{\frac{-U_{Des}}{k_B T}} \tag{2.1.11}$$

where the first term on the right hand side of the equation is the adsorption term, considering only empty sites $(1 - \theta)$, and the second one is the desorption term, considering only filled sites θ. To solve for the steady state coverage at a given flux, $\frac{d\theta}{dt} = 0$ to yield

$$\theta = \frac{z}{z + \nu N_s \mathrm{e}^{\frac{-U_{Des}}{k_B T}}} \tag{2.1.12}$$

$$\theta = \frac{QP}{1 + QP} \tag{2.1.13}$$

where

$$Q = \frac{\mathrm{e}^{\frac{U_{Des}}{k_B T}}}{\nu N_s \sqrt{2\pi m k_B T}} \tag{2.1.14}$$

An estimate of Equation (2.1.14) representing the Langmuir adsorption isotherm is plotted in Figure 2.10. The Langmuir model, while adequate and quite powerful in its simplicity for singular monolayer formation, does not accurately model film formation at high BEP or fluxes (when molecules start to stick to other admolecules and bulk condensation occurs) and presupposes strong adsorption of adatoms to the surface, so that inter-adatom or inter-admolecular interactions are neglected in light of the

adsorption to the surface/substrate. A more detailed model, and thus more accurate for these conditions, is the Brunauer-Emmett-Teller (BET) model[72], which models multilayer adsorption and takes into account the interactions between the adsorbent species. For the work in this thesis, the Langmuir model will be discussed in modeling the coverage of Bi. The choice of the simpler model is sufficient and justified, as the discussion will be related to monolayer formation of Bi, as the growth conditions used for Bi surfactant investigation do not yield bulk Bi condensation.

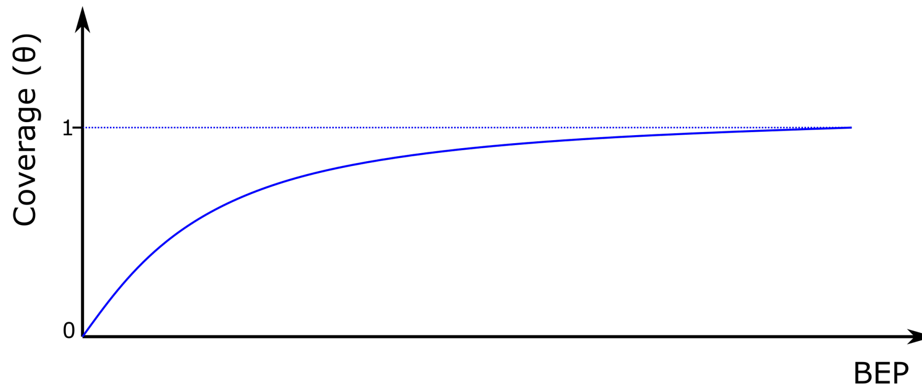

Figure 2.10: A rough sketch and comparison of the coverage as predicted by the Langmuir model as a function of BEP.

2.1.4 Surface Reconstructions

As mentioned so far in this thesis, the surface of a material harbours distinctly different properties from the bulk, as a consequence of the lower number of atoms the surface atoms are bonded to. In this respect, they have a higher energy than the bulk atoms and are more reactive, since there are many unfulfilled dangling bonds on the surface driving up the energy of the surface. Surfaces are created by cleaving the bulk and cutting these bonds, and the stronger these bonds were (e.g. covalent bonds) the

higher the surface energy due to the high energy of the dangling bonds. For these surface atoms this is an unstable situation, and this high reactivity could readily result in oxidation or the incorporation of impurities, which is one of the reasons why thin films are grown in UHV to minimize this possibility. In the absence of any way to passivate the surface, the surface atoms, which are freer than their bulk counterparts due to the lack of a top layer of atoms pinning them into position, have some freedom to regroup on the surface into a minimum energy position (an example is shown in Figure 2.11). This minimizes the surface energies and satisfies some of the bonds at the expense of some elastic strain with respect to the surface atoms' bonds with the bulk. This process can result in a relaxation of the layer (change in position of entire surface layer closer to the bulk) or a total reconstruction of the layer, with the surface atoms taking on different periodicities than the bulk atoms. Diamond/zincblende materials such as III-V semiconductors tend to form sp^3 hybridized orbitals to create 4 bonds to bond to their nearest neighbours covalently, and a reconstruction can happen by forming bonds using hybridized orbitals to minimize dangling bond energy. Changes in the reconstruction intensify with the introduction of adsorbed atoms and molecules on the surface or during deposition, with more radical reconstructions being possible, particularly for strongly adsorbed (chemisorbed) species. Layers can undergo a conservative reconstruction, with the number of atoms staying the same after the reconstruction, or non conservative, with the number of atoms on the surface changing (e.g. desorption). The surface reconstruction can influence the subsequent growth on the surface, and can be altered depending on the growth conditions like flux and temperature, and thus it is important to monitor during growth to fully deduce what is occurring on the surface.

Reconstruction notation denotes the periodicites of the surface atoms compared to the bulk. Using the translation vectors for the lattice defining the unit cell of the structure on the surface $(\vec{a}, \vec{b})$, for a surface reconstruction with twice the periodicity in the $\vec{a}$ direction but the same bulk periodicity in the $\vec{b}$ direction and at an angle ϕ, the notation would be $(2 \times 1)R = \phi$. This case is laid out in Figure 2.12. GaAs(001) has exhibited a (2×4) reconstruction under typical growth conditions[73], meaning the unit cell on the surface is twice as long along the $[1\bar{1}0]$ direction and four times as long along the [110] direction (compared to bulk periodicity). GaAs(111)A has been shown to have a (2×2) reconstruction, while GaAs(111)B has exhibited $(\sqrt{19} \times \sqrt{19})R = \pm 23.4°$ in addition to the (2×2) reconstruction[74].

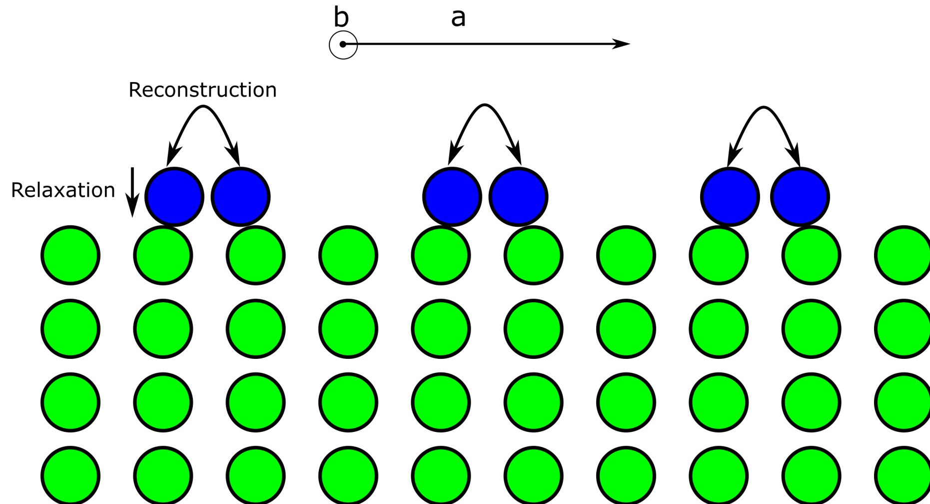

Figure 2.11: A rough diagram detailing an example of a $(2\times)$ surface reconstruction and a relaxation of the surface layer. The $\vec{b}$ direction points out of the page.

2.2 Molecular Beam Epitaxy (MBE)

MBE is one of the most advanced and precise methods used for epitaxial growth. Materials are deposited in a UHV environment ($10^{-8} - 10^{-12}$ Torr) to ensure maximum purity of the film and the absence of contaminants. A schematic of an MBE system is shown in Figure 2.12. The system consists of a load-lock, where the substrate is first placed, and then is transferred via the preparation chamber and valve to the growth chamber, where the growth commences under UHV conditions. The UHV environment elongates the mean free path ($\approx$ km) of the gasses/evaporated material being deposited, allowing them to form highly directional beams impinging on the surface, and inhibiting the interaction of these beams with each other during deposition. Due to the large mean free path and the vacuum, the fluxes are entirely dependent on the temperature applied to the effusion cells and the control of the shutters, with impurities (e.g. $\mathrm{H_2, O_2, C}$) inhibited from depositing due to their very low concentrations when contrasted with the molecular beams. To maintain this vacuum, a variety of pumps are used at different vacuum levels. The load-lock is kept at (5×10^{-6} Torr) using roughing and turbo-molecular pumps, while the growth chamber is pumped to achieve the UHV conditions. The substrate sits atop a molybdenum wafer holder due to its high thermal tolerance. Interaction occurs when both beams condense and crystallize on the substrate, which is heated by a heating coil. The growth is largely characterized by the rate of arrival of the deposited atoms on the surface, namely the growth rate (of the resultant film), which is limited to around $\approx 1\ ^{\mu m}/_{hr}$. Substrate temperature can be monitored either by a thermocouple installed in the vicinity of the substrate, or using a pyrometer in which the black-body radiation of the substrate is captured and from which the true temperature of the

substrate can be deduced. These two methods are employed in the MBE system used for the work in this thesis. Flux monitors/gauges are used to monitor the pressure inside the chamber and measure flux BEPs. To help maintain vacuum and filter out impurities from the chamber, a liquid nitrogen-cooled shroud is used in the growth chamber to condense volatile gasses and water vapour, which is then pumped out of the system/growth chamber. Effusion cells housing the constituent source materials (e.g. pure Ga and As for GaAs growth) and for dopants are heated to thermally evaporate the material into the growth chamber via sublimation (solid source MBE or SSMBE). Some MBE systems utilize gas sources rather than sublimation-based solid ones. In this sense, gas-source MBEs (GSMBE) or hydride-source MBEs can be seen as a crossover between CVD and chemical techniques with physical ones such as SSMBE. GSMBEs are considered as chemical beam epitaxy techniques, as the UHV also forces the carrier gas to act as a gaseous beam till it reaches the substrate surface rather than the atomic beams in SSMBE. GSMBEs give better control of the flux, but may introduce contaminants such as H_2 from the gas sources. SSMBE uses elemental solid As sublimation to produce As_4, which has a low sticking probability. Therefore, an arsenic cracker is needed to heat the arsenic tetramer As_4 gas (800-1000 °C) to create As_2 dimers. For GSMBE (as used in this thesis) the cracker is used to crack arsine gas (AsH_3) with H_2 as a by-product. Cracked species (such as As_2) stick easier to the surface, first by weakly adsorbing onto the surface then undergoing dissociative adsorption to finally strongly adsorb and incorporate on the surface as monomers. For SSMBE, this large As_4 production requires high pumping speeds to get rid of the excess arsenic (growths usually occur in group V rich conditions). In addition, large fluxes for SSMBE necessitate large effusion cells (solid source). In the GSMBE used

in this thesis, AsH_3 is used as the As source (with a cracker), and solid elemental sources (sublimation) are used for Ga and Bi. The MBE system used was a GSMBE from SVT Associates [75] housed in the Centre for Emerging Device Technologies (CEDT) at McMaster University. Further details about the MBE system used are given in chapter 3.

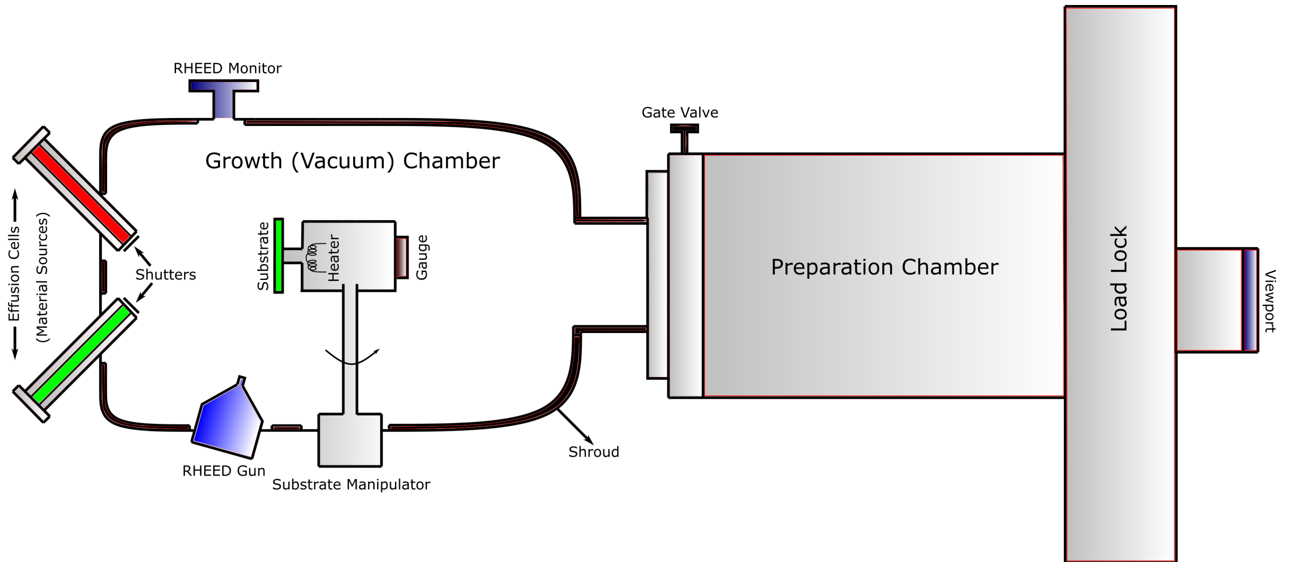

Figure 2.12: A schematic of an MBE system.

2.3 Metal-organic Chemical Vapour Deposition (MOCVD)

MOCVD is a chemical epitaxial technique used to produce crystalline films, without using a high vacuum environment. This technique employs the use of gas precursors containing the group V and III elements to be grown, carried by a carrier gas to the reaction chamber, where the gasses are mixed and passed over the substrate (horizontal reactor MOCVD) or introduced via a showerhead-like structure (vertical reactor),

where pyrolysis or thermal decomposition of the mixture ensues, depositing the III-V material. The MOCVD system used in this thesis utilizes a showerhead/vertical reactor. The substrate sits atop a graphite holder/susceptor and is heated using a coil. The growth is based on the gasses being in the supersaturation regime, with gas pressures ranging from 10 to 760 Torr. This permits the use of much higher fluxes and growth rates than those used in MBE. Hydride sources are used for the group V elements (e.g. arsine or AsH_3 for As), while metal-organic precursors are used for the group III elements (e.g. trimethyl-gallium or $Ga(CH_3)_3$ for Ga). Triethyl species are also sometimes used for group III elements, as are alkyls for group V (e.g. tertiary-butyl arsine or TBA). Metal-organic precursors are volatile and can undergo thermal decomposition at relatively attainable temperatures ($\approx$ 500 °C). The temperature needed for pyrolysis differs depending on the strength of the bonds of the precursor, with more carbon atoms meaning a weaker bond and a lower required substrate temperature to induce the decomposition and hence the reaction. The precursors are transported by the aforementioned carrier gas (typically H_2) which should be inert to reduce interaction and maintain purity as they constitute most of the gas. N_2 is also used as a carrier due to its inertness and effectiveness in cracking the metal-organic molecules due to its increased mass, enhancing purity.

A typical MOCVD reactor consists of a reaction chamber (Figure 2.13) where the growth takes place, gas and bubbler cylinders for the source and carrier gasses, and mass flow controllers and valves to regulate the flow and fluxes leading to the chamber. The group III and V sources are stored separately. The bubbler cylinders house the metal-organic group III precursors in liquid form, such as Trimethyl-gallium (TMGa), and the gas cylinders house the group V hydride sources (e.g. AsH_3) and

dopants. The bubbler cylinders are kept in a thermal bath and their vapour pressure is regulated. The carrier gas is passed through the bubbler and depending on the bubbler temperature, a certain amount of the precursors will be carried to the reaction chamber. Therefore it is the carrier gas flow rate and the bubbler temperature that determine the deposition rate and thus the growth rate. After the reaction occurs and the material is deposited, the remaining gasses and reaction products (e.g. CH_4) are then pumped out after dilution and scrubbing and passed to the exhaust.

Comparing both MBE and MOCVD as the premier epitaxial growth techniques for III-V epitaxy (Figure 2.13), MBE is characterized by numerous advantages. These include the ability to create abrupt doping profiles and thin heterostructures due to the accuracy and precision of the beams, as well as being able to create extremely pure films thanks to the UHV environment. For SSMBE, the process is also relatively simple, not necessitating carrier gasses which need high temperatures to react on the surface and deposit the materials, and adding/integrating new sources is relatively straightforward. UHV also facilitates the use of *in-situ* characterization techniques to monitor the growth as it proceeds, such as Reflection High Energy Diffraction (RHEED), which will be expanded upon later in this chapter. In addition, SSMBE does not utilize highly dangerous and toxic hydride group V sources, and GSMBE at least do not do so at high pressures. Despite these many advantages, MBE has been largely relegated to the realm of research and development and its commercial use has been sparse, owing to its limited growth rates when compared to chemical techniques (e.g. MOCVD), and its limited scalability and thus limited commercial viability. The significant advantages of MOCVD in cost and scalability while still maintaining the purity of crystalline films mean both techniques are highly relevant, and both will

be explored in this thesis in the context of the growth of GaAs(111) homoepitaxial films using surfactants. For the growth procedures in chapter 4, an industrial-grade, low pressure MOCVD system provided by Structured Material Industries (SMI)[76] was used in the CEDT. The system utilizes a vertical growth chamber with a close-coupled showerhead reactor, and the carrier gas used was H_2. The precursors used were TMGa and TEGa for Ga and AsH_3 for As.

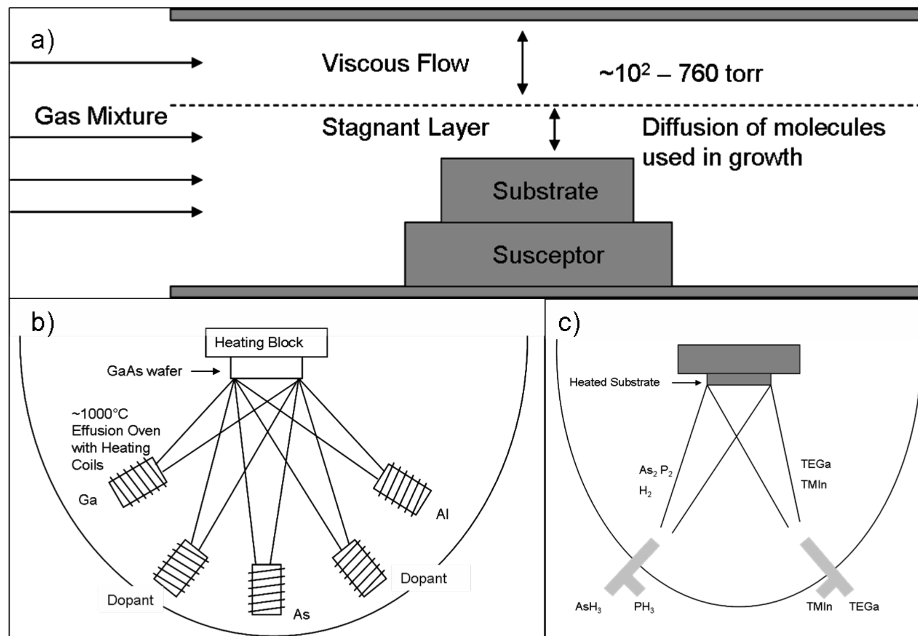

Figure 2.13: A comparison of the growth chambers of a) MOCVD, b) SSMBE, and c) GSMBE. Figure adapted from Wikipedia commons under a free license.

2.4 Atomic Force Microscopy (AFM)

Atomic force microscopy is an imaging technique belonging to a family of microscopy techniques known as scanning probe microscopy (SPM). This technique is capable of imaging surfaces at sub-nanometre resolutions and is the most popular technique

used for gathering high-resolution topographical surface images and height data of samples.

The basic working principle of AFM is the use of a fine tip (radius of curvature ≈ nm) on a silicon or silicon nitride springy cantilever (with a certain spring constant) to horizontally scan the sample surface, with the tip tracing the sample topography and height. The tip is kept in place while the platform/stage housing the sample moves in a raster fashion, with the aid of piezoelectric actuators producing fine movements. This typical AFM setup is shown in Figure 2.14. The raster motion occurs till the tip covers the entirety of the selected sample area, thus creating the image. As the tip completes the scan, the tip reacts or deflects to a degree depending on the force imparted on it as a result of the proximity of the tip to the surface. These forces causing the deflection as a consequence of the proximity could be as a result of direct mechanical contact (contact mode AFM), van der Waals forces, or electrostatic forces. In contact mode AFM, the tip is directly touching the sample (or a formed adsorbed fluid layer) as the scan progresses. The force can be calculated using Hooke's law and the deflection is measured. This mode yields high scan speeds and is useful for rough jagged surfaces with dramatic height fluctuations, but the constant direct contact could damage the sample, and shear forces resultant from direct contact could result in a misleading image. In tapping mode, the tip oscillates with a frequency below the resonant frequency of the cantilever, with oscillation amplitudes on the order of tens of nanometres. The resonant frequency depends on the forces affecting the tip due to the proximity of the surface, and as the tip approaches to tap the surface, the amplitude of the oscillation decreases. This damping of the oscillation and thus change in the amplitude of the deflection can be used to extract the height

of the sample at that given point. For this mode, alteration/damage to the sample is minimized at the expense of scanning speed, and shear forces are absent. A non-contact mode also can be used with the tip oscillating but not touching the surface (unlike tapping mode, which taps it), relying on long range van der Waals forces to modulate the oscillation and amplitude depending on the surface. This method is ideal for soft samples but usually requires to be operated in a vacuum to allow the tip to operate without getting trapped in the adsorbed fluid layer, and slower speeds must be used. For the purposes of imaging epitaxial semiconductor thin films, tapping mode is commonly used and is what will be used in this thesis.

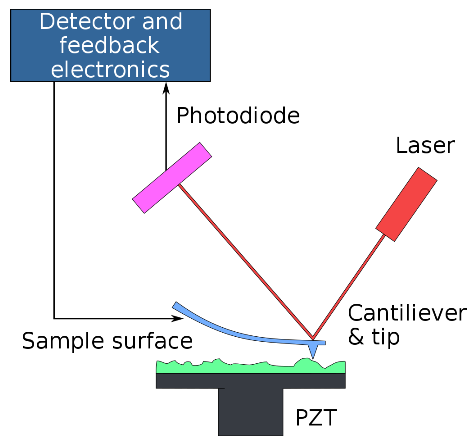

Figure 2.14: A block diagram illustrating the components of a typical AFM tool. Figure adapted from Wikipedia commons under a free license.

For deflection measurement, the deflection is most commonly acquired using optical techniques. As the scan occurs, a laser beam is pointed on the scanning tip and the beam is reflected by the tip and collected into a four quadrant photodetector. Depending on the angle of reflection (which differs depending on the tip height/position and thus reflection), one photodetector measures a value different from the other, and using the difference between the two readings, it is possible to calculate the degree of

the deflection and thus the height of the sample at that given coordinate. Feedback electronics help keep the oscillation constant by defining a specific set point. Other beam deflection measurement techniques can be used, such as the use of optical interferometry or the detection of Doppler shifts from the vibrating tip[77][78].

The AFM apparatus described, while first envisioned as an imaging technique, has also found use as a tool to measure force, and thus used in force spectroscopy to measure the mechanical properties of a sample, and as a manipulator, whereby the tip is used to interact with nanostructures, for nanoparticle assembly, and even atom manipulation on the surface[79].

AFM will be used in this thesis primarily for the measurement of the roughness of the grown films, as well as to probe the surface morphology of the grown GaAs(111) films with and without surfactants in order to investigate their behaviour. Two AFM tools were used in this thesis. The main one was a MFP-3D atomic force microscope (Asylum Research[80]) in tapping mode. The other one was the Anton-Paar Tosca 400 AFM[81] housed in the McMaster Manufacturing Research Institute (MMRI), also in tapping mode. The tips used had a resonance frequency of 300 KHz and a radius below 10 nm (for both systems). The Asylum Research AFM tool was used unless otherwise stated.

2.5 Reflection High Energy Electron Diffraction (RHEED)

Reflection High Energy Electron Diffraction (RHEED) is one of the chief methods used in MBE for *in-situ* monitoring of the growth and of surface processes. It is an

electron diffraction technique, similar to transmission electron microscopy, but specifically for interrogating crystal surfaces. An electron or RHEED gun is used to generate a high energy electron beam (e-beam), which is directed at the sample crystal (i.e. the growing film) as the growth progresses. The high e-beam energy ($\approx$ 20 keV) gives the beam a very small de Broglie wavelength ($\lambda \approx 0.06$ nm for the aforementioned energy), rendering it on the order of or smaller than the lattice/plane spacing of the crystal, allowing the e-beam to act as a wave suitable for undergoing diffraction, and facilitating the gleaning of surface information from the resultant diffraction pattern following constructive interference. The *in-situ* nature of the characterization is only possible due to the UHV conditions of the MBE technique. The e-beam strikes the surface at a grazing angle of incidence which is usually only a few degrees. The e-beam grazes the surface, entering only the first few monolayers, and then diffracts due to the atoms in the lattice site positions. The diffracted e-beam then exits the surface, striking a fluorescent screen to show the RHEED diffraction pattern.

The general Laue diffraction (assuming conservation of crystal momentum) condition for constructive interference from a beam interacting with a crystal lattice is given by[82]

$$\vec{k_D} - \vec{k_I} = \vec{G} \tag{2.5.1}$$

where the input and diffracted output beams have a momentum of $\vec{k_I}$ and $\vec{k_D}$, and $\vec{G}$ (m^{-1}) is the reciprocal lattice vector. The reciprocal lattice is the Fourier transform of the physical real lattice, where a physical crystal plane spacing of d is translated into $^{2\pi}/_{d}$ for the reciprocal lattice, with points on the reciprocal lattice representing families of crystallographic planes. The reciprocal lattice is the pattern found to represent

the spatial one after interrogation via diffraction, and is thus a crucial concept for crystallography and diffraction as a characterization tool.

Assuming conservation of energy, it is clear that

$$\left|\vec{k_I}\right| = \left|\vec{k_D}\right| = \frac{2\pi}{\lambda} \tag{2.5.2}$$

It is important to note that by restricting the analysis to elastic scattering conditions as implied by the previous equation, with some simplification, the general Laue condition in Equation (2.5.1) can be reduced to the famous Bragg condition without loss of generality. The angle between $\vec{k_I}$ and $\vec{k_D}$, θ_D , is the diffraction angle. As in Figure 2.15, the reciprocal lattice is represented as extremely long rods rather than points due to the 2D nature of surfaces (RHEED characterizes the surface only) with respect to the 3D bulk, where the spatial constraint of the perpendicular out-of place direction causes an elongation in the reciprocal lattice due to the inverse relationship between them. The input and diffraction wavevectors can construct a sphere (circle in 2D) known as the Ewald sphere, whereby according to the condition in Equation (2.5.1), an intersection of this sphere and any of the reciprocal lattice rods would satisfy the Laue condition, yielding constructive interference and a diffraction pattern.

Figure 2.15, shows the multiple diffraction orders possible from the multiple intersections between the elongated lattice rods and the Ewald sphere, as well as the different Laue circles/zones. The spacing between RHEED spots is r and the distance between the sample and the RHEED screen is R. The notation for each interference spot depending on the Laue zone and angle of diffraction is also shown, with the least diffracted angle being called the specular spot and denoted as (0,0). Due to the

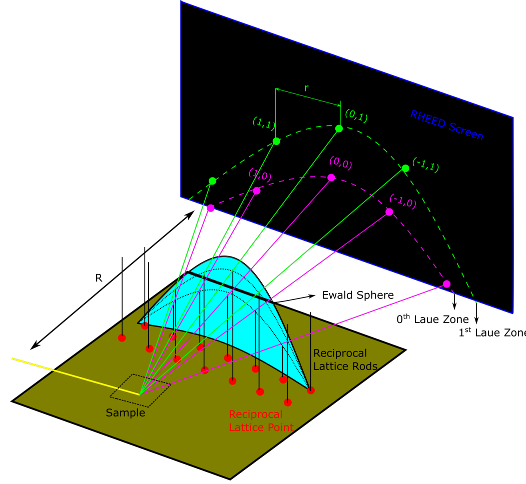

Figure 2.15: 3D sectional view sketch of intersection of Ewald sphere with lattice rods, yielding spots on the screen.

very small wavelength and thus the large value of $\left|\vec{k_I}\right|$ and $\left|\vec{k_D}\right|$, and the very closely-packed rods with a spacing of d, the rods can be seen as bundling up to form some sort of mesh-like plane made out of rods. The intersection of these "planes" with the sphere gives the Laue circles. As a result of the large circle radius, ($\vec{k_I} >> \vec{G}$), θ_D is very small and one can approximate $\vec{k_I}$ to be perpendicular to $\vec{G}$. Using the small angle approximation and geometrical arguments from Figure 2.15

$$sin(\theta_D) \approx \frac{\left|\vec{G}\right|}{\left|\vec{k_I}\right|} \approx \frac{r}{R} = \frac{\lambda}{d} \tag{2.5.3}$$

To ensure intersection, the sample can be tilted (shifting reciprocal lattice rods) or e-beam energy (and thus λ) changed. It is obvious that the reciprocal lattice, and thus the diffraction pattern, is highly dependent on the physical structure of the real surface lattice and thus RHEED and other electron diffraction techniques are a potent tool for probing the crystal surface. In RHEED's case, it is an extremely

powerful technique for monitoring growth, nucleation, and surface dynamics, and thus crucially the aforementioned surface reconstructions, with certain RHEED patterns corresponding to certain reconstructions. The periodicity of the spots/streaks in the pattern symbolizes periodicity on the surface as shown in Figure 2.17.

RHEED pattern intensity is also a key metric to consider when attempting to deduce what is going on at the surface. It has been used to monitor the state of the growth as shown in Figure 2.16, with more rough incomplete layer growth (or those with an abundance of islands) increasing scattering and giving off a diffuse, low intensity glow, while smoother surfaces give high specular intensities. The intensity tends to cycle between these two extremes as the growth progresses, giving an account of surface conditions while also allowing for the measurement of monolayer formation time.

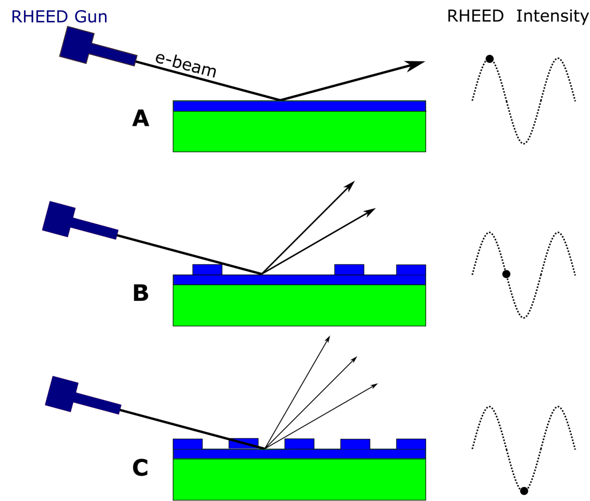

Figure 2.16: RHEED intensity variation as the growth progresses. A) symbolizes a fully formed smooth surface/epilayer (blue), B) symbolizes a growing epilayer with partial coverage, and C) represents the low point for the intensity at peak surface roughness. After C) the intensity climbs as the layer forms into a complete one, returning to A) once more and thus completing a monolayer growth cycle.

The monitoring of RHEED patterns as a reflection of adatom behaviour on the surface during epitaxial growths, such as the monitoring of desorption times, surface smoothness during growth, oxide removal, and surface reconstructions will be used in the work in this thesis.

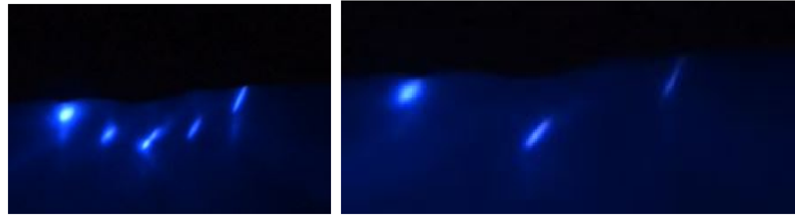

Figure 2.17: RHEED patterns for GaAs(111)A homoepitaxial growth, which will be elaborated upon in chapter 3. A 2×2 reconstruction, meaning the periodicity of the surface is twice the bulk, is shown on the left and a (1×1) pattern implying a surface reconstruction (during Bi deposition on GaAs(111) with identical surface periodicity to the bulk is shown on the right.

Chapter 3

Bi as a Surfactant for MBE of GaAs(111)

In this chapter, the behaviour of Bi as a surfactant on GaAs(111) is investigated. A process for calibrating the new Bi source is outlined and the source is used to explore Bi adatom action on GaAs(111)A. Bi is shown to act as a surfactant under certain growth conditions, inducing atomically-smooth stepped GaAs(111)A buffer layers when employed in GaAs(111)A MBE homoepitaxy. Greater Bi fluxes are shown to create smoother surfaces, and Bi is proven to also drive step anti-bunching, evening out step widths. A RHEED-based experiment is also proposed to measure the desorption energy barrier, by measuring the RHEED streak intensity change as Bi desorbs.

3.1 Calibration of the Bi source

A new solid Bi source/effusion cell was procured and installed into the hydride source/gas source MBE system (GSMBE from SVT Associates[75]) used in the Centre

Temperature (°C)	**BEP (Bi OFF)**	**BEP (Bi ON)**	***Net BEP***
750	4.81×10^{-9}	3.33×10^{-7}	$\mathbf{3.23 \times 10^{-7}}$
725	4.57×10^{-9}	2.18×10^{-7}	$\mathbf{2.13 \times 10^{-7}}$
700	3.09×10^{-9}	1.31×10^{-7}	$\mathbf{1.28 \times 10^{-7}}$
675	2.46×10^{-9}	8.3×10^{-8}	$\mathbf{8.05 \times 10^{-8}}$
650	2.12×10^{-9}	4.99×10^{-8}	$\mathbf{4.78 \times 10^{-8}}$
625	1.93×10^{-9}	2.86×10^{-8}	$\mathbf{2.67 \times 10^{-8}}$
600	1.81×10^{-9}	1.59×10^{-8}	$\mathbf{1.41 \times 10^{-8}}$
575	1.71×10^{-9}	8.65×10^{-9}	$\mathbf{6.94 \times 10^{-9}}$
550	1.63×10^{-9}	4.85×10^{-9}	$\mathbf{3.22 \times 10^{-9}}$
525	1.63×10^{-9}	3.13×10^{-9}	$\mathbf{1.52 \times 10^{-9}}$

Table 3.1: Ion gauge BEP (Torr) readings for the Bi cell at different temperatures.

for Emerging Device Technologies (CEDT), where the epitaxial growth was carried out. Before use, the source needed to be properly calibrated to ensure sound operation and control. The goal of the calibration procedure was to find the relationship between the heat and thus temperature applied to the cell and the flux resulting from the evaporation of the solid Bi material, and thus the flux.

Different temperatures were applied to the cell and the resultant BEPs were measured using an ionization gauge. This step is necessary to deduce the general relationship between the temperature and the flux before calibration. Flux values are measured while the Bi shutter is both on and off, with the difference corresponding to the net Bi BEP. BEP is given in units of Torr. The values are recorded in Table 3.1. There is clearly a proportional relationship exhibited with regards to the temperature and BEP, as expected. It is also expected that the relationship will be an Arrhenius one, given the nature of the thermally-activated reaction of the evaporation.

Now that the general trend has been obtained, it is important to define the actual flux for a given temperature data-point to calibrate the data, and for it to reflect

the true amount of material deposited on a substrate as a result of the flux. This data-point will then be compared to the BEP reading of the same temperature to find the BEP to flux calibration factor, where BEP is assumed to be proportional to the flux.

To obtain this data-point, Bi was deposited for 4 minutes on a Si substrate with a certain temperature being applied to the cell (750 °C). The amount of deposited Bi material was then estimated using AFM and image processing techniques. The AFM scan is shown in Figure 3.1.

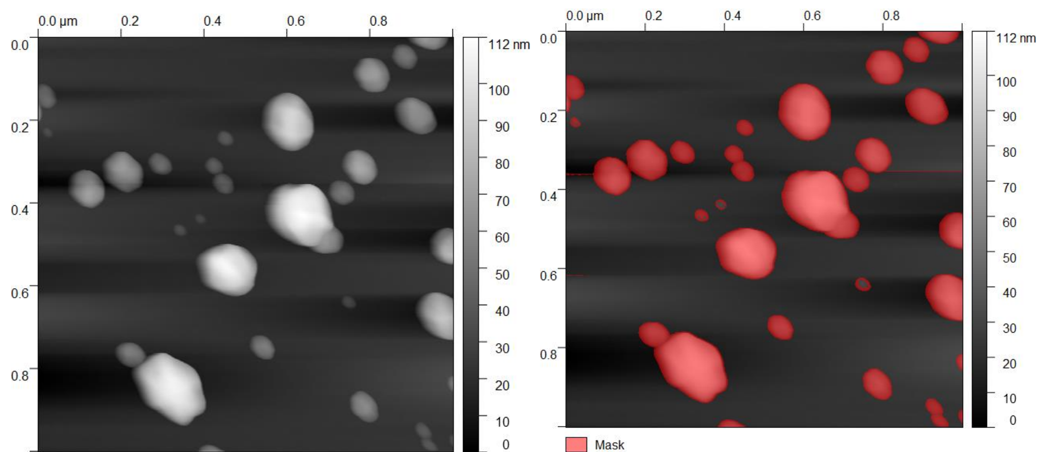

Figure 3.1: Bi deposited on a Si substrate for calibration purposes. The volume of the Bi droplets is calculated and used to calculated the deposited flux. Sample #2116.

All AFM images in this thesis were processed using Gwyddion open source software for scanning probe microscope data visualization and analysis[83] unless otherwise stated. The image was first processed by leveling/flattening the data by mean plane subtraction to remove macroscopic tilt, then aligning horizontal rows using the median method, before correcting horizontal scars and shifting the minimum data value to zero.

Mask threshold parameter:	Value
Height	28.7% (32.5 nm)
Slope	5.8%
Curvature	48%

Table 3.2: Mask threshold parameters for estimating deposited Bi volume.

A number of Bi droplets can be clearly distinguished against the dark and mostly level background (substrate). To be able to quantify the amount of material deposited (and thus estimate the flux), the AFM image should be used to estimate the volume of the deposited Bi droplets. To this end, the image was further processed by applying a threshold mask (using Gwyddion software) to properly isolate the Bi droplets. The parameters of the mask (height, slope, and curvature) were chosen so as to make the mask fully capture the Bi droplets in the image, as shown in Figure 3.1. The mask parameters are shown in table 3.2.

Using this mask, the zero-basis volume was calculated. This volume is defined as the volume encompassing the surface of the droplet till the $z = 0$ plane, with subzero values constituting negative volumes in the calculation. The total volume of all the droplets and thus Bi was calculated to be 9.453 $\times 10^{-21}$ m^3. The effective Bi thickness deposited (assuming Bi covers the whole surface and not as droplets) can be calculated by dividing this volume by the surface area of the scan 1×1 μm^2, which yields an effective thickness of 9.453 nm (Vol_{Bi}). Knowing this, and the atomic weight of Bi, as well as the density and duration of deposition (4 minutes), it is possible to calculate the number of atoms deposited per unit area per unit time, which is essentially the flux. Given that the atomic mass of Bi AM_{Bi} = 209, the density of Bi (ρ_{Bi} = 9.78 $^{g}/_{cm^3}$), and that one mole of a substance (atomic mass in grams) contains 6.022 $\times 10^{23}$ (Avagadro's numer = N_A) atoms, the number of atoms deposited and thus the flux

can be calculated.

$$\text{Bi atom weight}(AW_{Bi}) = \frac{209\ g}{N_A} = 3.47 \times 10^{-22}\ g \cdot \mu m^{-2} \tag{3.1.1}$$

$$\text{Weight of deposited Bi overall} = WD_{Bi} = \rho_{Bi} \times Vol_{Bi} = 92.45 \times 10^{-15}\ g \cdot \mu m^{-2} \tag{3.1.2}$$

$$\text{Number of Bi atoms}(N_{Bi}) = \frac{WD_{Bi}}{AW_{Bi}} = 26.6 \times 10^{7}\ \approx 27 \times 10^{7} atoms \tag{3.1.3}$$

$$\text{Flux at 750 °C } (F_{750°C}) = \frac{N_{Bi}}{Area \cdot Time} = \frac{26.6 \times 10^{7}}{10^{-8} \times 240} = \mathbf{1.11 \times 10^{14}} \approx \mathbf{10^{14} \frac{atoms}{cm^2 \cdot s}} \tag{3.1.4}$$

The calculated flux for this data-point (Temperature = 750 °C) is 1.11×10^{14} $^{atoms}/_{cm^2 \cdot s}$. Using this data-point in conjunction with the previous flux measured by the ion gauge at 750 °C, the true flux vs. temperature curve can be obtained.

$$\text{Calibration factor} = \frac{F_{750\ °C}}{3.23 \times 10^{-7}} = \mathbf{3.44 \times 10^{20} \frac{atoms}{cm^2 \cdot s \cdot Torr}} \tag{3.1.5}$$

Multiplying the ion gauge flux readings in Table 3.1 by the calibration factor yields the calibrated flux vs. temperature curve, which can then be used to accurately select the correct temperature to apply to the Bi cell to obtain a given flux.

Plotting the final data after using the factor to calibrate the curve, and then

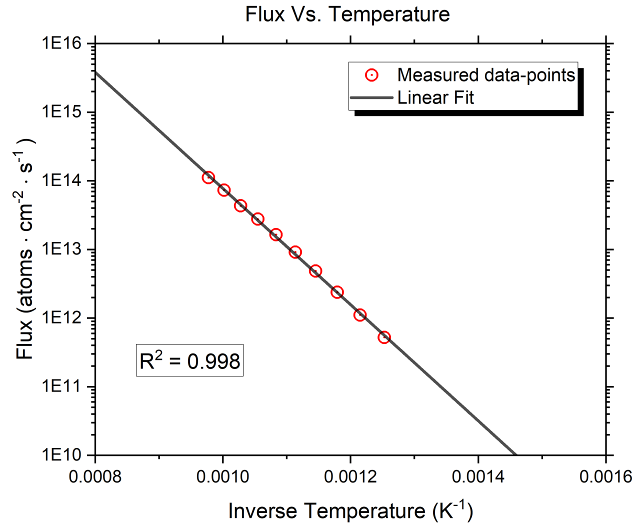

Figure 3.2: Arrhenius plot of the flux from the Bi cell vs. the applied temperature after calibration.

applying a linear fit for extrapolation, a clear Arrhenius relationship is observed in Figure 3.2 when plotting the flux on a log scale vs. the inverse of the temperature, as expected. The final fitted Arrhenius equation was found to be

$$f(1/T) = 2.25 \times 10^{22} \cdot e^{\frac{-2.67 \times 10^{-19}}{k_B T}} \tag{3.1.6}$$

3.2 GaAs(111)A homoepitaxy

To establish the state of GaAs(111) homoepitaxy without surfactants, a GaAs buffer layer was grown on GaAs(111)A. Before presenting the parameters of the growth, it is important to describe the sample preparation and loading procedure used for all samples grown in this chapter. The substrates used were 2-inch diameter, undoped, epi-ready, 350 μm thick wafers manufactured by AXT[84]. Firstly, the 2-inch wafers

were cleaved into sixths ("pie" pieces) in order to accommodate the custom holder designed for the MBE system, so as not to waste full wafers during growth. This was done by placing the full wafer on a custom designed steel cleaving platform connected to a pump to lock wafers in place during cleaving. The wafer was lined up and locked in place on the platform, and a small scratch was made using a diamond scribe, 30° from the line at the centre of and perpendicular to the primary flat (the cleavage lines for this orientation) as shown in Figure 3.3. The wafer edge where the scratch was made was then placed on an Allen key, and light pressure was applied till the wafer was cleaved. This process was repeated to obtain the 6 "pie" pieces. The samples were then cleaned using N_2. Subsequently, samples were then moved to a load-lock in preparation for MBE growth, which was evacuated of air first using a mechanical roughening pump, and then a turbo molecular pump to reach the required vacuum level (5×10^{-6} Torr). Inside the pre-growth load-lock chamber, a 15 minute outgassing procedure at 300 °C was done to remove and desorb any unwanted contaminants and particles (e.g. H_2O). The samples were then transferred using a transfer trolley to the growth chamber for deposition (after opening the gate valve between them) at a very high vacuum (VHV) value of 10^{-8} Torr.

After the sample was loaded in the growth chamber, the growth began. The temperature of the substrate was measured and tracked by way of a pyrometer capturing the blackbody radiation of the heated sample. As the temperature was ramped up in preparation for the subsequent oxide removal and growth, the As flux was initiated at 350 °C to saturate the substrate. This step is necessary in order to avoid As evaporation when increasing the substrate temperature T_{sub} and thus Ga droplets forming as a result. An inductively coupled plasma (ICP) source was used to etch away the

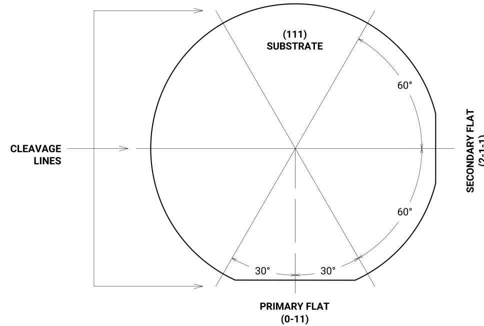

Figure 3.3: Cleaving lines for the (111) substrate.

oxide layer using H_2, then substrate is heated to 585 °C to help desorb the amorphous oxide layer formed on the substrate and to completely remove it. The use of the ICP source and H_2 plasma etching helps reduce the the T_{sub} needed for oxide removal and yields smoother surfaces. RHEED is observed to confirm oxide removal, as RHEED yields a uniform diffuse glow with the amorphous oxide intact, whereas after oxide removal, clear defined streaks were observed. After confirmation of the oxide removal, T_{sub} is ramped down to 485 °C to begin deposition. A Ga flux was deposited at a growth rate of $GR_{Ga} = 0.25$ $^{\mu m}/_{\text{hr}}$, with a V/III ratio of 9. The As source used was arsine AsH_3, which was passed through a cracker at (1000 °C) to dissociate it into As_2 dimers + H_2 which was then deposited on the surface. The GaAs buffer was grown for 36 minutes to yield a thickness of 150 nm. During this process substrate rotation was turned on in order to ensure the uniformity of the impinging flux and therefore the homogeneity of the growth.

AFM scans were conducted on the sample as shown in Figure 3.4. There is a conspicuous presence of large pyramidal dendritic defects and hillocks. The hillocks' height varied as shown between 9-12 nm as can be seen from the profiles in Figure

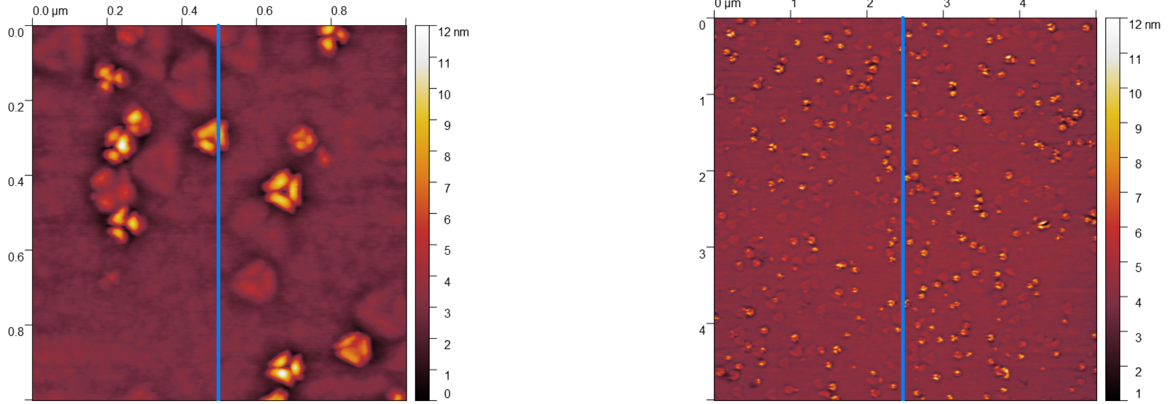

Figure 3.4: 1×1 μm^2 (left) and 5×5 μm^2 (right). AFM scans for the grown homoepitaxial GaAs(111)A buffer layer. Sample #2111

3.5, with bases on the order of 100 nm. The RMS roughness for the 1×1 μm^2 scan was 0.952 nm, while the RMS roughness for the 5×5 μm^2 scan was 0.612 nm. These characteristics mirror previous observations in the literature[54] and are characteristic of the presence of a large ES barrier, inhibiting downhill diffusion and thus 2D layer growth while permitting diffusion upwards to the nucleating island till it forms a 3D mound. Smaller flatter islands can be seen emerging, and assuming a large diffusion length for adatoms (larger than the island radius), the ES barrier must be the principal factor driving 3D growth[54]. These results unequivocally motivate the need for further studies on this surface with the goal of inducing more favourable surface morphologies for technological applications. This is what will be explored in the next section with Bi as a surfactant.

3.3 Bi-assisted growth on GaAs(111)A

Bi was used to investigate its effect on the GaAs(111)A surface morphology at differing Bi fluxes. Bi induced much smoother surfaces, lowering RMS roughness as the Bi flux

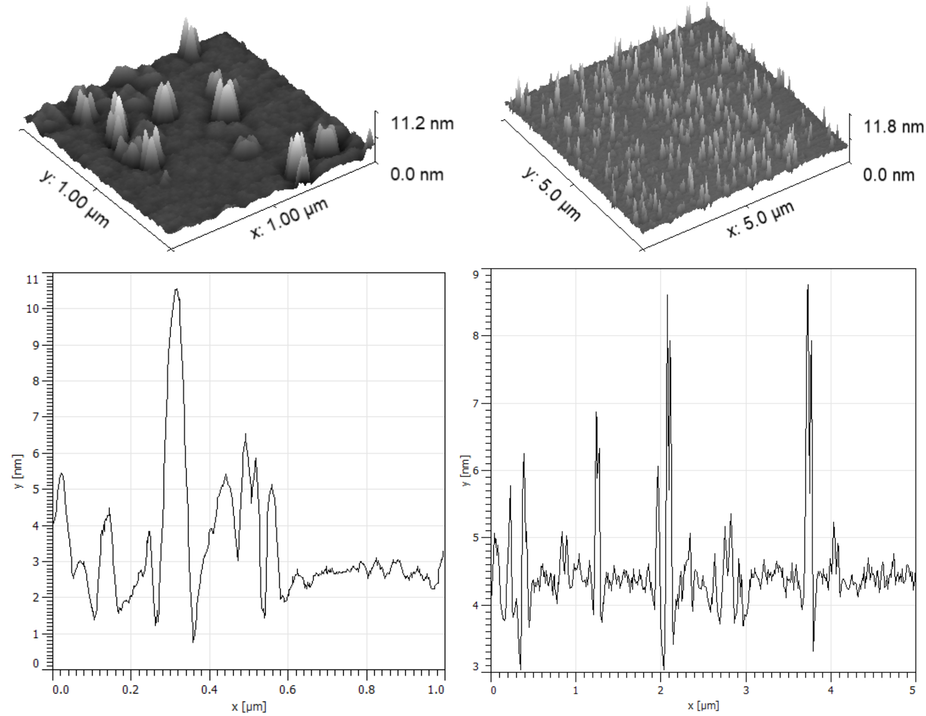

Figure 3.5: AFM scan of the homoepitaxial GaAs(111)A buffer layer. 1×1 μm^2 3D view of morphology (top left), 5×5 μm^2 3D view of morphology (top right), 1×1 μm^2 height profile at 0.25 μm vertically (bottom left, as indicated by the blue line in the previous figure), 5×5 μm^2 height profile at 2.5 μm vertically (bottom right, as indicated by the blue line in the previous figure).

increased, as well as inducing atomically-smooth steps. A summary of Bi's effect on GaAs(111)A on morphology and roughness is shown in Figure 3.6. In the upcoming subsections, each of the individual growths will be discussed in detail and analyzed.

3.3.1 First Bi-assisted growth ($T_{sub} = 365\ ^\circ$ C, $Flux_{Bi} = 0.28\ ^{ML}/_{s}$)

Building upon previous attempts to use Bi as a surfactant on low-index surfaces [63][62], Bi surfactant action was investigated on GaAs(111)A, which has not yet been studied extensively in the literature. Before investigating Bi's ability to induce epitaxial growth mode changes and InAs QD growth, it was important to explore what

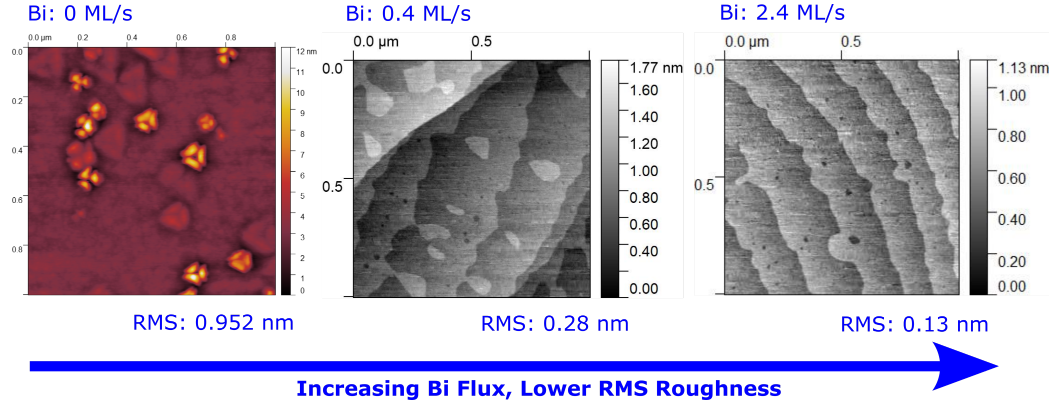

Figure 3.6: Summary of the effect of Bi on the GaAs(111)A surface, inducing smoother surfaces with increased Bi flux.

Bi does to the GaAs surface itself, motivating a study on homoepitaxial GaAs(111)A buffer growth with Bi.

Firstly, it is important to define what is meant by $^{ML}/_{s}$ as a unit of flux. The monolayer of a zincblende structure crystal is defined as $\frac{a_{crystal}}{2}$, where $a_{crystal}$ is the lattice constant of the crystal, assuming GaAs has two layers of Ga or As in the unit cell, with 4 atoms each. Therefore, each layer contains 4 Ga/As atoms. For a single layer (monolayer), there are 2 atoms, giving an areal density of $\frac{2}{{a_{crystal}}^2}$ for the typical (100) orientation, thus a flux of 1 $^{ML}/_{s}$ is equal to $\frac{2}{{a_{crystal}}^2}{}^{atoms}/_{cm^2 \cdot s^2}$. For GaAs this means

$$1\ ^{ML}/_{s} = \frac{2}{{a_{GaAs}}^2} = \frac{2}{(5.65 \times 10^{-10})^2} = 6.265 \times 10^{14} \approx 6 \times 10^{14} \frac{atoms}{cm^2 \cdot s^2} \tag{3.3.1}$$

$$0.28\ ^{ML}/_{s} = 0.28 \times 6.265 \times 10^{14} = \mathbf{1.8 \times 10^{14} \approx 3 \times 10^{14} \frac{atoms}{cm^2 \cdot s^2}} \tag{3.3.2}$$

Using these flux values with the calibration equation in Equation (3.1.6) and obtaining

the temperature value, the value of the temperature required to be applied to the Bi cell in order to obtain a flux of 0.28 $^{ML}/_{s}$ is found to be 1046 K (773 °C). For this first Bi-assisted growth a $Flux_{Bi}$ = 0.28 $^{ML}/_{s}$ was applied for 10 seconds pre-buffer layer growth, and this flux was maintained for the duration of the buffer layer growth (simultaneously with Ga and As).

For the first Bi-assisted growth ($Flux_{Bi}$ = 0.28 $^{ML}/_{s}$), the same sample preparation and loading procedures were used as outlined in the previous section in preparation for the growth. After loading, the outgassing procedure is completed and the oxide is removed thermally (confirmed by RHEED) as previously described, without the use of ICP to reduce H_2 in the system. T_{sub} was then ramped down to a lower temperature (365 °C) and GR_{Ga} = 0.25 $^{\mu m}/_{hr}$ and a V/III ratio of 10 were used.

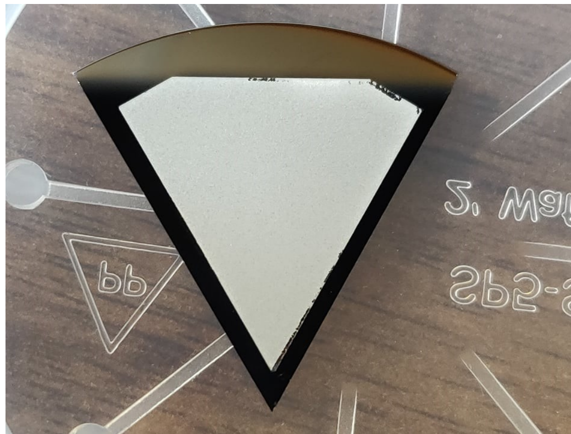

Figure 3.7: Bi-covered sample as a result of bulk condensation. Sample #2157.

Upon inspection of the sample after growth, it was clear that the sample was covered in Bi owing to the whitish colour of the sample (Figure 3.7), and that the growth of a smooth buffer layer growth had not transpired. This can be most likely attributed to either the low T_{sub} used (365 °C), causing the desorption of Bi to be in the bulk condensation regime, or a failure of the oxide to properly desorb. Considering

that a stable 2×2 RHEED reconstruction was observed before commencing the Bi deposition, the low T_{sub} during Bi deposition was the most plausible explanation. The low temperature inhibited Bi desorption (Bi adatoms did not possess enough thermal energy to overcome the desorption energy barrier) and thus lead to accumulation on the surface. Since Bi did not desorb after the growth, and in fact accumulated a considerably thick layer on the surface, it can be categorically concluded that Bi failed to act as a surfactant on this surface under these growth conditions.

To further buttress this conclusion, the sample was inspected using a Leica HC optical microscope with a Canon 77D 24 megapixel digital camera. Images were taken at 100× magnification (Figure 3.8). If the failed oxide removal hypothesis were accurate, a rough GaAs buffer layer would be expected upon observation under the microscope, while the presence of large droplets would dispel this notion. Bi droplets were clearly visible and further reified the accumulation hypothesis.

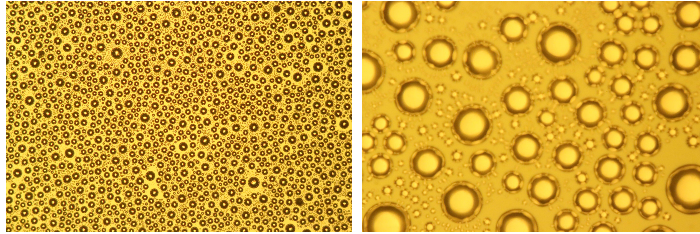

Figure 3.8: Bi-covered sample magnified 100 times (left) and 500 times (right) using an optical microscope.

3.3.2 Second Bi-assisted growth ($T_{sub} = 485$ °C, $Flux_{Bi} = 0.28$ $^{ML}/_{s}$)

For the second growth, the growth temperature (T_{sub}) was increased to 485 °C in order to allow for the timely desorption of Bi and hence facilitate surfactant action, and to prevent bulk condensation of Bi. The sample was prepared and loaded in a

similar manner to the growth described in the previous subsection, except that the Bi deposition and GaAs buffer growth procedures were done at 485 °C. AFM scans were then carried out on the sample.

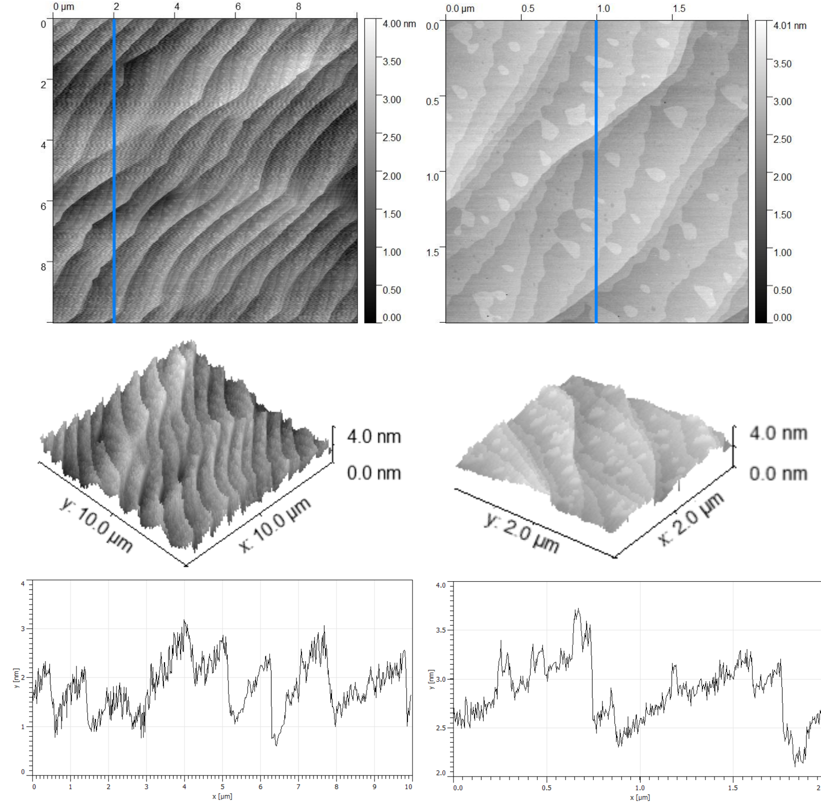

Figure 3.9: AFM scan of Bi-enhanced GaAs(111) buffer layer at Bi = 0.28 $^{ML}/_{s}$. 10×10 μm^2 AFM image (top left), 2 ×2 μm^2 AFM image (top right), 10×10 μm^2 3D view of the morphology (middle left), 2×2 μm^2 3D view of the morphology (middle right), 10×10μm^2 height profile at 2 μm vertically (bottom left, as indicated by the blue line), 2×2 μm^2 height profile at 1 μm vertically (bottom right, as indicated by the blue line). Sample # 2172.

It is apparent form Figures 3.9 and 3.10 that the Bi provoked a radically different surface morphology from the non-Bi buffer growths shown in Figure 3.4. An atomically-smooth surface was observed with atomic terraces and steps, which is a novel result compared to reports of GaAs(111) MBE buffer layer growth in the

literature[54]. RMS surface roughness for the (10×10), (2×2), (1×1) μm^2 scans in Figures 3.9 and 3.10 were measured to be 0.533, 0.28, 0.283 nm respectively. This surface indicates that step-flow growth has occurred on the surface despite the substrate being an on-axis substrate. This is most likely attributed to the fact that the propensity for adatoms to adsorb to step edges seems to be larger than the tendency to form islands, hence forming moving steps as the growth progresses. No substantial hillocks or defects can be found on the surface, a testament to its ultra-smooth nature, which is in sharp contrast to Figure 3.4. While there are a number of monolayer islands (on the order of hundreds of picometres high), it is evident that Bi modified surface energies and properties on the substrate, and desorbed post-growth. This is confirmed by the observation of (2×2) RHEED streaks after the growth, unlike for the growth in the previous subsection. These observations are distinctly characteristic of surfactant action. Observing the fact that terraces are forming, along with the prominence of several monolayer islands, it can be deduced that the growth is at the morphological transition threshold between island nucleation and step-flow growth. Knowing that the transition to the step-flow growth regime occurs when the terrace width is similar to the adatom diffusion length, it is reasonable to assume that the diffusion length on this surface is on the order of the terrace width (and at least greater), which can be deduced from Figures 3.9 and 3.10 to be in the 250-500 nm range. This observation is more or less in line or a little larger than the diffusion lengths quoted in the GaAs(111)A literature, where the diffusion length of Ga adatoms on the surface has been suggested to range from 100 nm to several hundred nanometres[85][86][87]. In light of this, a possible hypothesis behind Bi's triggering of step-flow growth is that Bi induced a slight increase of the diffusion length of the

impinging adatoms larger than the step width, allowing for adatoms to the reach step edges where the probability of sticking is larger (owing to an increase in nearest neighbours) thus provoking step-flow growth on a nominally on-axis substrate (±0.5° as per wafer specifications). Since steps appear on the surface, an offcut angle can be calculated. For this terrace width ($W_t \approx 250$ nm) the local offcut angle $\theta_{offcut} = 0.068$ is defined as the angle encompassing the monolayer (ML) height and adjacent to the step. It can be calculated using the following equation

$$\theta_{offcut} = arctan(\frac{ML}{W_t}) = arctan(\frac{2.825 \times 10^{-10}}{250 \times 10^{-9}}) = 0.068^{\circ} \qquad (3.3.3)$$

which is much larger than the width calculated for a 0.5° offcut, which using similar arguments can be calculated to be around 34 nm.

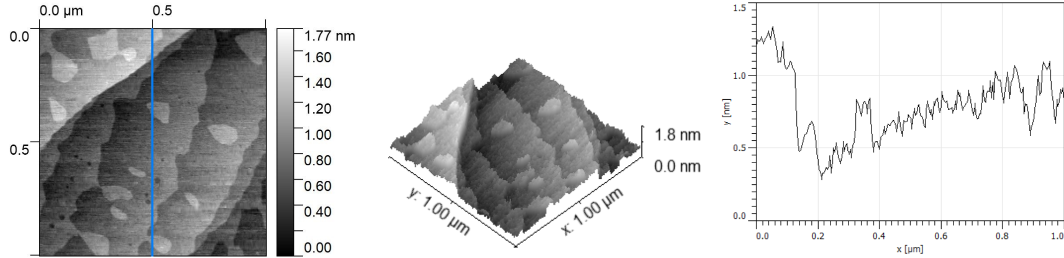

Figure 3.10: AFM scan of Bi-enhanced GaAs(111) buffer layer at Bi = 0.28 $^{ML}/_{s}$. 1×1 μm^2 AFM image (left), 1×1 μm^2 3D view of the morphology (middle), 1×1 μm^2 height profile at 0.5 μm vertically (right, as indicated by the blue line). Sample # 2172.

3.3.3 Third Bi-assisted growth ($T_{sub} = 485$ °C, $Flux_{Bi} = 1$ $^{ML}/_{s}$)

To further examine the effect of Bi on GaAs(111)A, another growth was carried out, identical to the one described in the previous subsection but with an increased Bi flux of (1 $^{ML}/_{s}$). The goal was to examine if an increased Bi flux could have a heightened

effect on surface morphology smoothness or atomic terraces, or cause any notable changes when compared to 0.28 $^{ML}/_{s}$. The calibration equation (3.1.6) was used to select the required temperature to be applied to the Bi cell in order to yield a flux of 1 $^{ML}/_{s}$, and a temperature of 1121 K is shown to be needed. After sample growth, the sample was imaged using AFM.

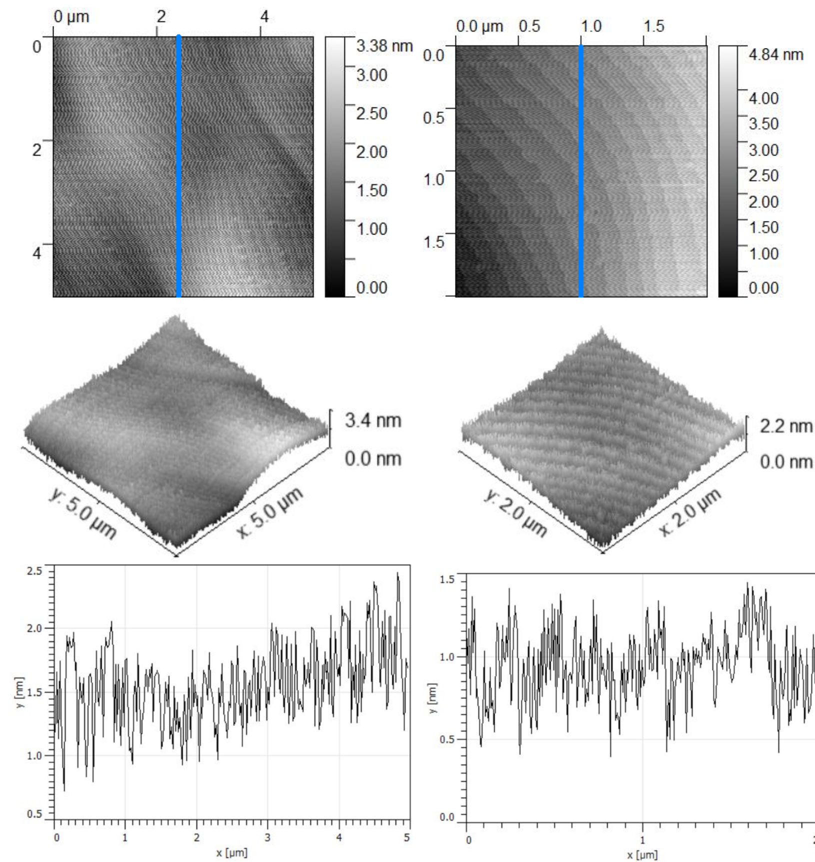

Figure 3.11: AFM scan of Bi-enhanced GaAs(111) buffer layer at Bi = 1 $^{ML}/_{s}$. 5×5 μm^2 AFM image (top left), 2 ×2 μm AFM image (top right), 5×5 μm^2 3D view of the morphology (middle left), 2×2 μm^2 3D view of the morphology (middle right), 5×5 μm^2 height profile at 2.5 μm vertically (bottom left, as indicated by the blue line), 2×2 μm^2 height profile at 1 μm vertically (bottom right, as indicated by the blue line). Sample # 2181.

As is evident from Figures 3.11 and 3.12, Bi was able to generate atomically-smooth terraces and provoked a smoothing of the surface morphology. The step-flow nature of the growth also transpired under the increased flux. RMS surface roughness for the (5×5), (2×2), (1×1) μm^2 scans in Figures 3.11 and 3.12 were measured to be 0.49, 0.8, 0.13 nm respectively. It can be noted that the smattering of monolayer islands present for the 0.28 $^{ML}/_{s}$ growth was absent in this growth, further enhancing the atomically-smooth surface. Intriguingly, there was an apparent presence of holes in the terraces for this growth. This could possibly be attributed to the significantly increased Bi flux, raising the competition of the As and Bi group V species to bond with the Ga-terminated surface, especially at modest V/III ratios compared to the literature[54]. Bi could have incorporated instead of As in the surface bilayer, desorbing when the Bi flux was interrupted and thus leaving holes behind. From the 3D image in Figure 3.11 it seems there was a local offcut for this particular scan location, which may have influenced the step-flow growth, varying the terrace width The offcut angle for this sample is slightly larger than that of the one in the previous section owing to the slightly shorter terrace width.

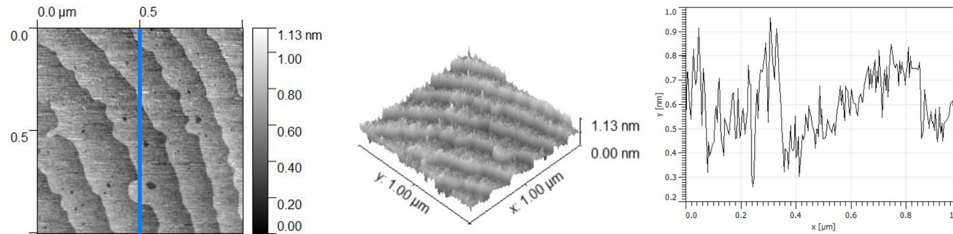

Figure 3.12: AFM scan of Bi-enhanced GaAs(111) buffer layer at Bi = 1 $^{ML}/_{s}$. $1{\times}1$ μm^2 AFM image (left), $1{\times}1\mu m^2$ 3D view of the morphology (middle), $1{\times}1\mu m^2$ height profile at 0.5 μm vertically (right, as indicated by the blue line). Images processed using Gwyddion. Sample # 2181.

Another compelling and technologically relevant observation was the tendency of

the high Bi flux to induce more evenly-spaced atomic steps when compared to the previous 0.28 $^{ML}/_{s}$ Bi growth, as evidenced by a comparison between Figure 3.9 and Figure 3.12. Offcut surfaces with large ES barriers (such as some (111) surfaces) have been shown to support step-bunching due to the anisotropy in diffusion kinetics imposed by the barrier[88][89]. Interestingly, the ES barrier, which has been posited to be the root of the roughening and hillock formation problem in GaAs(111) homoepitaxial growth[54] could be provoking atomic step equalization. The ES barrier inhibits adatom diffusion across step edges. While it has been suggested that the mounds forming on GaAs(111)A homoepitaxial layers are fueled by the large ES barrier only allowing diffusion of adatoms uphill or to climb the steps, creating a net upward diffusion of adatoms and thus driving 3D growth, this did not seem to be occurring here. In this instance, the ES barrier could be having an opposite effect in the context of step-flow growth. It is intriguing to note here that the terrace width has somewhat shrunk compared to the previous growth, making it difficult to judge if the diffusion length has changed with the increased Bi flux, as the most that can be said in this case is that the diffusion length is unambiguously bigger than the $\approx$ 200 nm step widths shown in Figure 3.12. In any case, it is evident that the adatoms are free to diffuse the full width of the terraces (whether it be due to width reduction or diffusion length increase), ensuring that the ES barrier considerations heavily influence the dynamics as the adatoms reach both extremes of the terrace with ease. This facilitates the incorporation of adatoms to the “uphill” atomic step edges but hinders binding to step edges in lower terraces, or “downhill” ones, again due to the ES barrier’s inhibition of adatoms “falling off” higher terraces or islands. When adatoms can attach to uphill steps and are prohibited from diffusion downhill

to attach to downhill steps, large terraces get shorter as adatoms on it cannot diffuse down to contribute to its length, and the large terrace is eventually covered by adatoms attaching to the uphill step edge (shortening the long terrace), hence the occurrence of step anti-bunching (step-width equalization).

As in Figure 3.13, the adatoms in the long middle terrace attach to the edge of the left terrace (uphill), while (downhill) diffusion to the step edge between the middle and right terraces is discouraged due to the unfavourable energetics imposed by the ES barrier. Assuming an uneven starting surface without an ES barrier and with unequal monolayer steps, and a uniform growth rate as a result of a uniform flux of impinging atoms across the entire surface, the growth would evolve in a manner which conserves this unequal step imbalance with no tendency for equalization. Larger steps would receive more atoms, which would stick there, while smaller steps would receive less atoms. This is known as step-bunching. If there were an ES barrier at the step edges acting as described previously (unidirectional upward diffusion), bunching would also occur, with the status-quo maintained and the unequal step widths would remain throughout the growth as adatoms can climb up the steps. Considering the presence of a "modified" large positive ES barrier inhibiting both adatoms climbing the steps and adatoms falling off them though alters the dynamics and energetics of the growth, by driving binding to uphill step edges as in this case the barrier does not allow downhill adatoms to climb to the uphill steps. Therefore large terraces become smaller as atoms attach to step edges and cover them. This phenomenon is known as step anti-bunching and is a desirable for the growth of quality semiconductor heterostructures and uniform surfaces. Again, it is important to recall that in the conventional non-surfactant growth dominated by 3D hillocks (Figure 3.4), the ES

barrier allowed diffusion of the adatoms to climb to the higher island but not for the adatoms on the island to diffuse downhill. This did not occur here, as adatoms reaching the step edge seem to be locked in place with no propensity for fuelling 3D growth. This seems to intimate that Bi plays a role in strengthening the bond between step edges and adatoms, with adatoms preferring to incorporate there than diffuse upwards. It is possible that Bi itself could be incorporating there during growth, locking adatoms onto the same level as they float above them and hampering their climb up the steps, before desorbing.

After investigating various Bi fluxes on GaAs(111)A, it has been proven that the aforementioned surfactant-induced, atomically-smooth terrace morphology would drastically improve quantum nanostructure and device properties on GaAs(111), and open up this previously underutilised platform to a vast array of technological applications in quantum photonics, GaAs high-speed electronics, spintronics, and topological insulators. These results verify and expand upon the preliminary work[65] on GaAs(111)A.

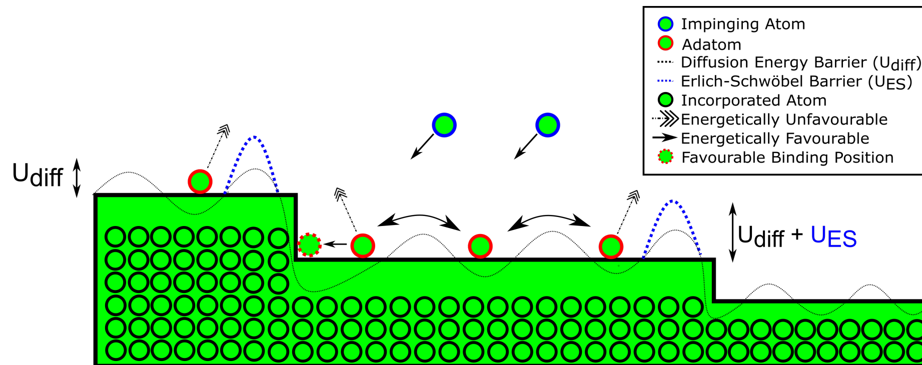

Figure 3.13: Demonstration of the surface energetics relevant to adatom diffusion leading to step-flow growth. There is a clear driving force for step-antibunching owing to the ES barrier.

3.4 Bi Desorption RHEED experiment

3.4.1 Motivation

In the interest of further probing into the nature of Bi surfactant action, knowing how Bi adatoms behave on the GaAs(111) surface is of paramount importance. To that end, unveiling the shroud of mystery surrounding the energetic and kinetic landscape of this surface it crucial. The nature and value of the diffusion and desorption energy barriers strongly dictate many facets of Bi adatom dynamics, such as the Bi coverage at any given growth condition (temperature, flux ec.), Bi diffusion length or diffusivity on the surface, and tendency for incorporation on the surface, among others. An important parameter which has not yet been reported in the literature for this system (Bi:GaAs(111)) is the desorption energy barrier U_{Des}. The value of this parameter is important in the context of the layer growth models described in Chapter 2, particularly the BET model owing to the fact it is a multilayer model. Knowing the value of U_{Des} in light of the value of the energy desorption barrier for Bi on Bi ($U_{Des_{Bi:Bi}} = 1.7$ eV)[90] would allow for the deduction of how easily bulk Bi layer formation can occur on GaAs(111) surfaces. If $U_{Des_{Bi:Bi}} < U_{Des}$, this implies that Bi sticks to GaAs(111) more strongly than to other Bi atoms, meaning as the GaAs(111) surface is bombarded with Bi and a Bi monolayer is formed, it will be harder to form the bulk phase (several monolayers), with such a buildup only being possible under increased fluxes as per the BET model. This would mean increased Bi fluxes could be used to increase the surfactant effect without fear of bulk condensation. Hence, the calculation of this parameter could provide significant insight into how Bi wets the surface and how Bi layers form, further enhancing the understanding

of its surfactant behaviour.

3.4.2 Experiment Methodology & Setup

There are two methods to fit RHEED data to extract U_{Des}, as outlined in a study by Young et al.[90]. Firstly, the RHEED intensity data can be used to model Bi coverage, and thus can be fit with Langmuir isotherm model to measure U_{Des}.

Assuming single monolayer formation, with no multiple adsorption, mutual adatom interactions, diffusion, and adsorption to empty sites only (no bulk condensation), the Langmuir adsorption isotherm can be invoked to model Bi monolayer formation and coverage on this surface.

$$\frac{\mathrm{d}\theta}{\mathrm{d}t} = (\frac{(1-\theta)z}{N_s}) - \theta\nu \mathrm{e}^{\frac{-U_{Des}}{k_B T}} \tag{3.4.1}$$

where

$$z = \frac{P}{\sqrt{2\pi m k_B T}} \tag{3.4.2}$$

where θ is the Bi coverage (ranging from 0 to 1), ν is the vibrational attempt frequency of Bi adatoms (Hz), and z is the Bi flux ($^{atoms}/_{cm^2 \cdot s^2}$) as outlined in chapter 2. Solving for the steady state solution implies zero change in Bi coverage. Setting $\frac{\mathrm{d}\theta}{\mathrm{d}t} = 0$ yields

$$\theta = \frac{z}{z + \nu N_s \mathrm{e}^{\frac{-U_{Des}}{k_B T}}} \tag{3.4.3}$$

$$\theta = \frac{QP}{1+QP} \tag{3.4.4}$$

where

$$Q = \frac{e^{\frac{U_{Des}}{k_B T}}}{\nu N_s \sqrt{2\pi m k_B T}} \tag{3.4.5}$$

Knowing the Bi coverage (θ) at different temperatures when depositing Bi on GaAs(111), the θ vs. T data-points can be used to fit the Langmuir model curve to solve for U_{Des}. Comparing the RHEED streak intensity can be used as a measure of θ[90], allowing the aforementioned curve-fitting and U_{Des} parameter extraction. The rise in RHEED intensity could be attributed to the heavier Bi atoms (when compared to Ga), with more electrons, causing more electron reflection/scattering for the RHEED and thus more electrons to hit the fluorescent surface.

Another method (and the one used in this thesis) to calculate U_{Des} experimentally is to measure the desorption time of Bi at different temperatures and plotting the Arrhenius relationship between the two, and subsequently calculating the slope as a measure of U_{Des}.

$$\frac{1}{\tau_{Des}} = \nu \cdot e^{\frac{-U_{Des}}{k_B T}} \tag{3.4.6}$$

Taking the natural logarithm of both sides

$$\ln\left(\frac{1}{\tau_{Des}}\right) = \ln\left(\nu \cdot e^{\frac{-U_{Des}}{k_B T}}\right) \tag{3.4.7}$$

$$\ln\left(\frac{1}{\tau_{Des}}\right) = \ln(\nu) + \left(\frac{-U_{Des}}{k_B}\right) \cdot \left(\frac{1}{T}\right) \tag{3.4.8}$$

where τ_{Des} (s) is the residence time. Looking at equation (3.4.8), measuring the τ_{Des}

at several different temperatures, and plotting an Arrhenius plot $\ln\left({}^{1}/_{\tau_{Des}}\right)$ vs. $\left({}^{1}/_{T}\right)$ would yield a slope of ${}^{-U_{Des}}/_{k_B}$, allowing the extraction of U_{Des}, as k_B is a constant. The y-intercept can be used to extract the attempt frequency ν.

To this end, the samples (GaAs(111)A) for this experiment were prepared and loaded into the chamber using the same method as described previously in this chapter, with $GR_{Ga} = 0.25$ ${}^{\mu m}/_{hr}$ and V/III ratio = 10. A 0.28 ${}^{ML}/_{s}$ Bi flux was used 10 seconds before buffer growth and was left on for the remainder of the buffer growth, A GaAs buffer was grown for 36 minutes for a buffer layer of 150 nm at $T_{sub} = 485$ °C. The RHEED is checked to ensure Bi is not covering the substrate and that Bi is desorbing. After buffer layer growth is completed, both Bi and Ga sources are switched off (while maintaining As to prevent As desorption). Substrate rotation is then turned off, and the Bi shutter is opened (Bi deposition is resumed) for 60 seconds at 0.28 ${}^{ML}/_{s}$. After this, the Bi shutter is then closed and the RHEED is observed as the Bi deposition is interrupted/shut off. The RHEED transition and change upon halting Bi deposition is captured using a Nikon D5300 digital camera. A black shroud was used to cover the camera and RHEED screen together to minimize reflections, with the camera being mounted on a tripod. The captured RHEED video was processed in order to analyze the RHEED change, and calculate τ_{Des} by observing how quickly the reconstruction changes as a measure of the speed of Bi desorption, and therefore the residence time, as illustrated in Figure 3.14.

RHEED videos were recorded for the Bi ON/OFF transition (implying Bi desorption), sliced into individual frames, and then analyzed using ImageJ[91]. The brightness/intensity of both the central RHEED streak and the (re)appearing RHEED streak was recorded for each measurement and plotted vs. time in order to track

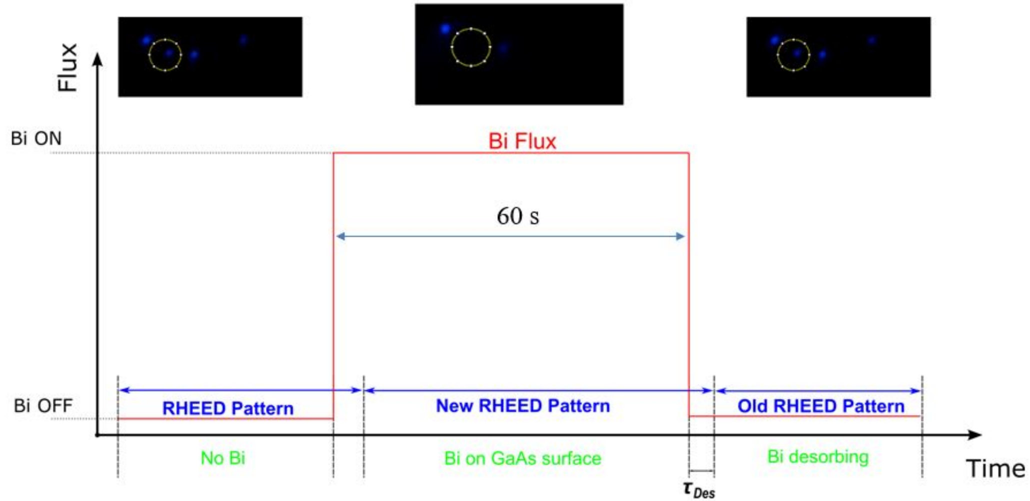

Figure 3.14: Demonstration of how τ_{Des} is observed from the experiment (depositing Bi, allowing it to desorb, and observing RHEED changes).

changes, as shown in Figure 3.15. The time taken for the RHEED central streak to change from one stable intensity to another, or the time for a new streak to appear was measured in order to estimate τ_{Des}. These changes imply a reconstruction change and/or an alteration of the surface (most likely Bi desorption), meaning they are likely representative of τ_{Des}. The reappearing RHEED streak when Bi desorbs (RHEED pattern change) is circled and the intensity is tracked. The videos were processed using ImageJ. The video was taken at T_{sub} = 485 °C.

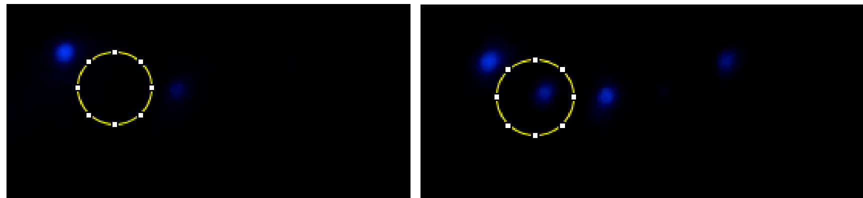

Figure 3.15: RHEED pattern (1×1) as Bi is being deposited (left) and RHEED pattern (2×2) after 60 seconds when Bi deposition is halted and Bi desorbs (right).

3.4.3 Experiment Results

First Attempt

The experiment was carried out at at several temperatures, with 3 readings of the reappearing RHEED streak intensity vs. time for each temperature, with the most stable reading (from each temperature) selected to plot and analyze. A wide range of temperatures ($T_{Sub} = 440, 470, 485, 500$ °C) was used to survey τ_{Des} at different energetic conditions.

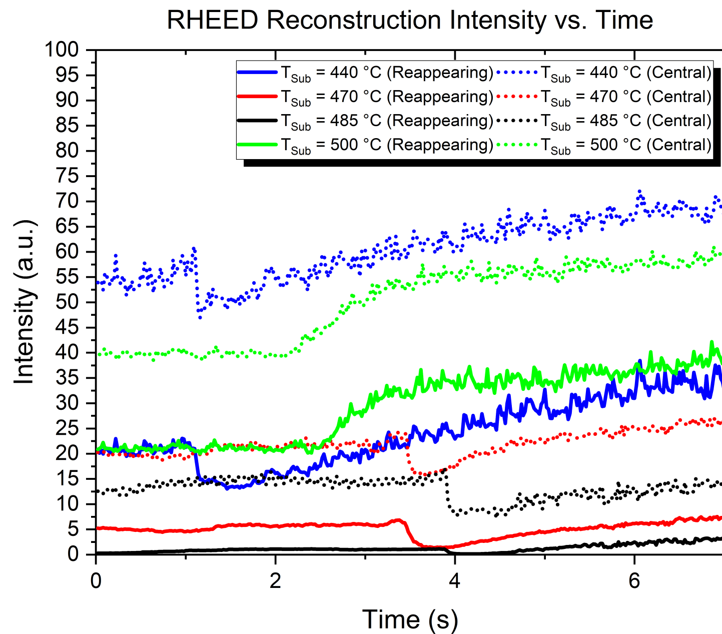

Figure 3.16: Intensity rises vs. time for both the reappearing RHEED streak and the central one.

Observing the RHEED video before, during and after Bi deposition (for all temperatures), it was clear that no bulk Bi build up (metallic Bi droplets) were forming

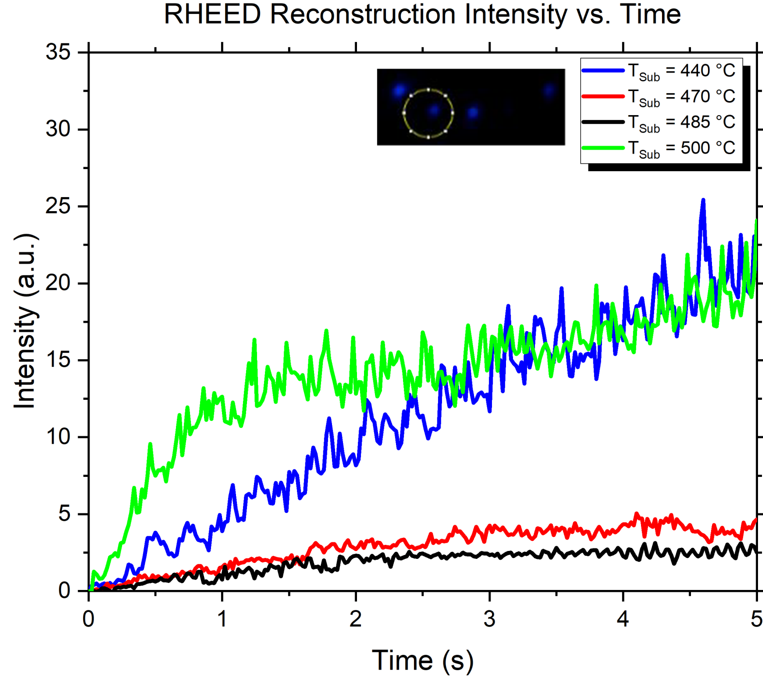

Figure 3.17: Intensity rises vs. time for the reappearing RHEED streak (2×2). Rise times for the intensities are an indication of τ_{Des} (inset is the plotted $2 \times 2 streak$).

on the surface. This can be deduced from the fact that that a stable 2×2 reconstruction was seen pre-deposition, which transitioned into a 1×1 deposition during deposition, then returned to 2×2 after shutting of the Bi source (see Figure 3.15). It would stand to reason that if Bi bulk had formed, there would not be a constant RHEED pattern observed during deposition. The usage of a steep RHEED grazing angle could be behind the spotty streaks, as the electron beams penetrate deeper into the surface several monolayers.

It can be seen from Figures 3.17 and 3.16 that for higher T_{Sub} values, the intensity shoots up quicker and rises in less time. It is important to note that the plotted intensity vs. time data are for the reappearing RHEED streak as shown in Figure 3.15.

The rise times for both the central and reappearing RHEED streak are very similar. However, the reappearing RHEED streak was chosen as opposed to the central one as this is likely more representative of the desorption of Bi than the intensity fluctuation of the ever-present central RHEED streak. Some of the higher temperature rise times (e.g. $T_{Sub} = 485$ °C) may seem to have low rise times at first glance, but this can be attributed to the low steady-state intensity for these temperatures.

The start of the decay in each curve in figure 3.16 represents the moment when the Bi was turned off, allowing for the intensity rise as Bi desorbs from the surface. These decays were representative of a change in the background intensity for the whole RHEED screen, and did not change substantially with T_{Sub}, indicating that they do not hold useful information for surface dynamics. It is interesting to note how for some temperatures this initial pre-rise decay exists, while it is absent for others. The representative part of the signal (rise) is taken starting from the local minimum (after the background intensity change from shutting Bi off) till the end of the signal. The plots in Figure 3.17 are taken from Figure 3.16, but with the rises shifted to time = 0, and the starting intensity for the rise set to 0.

Calculating the rise times (an estimate of τ_{Des}) involves measuring the time from time = 0 till the time the intensity levels-off and becomes stable. Rather than measure this time arbitrarily, an exponential rise model for the rise times is used to fit the data, and to subsequently extract (τ_{Des}). The fitting equation for the RHEED intensity $I(t)$ (arbitrary units) was defined as

$$I(t) = I_{Max}(1 - e^{-(t-x)/\tau_{Des}}) \tag{3.4.9}$$

where I_{Max} is the maximum RHEED intensity reached (steady-state), and (x) is

a shifting term in order to align the rise model with the data.

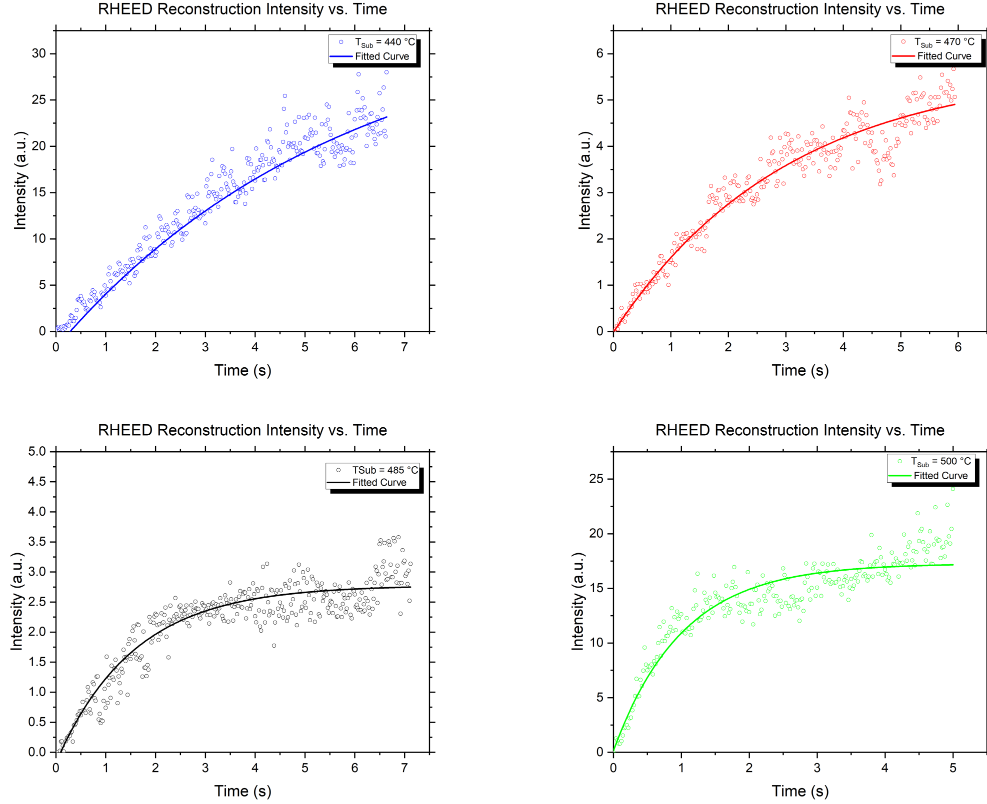

Figure 3.18: Reappearing RHEED streak intensity data fitted with exponential equation in order to extract τ_{Des}.

It can be seen from Figure 3.18 that the exponential rise time model fits the data very well, follows the expected coverage, and can yield an accurate estimate of τ_{Des}. The R^2 parameter signifying goodness of fit for T_{Sub} = 440 °C, 470 °C, 485 °C, 500 °C was 0.9986, 0.9338, 0.8815, 0.8653 respectively. The extracted τ_{Des} rise time values from the fitted curves are presented in Table 3.3. It is evident from the table that, as expected, higher T_{Sub} values yielded lower τ_{Des} values.

Plotting the rise times on an Arrhenius plot of desorption rate vs. inverse temperature ($ln(^1/_{\tau_{Des}})$ vs. $^1/_T$) yields U_{Des} from the slope ($^{-U_{Des}}/_{k_b}$)) and the attempt

T_{Sub} (° C)	τ_{Des} (s)
440	5.8±0.2
470	3±0.4
485	1.55±0.14
500	1±0.1

Table 3.3: τ_{Des} values from fitting.

Parameter	Result
U_{Des}	1.4 ± 0.7 eV
ν	0.14×10^{10} Hz [2.2×10^{5} - 7.8×10^{13}]

Table 3.4: U_{Des} and ν values from fitting for second experiment with uncertainties.

frequency (ν) from the y-intercept. The fitting polynomial (y = mx +c) , where m is the slope and c is the y intercept, was found to be

$$ln(1/\tau_{Des}) = -16333x + 21.064 \tag{3.4.10}$$

$$c = ln(\nu),\ \nu = 0.14 \times 10^{10}\ Hz \tag{3.4.11}$$

$$m = {-U_{Des}}/{k_b} = -16333,\ U_{Des} = -2.254 \times 10^{-19} J = \mathbf{1.407\ eV} \tag{3.4.12}$$

U_{Des} was calculated to be 1.407 eV, and $\nu = 0.14 \times 10^{10}$ Hz as shown in Figure 3.19.

Therefore, when considering the error analysis for the fit, this first RHEED experiment produced U_{Des} 1.4 ± 0.7 eV while taking into account the confidence interval (95% bounds). The results are summarized in table 3.5

While the experiment was successful in yielding a realistic value for U_{Des}, there

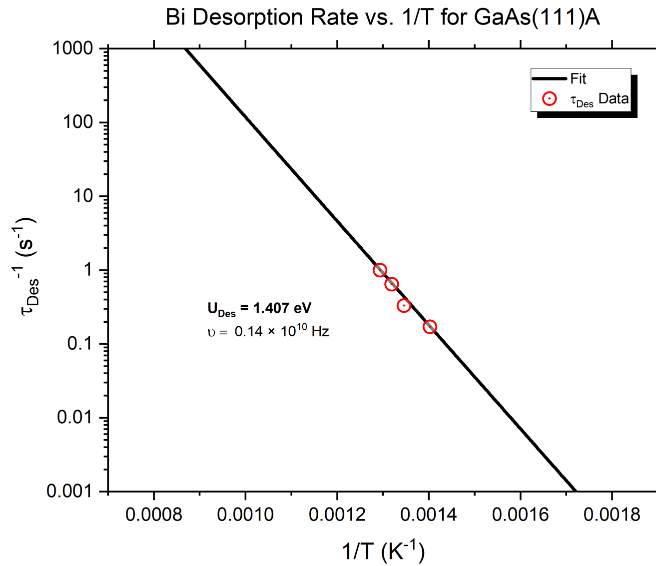

Figure 3.19: Arrhenius plot (desorption rate vs. inverse temperature). $R^2 = 0.9735$.

were a few issues that could potentially be problematic regarding the data from this first experiment. The first issue is the noisy nature of the data. Another potential issue was that the rise times were only recorded for as little as 5 seconds after the start of the rise. This could mean that the rise times were cut off prematurely in the recording and could affect the calculation of rise times. These concerns are allayed by the use of a fitting equation to extract τ_{Des}. Higher temperatures could also have been used. The ±0.7 eV error for the final energy barrier value is also more than desired. Nevertheless, these concerns, along with a desire to ensure replication and reproducablity of the result, led to a second attempt at the experiment, with longer recording of rise times and using different T_{Sub} values.

Second Attempt

The experiment was conducted again with an identical setup and methodology in an attempt to reproduce the results. In order to mitigate the issues brought up in the previous experiment, the rise times were recorded for over 20 seconds in order to capture the full rise, and a more diverse range of T_{Sub} data-points were taken (400, 425, 485, 515, 530) °C, focusing on higher temperatures.

Similar RHEED patterns were observed for this experiment as in the previous one. The RHEED intensities from the reappearing RHEED streak were plotted versus time in Figure 3.20. As can be seen from the figure, the RHEED intensity signals for this experiment suffer from even greater noise than the first one, which hampered data extraction (rise times). The noisy nature of the signal, with large fluctuations, could be due to electric current fluctuations in the substrate heater's coil, due to the proportional–integral–derivative (PID) controller. In an attempt to maintain a stable heating temperature, the heating coil could have been turning on and off to fixate on the required temperature. The resulting varying electromagnetic fields from the current changing in the coil could be interfering with the electron beams responsible for the RHEED patterns, yielding noisy data and intensity fluctuations on a large scale. This hypothesis is buttressed by the fact that readings for $T_{Sub} = 485$ °C rise time appears to be much more stable. Before conducting the experiment, the buffer layer was grown at this temperature for 36 minutes, meaning that the temperature was likely very stable compared to the other measurements. There were numerous sudden rises and kinks in the signals, particularly for lower temperatures. The fact that the $T_{Sub} = 485$ °C signal is the most stable, and was the first temperature used in this experiment after the growth of the buffer layer, further lends credence to

the thermal instability hypothesis as a source for the noisy RHEED signals, owing to the electromagnetic interference from the coil in the substrate heater. It can be seen that for higher temperatures, an initial quick rise exists, followed by a slower and more gradual rise. This is very apparent in the more stable signals, such as for (T_{Sub} = 485 °C). For lower temperatures one rise exists, which could be a result of a merging of the two rises. These two rises could be a manifestation of 2 different phenomena occurring on the surface. It is important to note however that when analysing the RHEED signals, the second gradual rise times exhibited no substantial variation with temperature, while the initial quick rises did. The second "gradual" rises are also more prone to being corrupted by fluctuations owing to their increased length. As a result, the signals for lower temperatures are severely adversely affected by the noise and sudden intensity fluctuations, to the point where they are rendered largely useless (cannot be reliably fitted with the rise time exponential model). In addition, the merging of the two rises for the colder temperatures would also not allow for reliable comparison with higher temperatures, as these times might be resultant of different physical phenomena. For these reasons, T_{Sub} = 400 and 425 °C) were discarded from further analysis.

For T_{Sub} = 485 and 515, and 530 °C, the RHEED signals were shifted to time = 0, and the starting intensity for the rise were also set to 0. from the start of the rise as in the previous experiment (Figure 3.21). The rise times plotted were the initial quicker rise times as opposed to the gradual ones. The higher temperatures exhibit quicker rise times as expected.

The same fitting equation (3.4.9) was used for this experiment. The fits are shown in Figure 3.22 and the extracted rise times τ_{Des} are shown in Table 3.5.

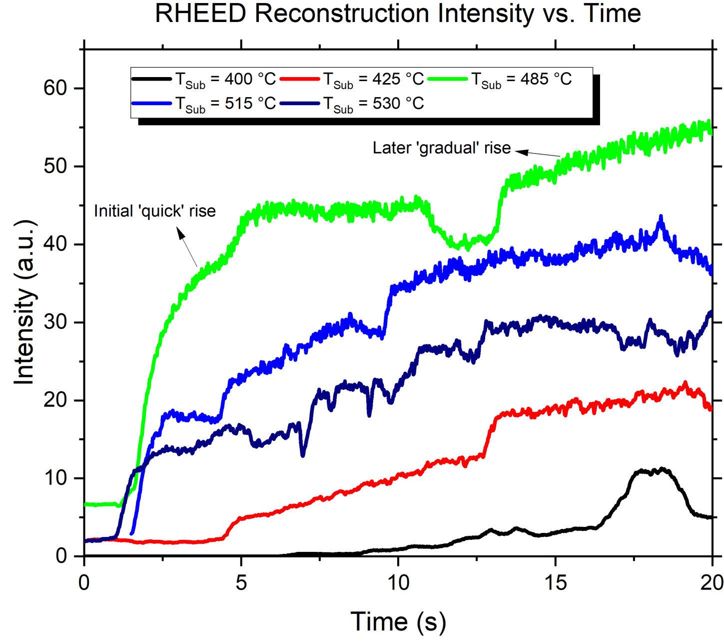

Figure 3.20: Reappearing (2 × 2) RHEED streak intensity plotted versus time. Quick and gradual rises are outlined.

The desorption times are plotted on an Arrhenius plot and a linear fit is applied to calculate U_{Des} as shown in Figure 3.23. The fitted line equation (y = mx + c) was calculated to be

$$ln(^1/_{\tau_{Des}}) = -15836x + 20.996 \quad (3.4.13)$$

T_{Sub} (° C)	τ_{Des} (s)
485	0.85±0.04
515	0.48±0.04
530	0.25±0.02

Table 3.5: τ_{Des} values from fitting for second experiment.

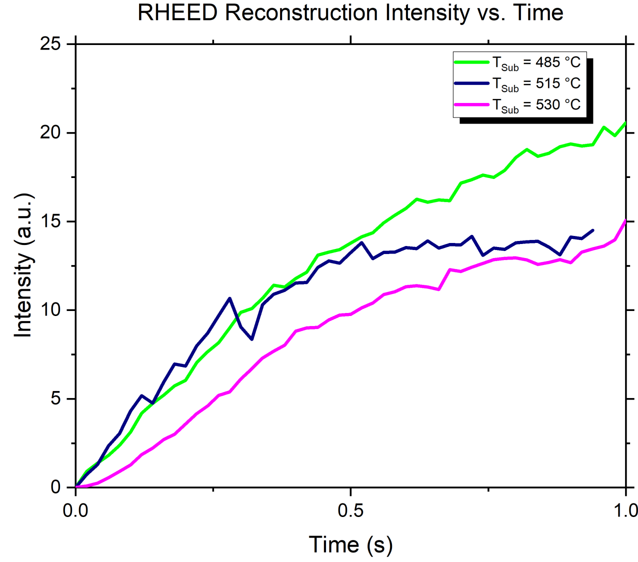

Figure 3.21: Intensity rises vs. time for the reappearing RHEED streak as an estimate of τ_{Des}.

$$c = ln(\nu),\ \nu = 0.11 \times 10^{10}\ Hz \tag{3.4.14}$$

$$m = {}^{-U_{Des}}/_{k_b} = -15836,\ U_{Des} = -2.185 \times 10^{-19} J = \mathbf{1.365\ eV} \tag{3.4.15}$$

U_{Des} was calculated to be 1.365 eV, and $\nu = 0.11 \times 10^{10}$ Hz as shown in figure 3.23.

The U_{Des} and ν values yield realistic results and notably are in very close agreement with the previous experiment, further solidifying the obtained results. The fit for the second experiment however is not as robust as the first experiment, and uncertainties even larger than the nominal value were calculated for U_{Des}. A noteworthy comment when comparing both experiment results for τ_{Des} at T_{Sub} = 485 °C exhibit substantial difference (1.55 vs. 0.8512) seconds, indicating there could

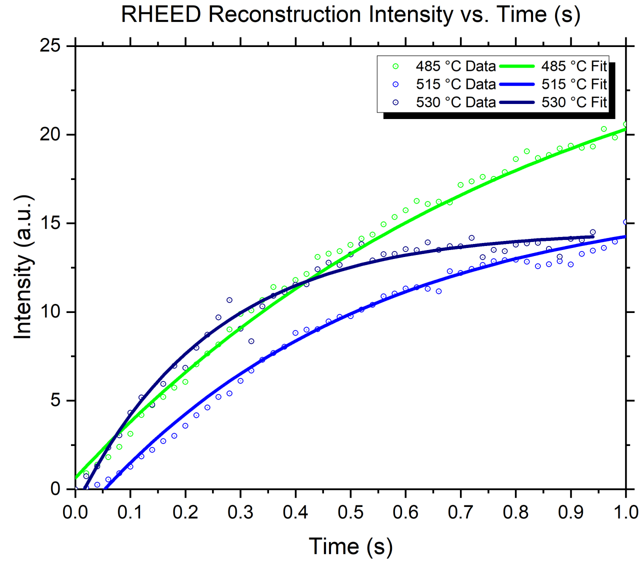

Figure 3.22: Reappearing RHEED streak intensity data fitted with exponential equation in order to extract τ_{Des}. Quick initial rises are used. R^2 = 0.996, 0.9906, 0.9814 for 485, 515, 530 °C respectively.

be a large degree of experimental error. This could possibly be due to inaccuracies in specifying, maintaining, or measuring the temperature across both experiments, or the aforementioned noise in the RHEED intensity signal as a consequence of the PID controller (particularly for the second experiment). It can be concluded that the second experiment, while yielding a remarkably similar value to the first one, is less trustworthy owing to the noise and fewer number of data-points. To ameliorate this, data from both experiments were combined in order to calculate a final combined value for U_{Des} and decrease the uncertainty by increasing the data-points. The fit for the combined data is shown in Figure 3.24, and the final values with the uncertainties are shown in table 3.6, and the final estimate for U_{Des} is found to be 1.74 ± 0.38 eV.

It is also intriguing to compare the obtained values for U_{Des} and ν in light of the expected presuppositions as per the Langmuir model. For the formation of a stable

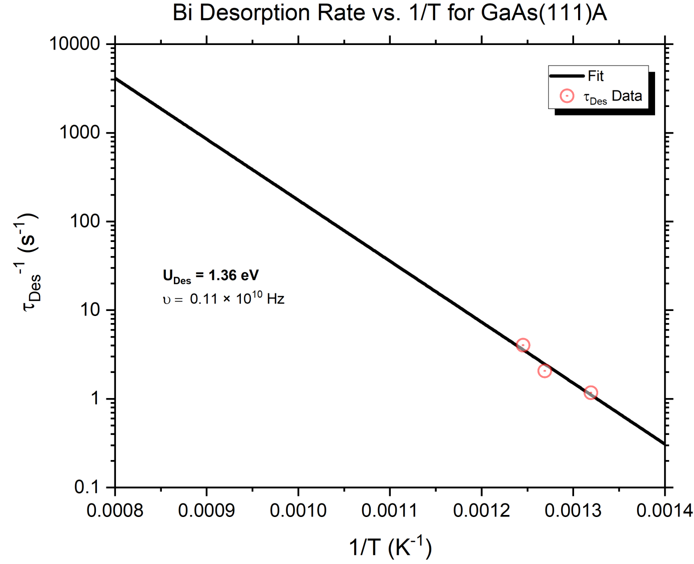

Figure 3.23: Arrhenius plot for second experiment (desorption rate vs. inverse temperature) in order to calculate U_{Des}. $R^2 = 0.93766$.

Parameter	Result
U_{Des}	1.74 ± 0.38 eV
ν	2.75×10^{11} Hz [0.312×10^9 - 2.44×10^{14} Hz]

Table 3.6: Final U_{Des} and ν values from fitting combined data from both experiments with uncertainties (95% confidence bounds).

monolayer as per the model, it is assumed that the adsorbent adatom sticks more strongly to the surface than to other adatoms, allowing for monolayer formation and preventing mound/island nucleation. In light of of the reported self-desorption energy found in the literature for Bi of 1.7 eV[90], the values for the the two experiments (1.407 eV and 1.365 eV respectively) seem like peculiar results, seeing as a Bi monolayer seems to form. However, the combined data value (1.74 ± 0.38 eV) is somewhat inline with expectations, although it is still not unambiguously higher than the self-desorption value. The results that show a value below the self-desorption one could

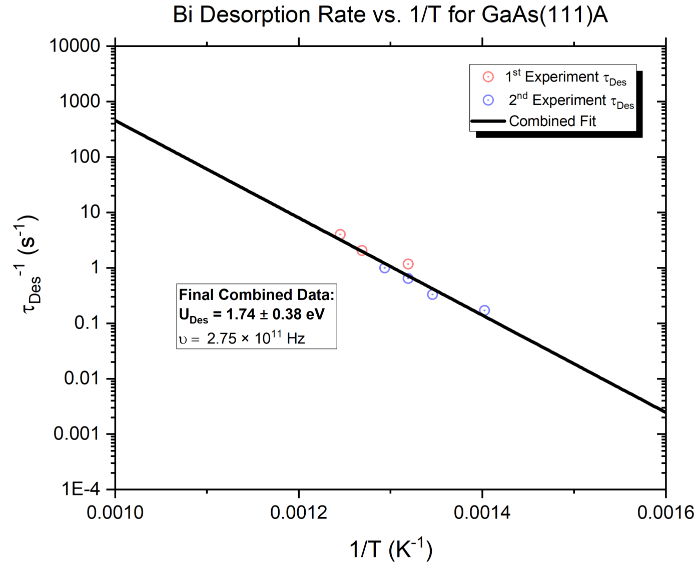

Figure 3.24: Arrhenius plot for combined data from both experiments (desorption rate vs. inverse temperature) in order to calculate U_{Des}. $R^2 = 0.977$.

be interpreted in a number of ways, although in all cases the uncertainty does overlap with the intuitively expected lower limit. It is known that Bi does not incorporate easily into III-V films, losing to As in the competition for group III surface bonding, and specific growth conditions are needed for Bi incorporation, such as the use of high Bi fluxes. It is also apparent form Figure 3.12 that Bi may have adsorbed to Ga surface sites, but desorbed immediately on interruption of the Bi flux, These characteristics suggest a low desorption energy barrier due to a weak Ga-Bi bond and due to the fact Bi tends to segregate on the surface owing to its size[92], and thus gives some credence to the low results obtained. The low attempt frequencies (ν) measured (typically $\approx 10^{12}$ Hz) however are not indicative of an easily desorbing adatom. It is worth bearing in mind that the oscillation could be weak as Bi is a heavy atom. Perhaps the low desorption energy and low attempt frequency counteract each other.

This binding energy can be expected to vary as a result of changing the V/III ratio, with lower ratios encouraging better bonding and incorporation for ratios less than 1[90]. Another possibility is that the activation energy measured is that of a surface reconstruction and not of Bi desorbing, which would explain the low value. In addition, the uncertainty for the measurement was quite large for the two experiments, overlapping with the value of Bi self-desorption.

3.5 Conclusion

In conclusion, in this chapter a procedure was outlined for Bi source calibration, and this source was used to investigate the impact of Bi on GaAs(111)A growth and the behaviour of Bi on the surface. Bi was found to significantly impact the growth and surface dynamics for GaAs(111)A homoepitaxy, radically improving hillock and defect-ridden conventional GaAs(111)A buffer layers by inducing atomically-smooth GaAs(111)A layers with RMS roughness values of as little as 130 pm, which has not been reported before in the literature. Smooth terraces were observed as a result of smooth step-flow growth, thanks to the perceived increase in diffusion length provoked by Bi surfactant action. The effect was enhanced when using greater Bi fluxes, with the ES barrier of GaAs(111)A previously posited to be the cause of the 3D defects in GaAs(111)A possibly responsible for step anti-bunching when using Bi.

In an effort to probe Bi adatom behaviour and dynamics on GaAs(111)A, an experiment was designed using RHEED in order to measure the Bi desorption energy barrier U_{Des} and attempt frequency on GaAs(111)A, which has not been reported yet in the literature. The experiment was conducted twice and yielded very similar results of 1.4 $\pm$ 0.7 eV and 1.365 eV respectively as seen in Figure 3.25, with the

attempt frequency calculated to be 0.14×10^{10} Hz and 0.11×10^{10} Hz respectively. When considering both experiments and the totality of the data, the final values were found to be 1.74 ± 0.38 eV, and $\nu = 2.75 \times 10^{11}$ Hz.

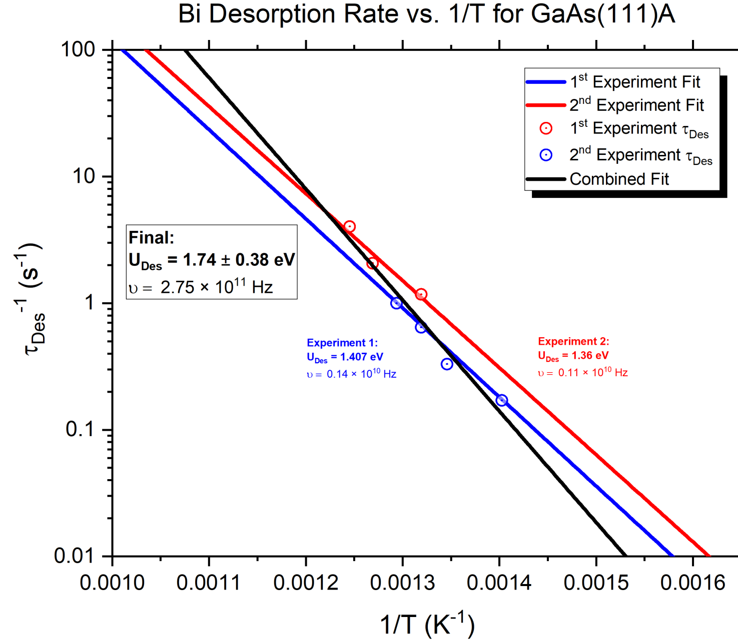

Figure 3.25: Arrhenius plot for both experiments (desorption rate vs. inverse temperature), and for all the combined data, giving the final values.

The results are novel and indeed prove that Bi acts as a surfactant on GaAs(111)A and significantly enhances surface morphologies, with a nominal U_{Des} value a around that of Bi to Bi self desorption energy barrier of 1.7 eV, provoking thoughts of how Bi is covering the surface in the context of the Langmuir model. When taking into account the uncertainty however, the range is somewhat congruent with the assumptions of the Langmuir model.

Chapter 4

MOCVD Growth on GaAs(111)

4.1 Motivation

In this chapter, a preliminary study of growth on GaAs(111) using MOCVD will be presented. The motivations behind exploring the state of GaAs(111) growth using MOCVD were multifold. Firstly, there is a notable lack of research done on Bi and Sb surfactants on non-(100) low index GaAs surfaces when compared to MBE. In addition, MOCVD as previously mentioned is the more viable commercial technique, so it would stand to reason that investigation of the GaAs(111) platform on MOCVD could be a potentially more fruitful one. As mentioned in chapter 1, GaAs(111) homoepitaxial growth using MOCVD has been shown to yield smoother GaAs buffer layers than MBE, with less defects and more favourable surface morphologies[56][57], but MOCVD growth for this substrate in general has been explored to a lesser degree than MBE. Therefore, using MOCVD would bypass the poor surface roughness and morphologies seen in GaAs(111)A MBE growths, and allow for direct investigation of the potential of Bi/Sb surfactants to induce InAs/GaAs(111) QDs. Furthermore, the

delays and restrictions imposed on experimental work as a consequence of the COVID-19 pandemic, coupled with some untimely maintenance issues with the GSMBE system and the Bi effusion cell therein, delayed planned MBE growths and experiments, particularly for MBE-grown InAs/GaAs(111) QDs. These factors all informed the decision to carry out an introductory study on GaAs(111) MOCVD growth. GaAs(111) homoepitaxial buffer layers were grown on both GaAs(111)A and GaAs(111)B (Ga and As terminated surfaces respectively), and the surface morphologies of the growths where characterized using AFM. InAs was also deposited on GaAs(111)B to explore the default growth mode without surfactants. Sb-mediated InAs/GaAs(111) growths (in order to investigate Sb surfactant potential to alter growth modes) were also carried out. Additionally InAs/GaAs(100) QD growths were done using MOCVD for calibration purposes.

4.2 GaAs(111)A homoepitaxy

While GaAs(111) growth in general has not been extensively studied using MBE compared to the (100) orientation, MOCVD GaAs(111) growth has been studied even less[93]. Despite this, relatively smooth GaAs(111) homoepitaxial growth has been demonstrated on MOCVD (unlike MBE) since the 1990s[93][56][57]. GaAs(111)B was found to require very high substrate temperatures ($T_{Sub} \approx 800$ °C) to yield the mirror-like smooth surfaces readily attainable on GaAs(100) at lower temperatures ($T_{Sub} \approx$ 500 °C). Using such temperatures for GaAs (111)B would produce large hillocks and defects. For GaAs(111)A, ($T_{Sub} \approx 600$ °C) is required to obtain reasonable surface morphologies, and deviation from this condition would result in hexagonal hillock microstructures[57]. The GaAs(111)A surface roughness in particular was found to

have a strong dependence on T_{Sub} and AsH_3 partial pressure and thus the V/III ratio, with minimal dependence on growth rate or TMGa flow[56]. It was found that for most V/III and T_{Sub} conditions, large microstructures and hillocks nucleate on the surface, except for a narrow T_{Sub} window intertwined with AsH_3 flow[56]. The morphology is dictated by arsine derivative adsorbates such as AsH and AsH_2. The arsine dissociation is enhanced by the TMGa presence, and As species bond to the Ga-terminated GaAs(111)A surface. TMGa pyrolysis results in $Ga(CH_3)$, where the CH_3^- radical was found to hinder 2D growth. CH_3^- is usually expelled from the chamber by combining with the hydrogen in AsH to leave as methane (depositing As), and this is why large supplies of AsH and hence high arsine partial pressures are needed for 2D growth, along with high temperatures.

Using this understanding gleaned from the literature, optimal GaAs(111)A buffer layer growth conditions were formulated to conduct a test growth. The sample was then characterized using AFM to interrogate surface morphology and to verify if the native buffer layer is smooth enough to support useful quantum nanostructures such as QDs.

The same 2-inch $1/6$ GaAs(111)A "pie" wafer samples referenced in chapter 3 were used, along with the same preparation, cleaving, and cleaning procedures outlined previously. Due to the lack of a 2-inch $1/6$ wafer holder, two cleaved Si(111) 2-inch wafer pieces were used to fill in the gaps in the 2-inch full wafer holder, acting as a makeshift holder/adapter. The sample was loaded first into the load-lock chamber, and the pressure in the system was evacuated to a pressure of 35 Torr. The sample was then transferred to the reaction/growth chamber, with the sample sitting atop a

graphite susceptor. A baking procedure was then conducted at the growth temperature $T_{Sub} = 600$ °C to desorb impurities and remove the native oxide while providing AsH_3 flow to inhibit As escaping the substrate.A H_2 carrier gas flow of 16 $^{l}/_{min}$ was used, with a TMGa bubbler temperature and pressure of -10 °C and 800 Torr yielding a TMGa flow rate of 174 $^{\mu mol}/_{min}$. The growth rate achieved under these conditions was found to be 2.5 $^{\mu m}/_{hr}$ with a V/III ratio of 15 being used. A 150 nm buffer layer was grown.

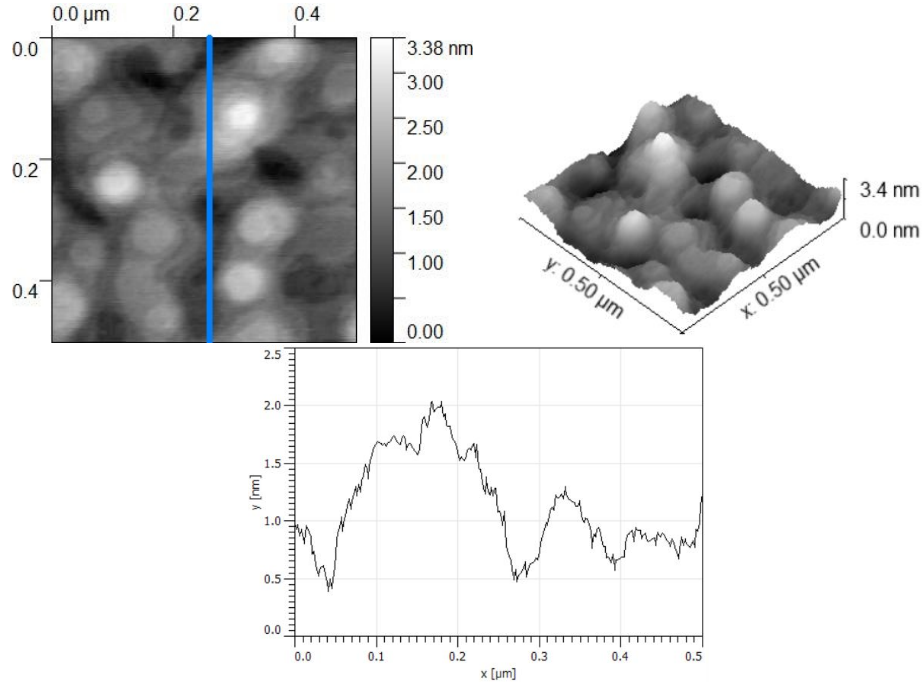

Figure 4.1: AFM scan of GaAs(111)A homoepitaxial buffer layer. 0.5×0.5 μm^2 AFM scan (left), a 3D image of the morphology (right) and the height profile (bottom) for the vertical 0.25 μm line for the GaAs(111)A homoepitaxial growth at $T_{Sub} = 600$ °C and V/III = 15. Sample S24.

While the growth did indeed yield mirror-like surfaces as predicted, it is apparent that upon closer inspection using AFM, as shown by the AFM scans in Figure 4.1 and Figure 4.2, that the surface is littered with small nanostructures. Nevertheless,

the state of the growth on MOCVD is markedly better than that observed previously using MBE as seen in Figure 3.4, with the 1×1 μm growth for MBE having an RMS roughness of ≈ 1 nm as mentioned in chapter 3 versus the roughness value obtained here for MOCVD (0.58 nm) for the same scan size (Figure 4.2).

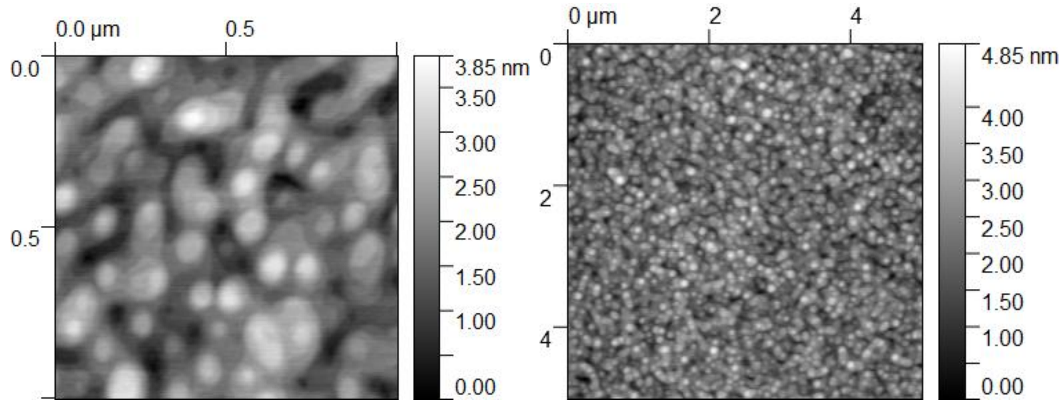

Figure 4.2: AFM scan of GaAs(111)A homoepitaxial buffer layer. 0.5×0.5 μm^2 AFM scan (left) 1×1 μm^2 scan (right) for the GaAs(111)A growth. Sample S24.

Other scan sizes yielded very similar RMS results. The MBE growth contained large hillocks above 12 nm high and large bases, here the nanostructures are smaller, but more numerous. This could be emblematic of a lesser diffusion length for Ga for MOCVD-grown GaAs when compared to MBE-grown Ga. This may be due to metal-organic manifestations of Ga diffusing with more difficulty than elemental Ga in MBE, although the inverse has been posited[94], as it is plausible that the adsorbed metal-organic species are more volatile. Surface reconstructions can also play a role in determining the diffusion length[12]. In addition, it could be argued that faint terraces could be seen to be forming on this surface, even though island nucleation and coalescence is clearly exhibited and dominates the morphology. This is particularly apparent in the upper left corner of the leftmost image in Figure 4.1. An interesting experiment would be the investigation of whether Bi/Sb could be used

to create the atomically-smooth stepped surfaces seen with MBE in chapter 3.

4.3 GaAs(111)B homoepitaxy

Another growth was conducted, this time using GaAs(111)B substrates. Comparing the difference between GaAs(111)A and (111)B growths would provide valuable insight into the influence of differences in Ga/As reactivity on the adatom kinetics. For this growth, the same preparation and loading procedures were used. Similar growth conditions were maintained, apart from the growth temperature, which was increased to $T_{Sub} = 720$ °C and the V/III ratio, which was set to 40.

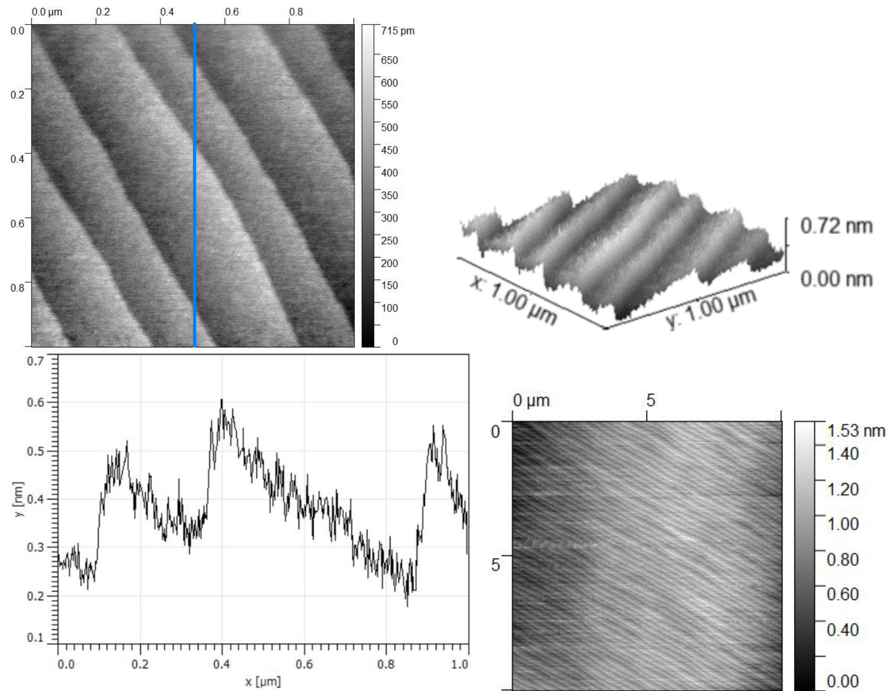

Figure 4.3: AFM scan of GaAs(111)B homoepitaxial buffer layer. 1×1 μm AFM scan (left), a 3D image of the morphology (right) and the height profile (bottom left) for the vertical (blue) 0.5 μm line for the GaAs(111)B homoepitaxial growth at $T_{Sub} = 720$ °C and V/III = 40. The bottom right image shows a 10×10 μm^2 scan of the sample. Sample S26.

As evident from Figure 4.3, atomically smooth steps formed on the surface, with the surface overall having an extremely smooth morphology. The RMS roughness was calculated to be 0.09 nm for the $1\times1\ \mu m^2$ growth, while an RMS roughness of 0.19 nm was measured for the $10\times10\ \mu m^2$, which is significantly lower than for the GaAs(111)A sample. It is interesting to note this morphological transition to step-flow growth for a nominally on-axis substrate in the absence of any external factors or surfactants. It is conceivable that the very small error/offcut angle could be the catalyst behind this observed phenomena. The terrace width and thus offcut angle for this sample is very similar to the angle calculated for the previous samples in chapter 3. The hypothesis positing the emergence of step-flow growth is also buttressed by the fact that very large diffusion lengths have been reported for GaAs($\bar{1}\bar{1}\bar{1}$)B in the literature (as high as 10 μm at $\approx$ 600 °C), with order of magnitude increases over GaAs(100) and much larger when compared to the aforementioned diffusion of ($\approx$ 100nm) for GaAs(111)A MBE-grown surfaces[85]. In light of the very small possible offcut, coupled with the high growth temperature and diffusion length, it is conceivable that a morphological transition to extremely smooth step-flow growth would occur. It is thus concluded that even without surfactants, GaAs(111)B buffer layers are already suitable for SK QD growth.

4.4 InAs/GaAs(100) QD growth

As mentioned in chapter 1, SK QD growth spontaneously transpires on GaAs(100) substrates when depositing InAs above the critical thickness for QD formation for this material system (7.2% lattice mismatch with compressive strain), where this thickness is dependent on the lattice mismatch, and the temperature. In order to calibrate the

In source (TMIn), and to serve as a starting point for future InAs/GaAs(111) QD growth using surfactants, an InAs/GaAs(100) growth was performed using MOCVD. Depositing an InAs layer on GaAs(100) just above the critical thickness should easily yield self-assembled QDs, and thus would confirm successful operation and calibration of the In source. The critical thickness for SK growth under typical conditions for the InAs/GaAs(100) system is around 1.7 ML[95] ($ML_{InAs} = {}^{a_{InAs}}/_{2} = 3.025 \times 10^{-10}$ m). The InAs deposition target was 4 MLs. The structure grown for the QDs is shown in Figure 4.4, with the structure and conditions were informed by optimal QD growth conditions found in the extensive InAs/GaAs(100) QD literature[96][97].

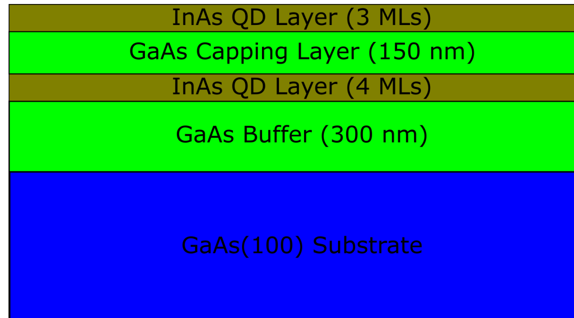

Figure 4.4: Structure grown for InAs/GaAs(100) QDs.

The 2-inch GaAs(100) wafer was cleaved into a square and loaded onto a wafer holder, and the aforementioned loading and preparation sequence was carried out. A TEGa flow of 13.6 ${}^{\mu mol}/_{min}$ was used with a bubbler temperature of 15 °C and a pressure of 800 Torr. The V/III ratio was 83, and a baking procedure was done at 800 °C for 5 minutes under AsH_3 flow. The buffer layer growth was carried out using a two-step methodology, with the growth starting at T_{Sub} = 650 °C for the buffer layer growth before decreasing to 500 °C pre-InAs deposition in order to not cause In desorption (growth interruption). InAs deposition at 500 °C occurred for 8 seconds to get the required 4 ML deposition with TMIn a flow of 19.4 ${}^{\mu mol}/_{min}$

(bubbler temperature = 20 °C, pressure = 800 Torr). Growth interruptions to alter growth conditions should be as short as possible in order to minimize In desorption and impurity incorporation and form the QDs. Therefore, a short 30 second growth interruption was done before the capping layer and precursor flow was stopped to switch to GaAs deposition for the capping layer. The first step of the capping layer (30 nm) was grown at this temperature, then the temperature was ramped back up to 650 °C for smooth GaAs growth to complete the 150 nm layer, with the temperature decreased back to 500 °C towards the end to repeat the InAs deposition on the cap layer in order to facilitate AFM characterization of the QDs while conserving the capping layer to be used for photoluminescence as a test of optical quality of the QDs.

AFM characterization was conducted for this growth using the Tosca tool, and the results are shown in Figure 4.5. The photoluminescence (PL) spectrum is shown in Figure 4.6. Room temperature PL measurements were conducted using an argon ion laser at 488 nm, and a nitrogen cooled InGaAs 1D array detector was used.

QDs can be conspicuously seen to have formed on the surface, with heights ranging from 5-11 nm. Analyzing the amount of InAs deposited, a threshold mask is applied to all the InAs observed in the 1×1 μm^2 sample and the zero basis volume calculated (Vol_{InAs}). Knowing the thickness of an InAs ML (ML_{InAs}) and the area of the scan, the number of deposited InAs monolayers can be calculated, and this was found to be ≈ 8 MLs.

Recalling that the target InAs deposition was 4 ML, it is clear that there is a large discrepancy in the InAs deposition and thus the control of the TMIn flow. This over-deposition is undoubtedly portrayed in the PL spectrum, as only the GaAs buffer

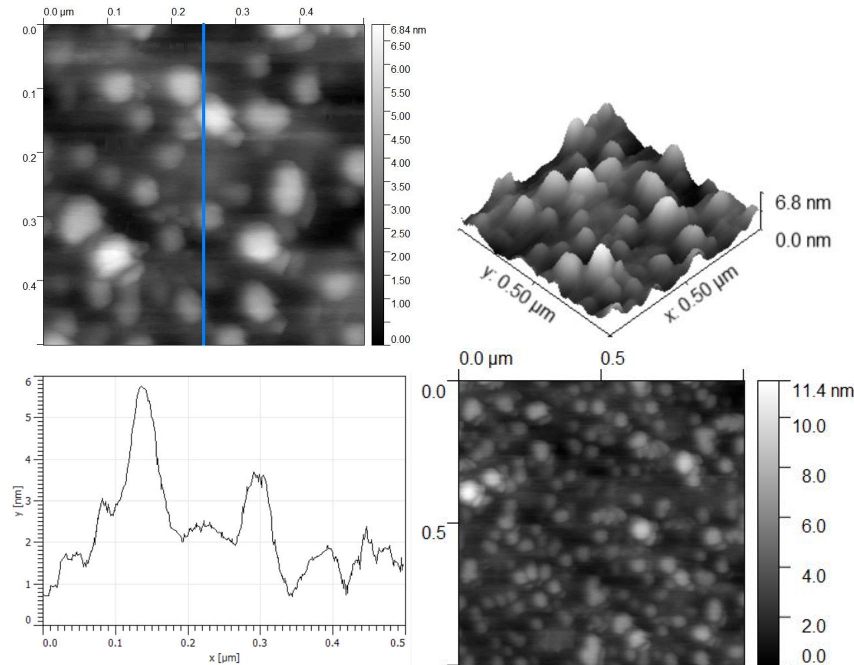

Figure 4.5: AFM scan of InAs/GaAs(100) QDs. 0.5×0.5 μm^2 AFM scan (left), a 3D image of the morphology (right) and the height profile (bottom left) for the vertical 0.25 μm line for the InAs/GaAs(100) QD growth for this scan size. Another scan of the sample (1×1 μm^2) is shown on the bottom right. Sample S33.

layer PL emission is found at $\approx$ 850 nm, with the expected QD emission around $\approx$ 930 nm being notably absent, meaning the QDs are optically inactive. This is very likely due to dislocations plaguing the QDs as a result of increased In flow and thus InAs deposition, meaning that the $\approx$ 8 MLs deposited, while above the SK growth critical thickness as evidenced by the formation of the QDs, is clearly over the critical thickness for dislocations, and the InAs QDs have grown so much in size as to plastically relax under the increased strain. The radiative recombination rate seems to have been severely hindered as to be rendered useless by the traps presented by the emergence of these dislocations.

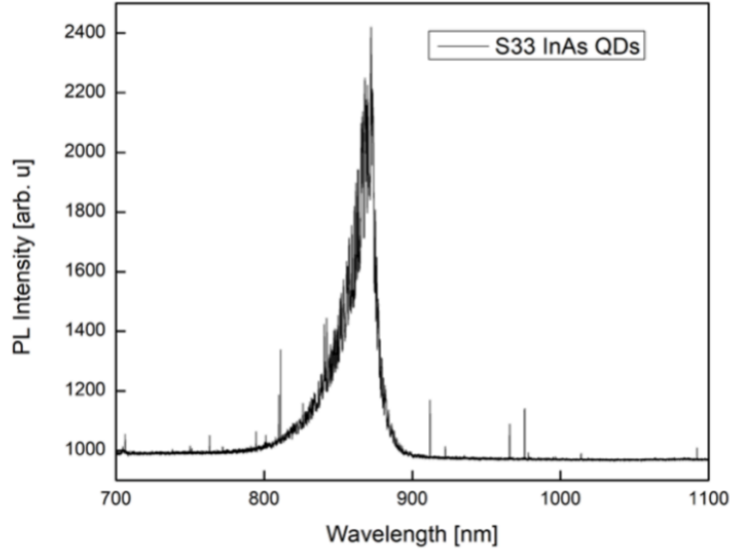

Figure 4.6: PL spectrum for the InAs/GaAs(100) QD sample.

4.5 InAs/GaAs(111)B growth

Before attempting to leverage Bi/Sb surfactants for QD growth on GaAs(111)B, it is important to verify the original growth mode for InAs deposition without surfactants. While this is known to produce plastically relaxed dislocated layers[98][99], it is important to verify this before moving on to surfactant investigation, particularly for GaAs(111)B. InAs deposition was carried out according to the conditions illustrated in the previous section ($\approx 8\ ML_{100} \approx 2.5$ nm) was deposited on a GaAs(111)B buffer layer (buffer was grown as per the conditions laid out in section 4.3) after interrupting the growth post-buffer to ramp down T_{Sub} to 500 °C for InAs deposition. It is important to point out that the ML unit is defined differently depending on the orientation. The AFM (Tosca tool) results are presented in Figure 4.7.

Clearly, no QDs were formed despite being safely above the critical thickness for QD formation, at least for the (100) surface, which is the typical InAs/GaAs platform.

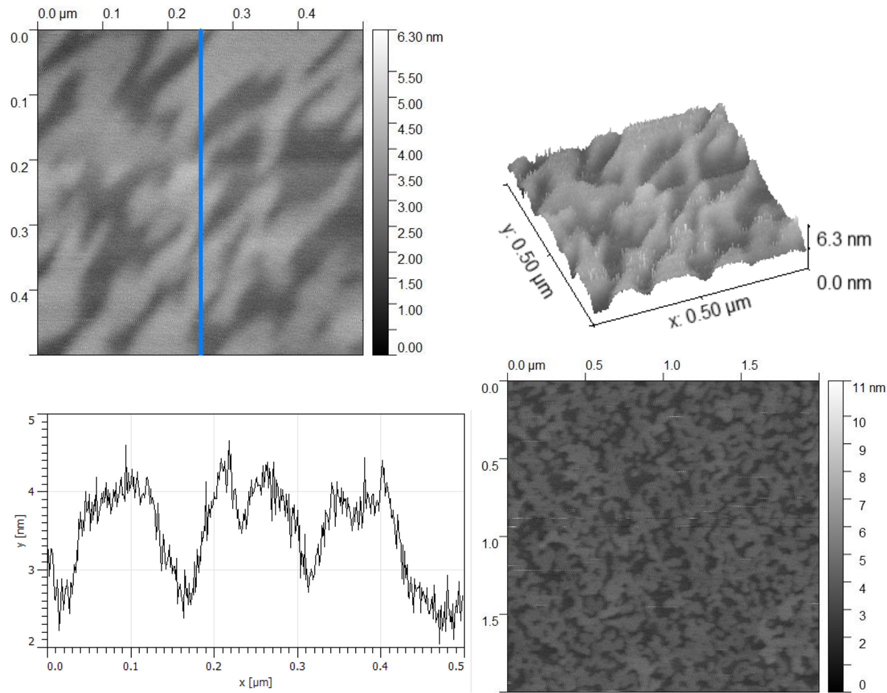

Figure 4.7: AFM scan of InAs/GaAs(111) layer. $0.5 \times 0.5\ \mu m^2$ AFM scan (left), a 3D image of the morphology (right) and the height profile (bottom left) for the vertical $0.25\ \mu m^2$ line for the InAs/GaAs(111)B growth for this scan size. Another scan of the sample ($2 \times 2\ \mu m^2$) is shown on the bottom right. Sample S37.

This confirms the assumption that 2D dislocated growth occurs, with the surface comprising large, flat islands/plateaus. The surface closely resembles the morphologies found in the literature for deposition of InAs on GaAs(111)A[98][99], and for InAs deposition on other non-(100) low index GaAs substrates[63], with an RMS roughness of ($\approx$ 0.615 nm). Thus, the stage is set for novel surfactant investigation for QD formation on the InAs/GaAs(111)B material system.

4.6 Sb-enhanced InAs/GaAs(111)B growth

In light of the results of the previous growth, two growths were conducted with Sb to gauge its effect on the morphology. Before using Sb, it is crucial to be mindful of the growth conditions as Sb incorporates more readily than Bi when used as a surfactant. The same growth shown in the previous section was repeated, but once with a 4 second TMSb flux = 72 $^{\mu mol}/_{min}$ pre-InAs deposition procedure (after buffer layer growth) and another identical one but with the TMSb flow maintained for the duration of the InAs deposition. Sb has been employed as a surfactant with similar growth conditions for InAs/GaAs(100), thus avoiding incorporation[51]. InAs deposition is identical to the previous growth, above the critical thickness. These will be named growth A and growth B for simplicity. The bubbler temperature and pressure for TMSb were 0 °C and 800 Torr respectively. The resultant surface morphologies are presented in Figure 4.8 for growth A and Figure 4.9 for growth B after using AFM (Tosca tool).

The morphology is noticeably different when compared to Figure 4.7. There is a clear tendency to form large 3D triangle-like (3 and 6-sided) structures (particularly for growth B) instead of generally rough 2D surfaces. The triangular structures are quite reminiscent of typical of structures grown on (111) surfaces[13] (which was only recently achieved in that instance by growing GaAs on InAlAs/InP(111)). These structures tend to be symmetric (e.g. equilateral triangles) due to the highly symmetric GaAs(111) surface and thus the isotropic diffusion on the surface[12]. As the structures are more triangular and pronounced for growth B, it is conceivable that Sb is promoting this morphological transition as growth B utilizes Sb for the whole growth as opposed to pre-growth. Sb could be promoting this 3D growth transition, and the short 4 second pre-InAs deposition of Sb may not have been enough to

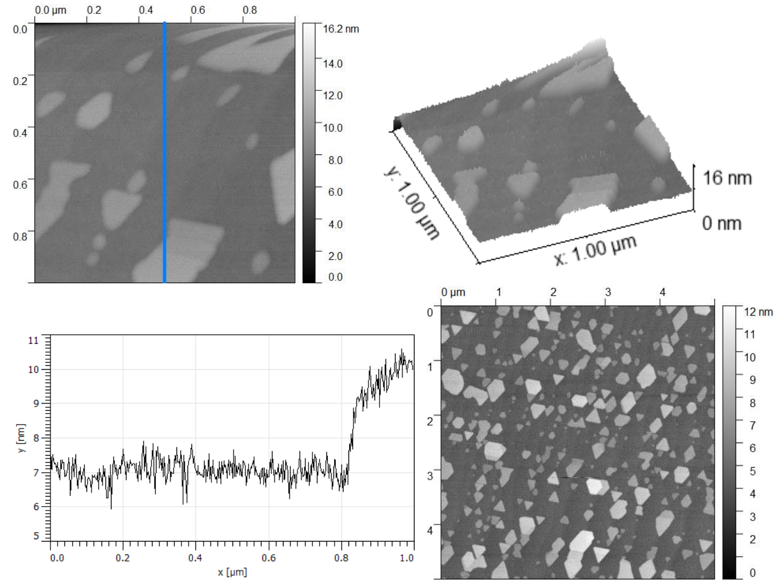

Figure 4.8: Sb:InAs/GaAs(111)B (Growth A): 1×1 μm AFM scan (left), a 3D image of the morphology (right) and the height profile (bottom left) for the vertical 0.5 μm line for this scan size as shown by the blue line. Another scan of the sample (5×5 μm) is shown on the bottom right. Sample S46.

saturate the surface. Having said this, the structures are huge in comparison with expected QD dimensions[38], with some spanning hundreds of nanometres at the base, an order of magnitude larger than expected. These are most likely coalesced, plastically relaxed, non-coherent nanostructures that perhaps started to nucleate as QDs, but rapidly grew into larger plateaus. This is indicative of excessive InAs deposition above the critical thickness for dislocations (plastic relaxation), casting aspersions on the calibration of the In deposition/TMIn flow. It is possible that more than the prescribed 4 MLs of InAs are being deposited. Nevertheless, the fact that Sb is driving 3D growth is an encouraging preliminary result for the potential of surfactants to provoke QD formation on (111).

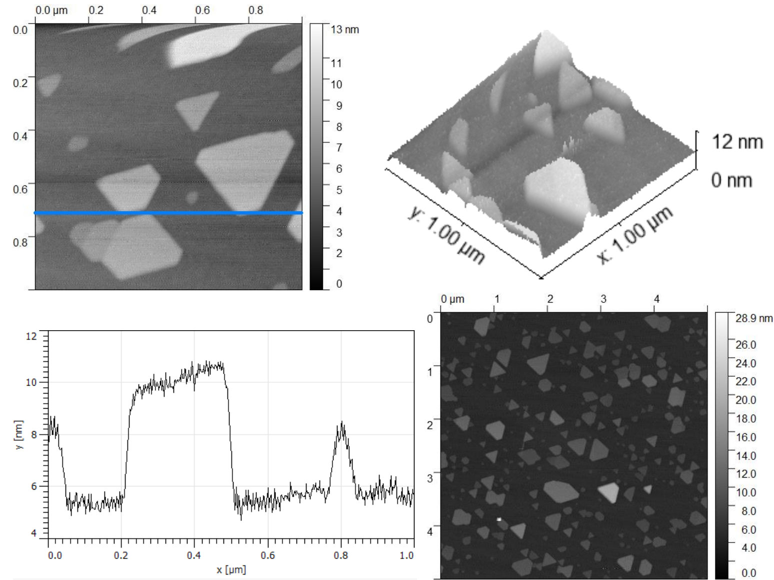

Figure 4.9: Sb:InAs/GaAs(111)B (Growth B): 1×1 μm^2 AFM scan (left), a 3D image of the morphology (right) and the height profile (bottom left) for the horizontal 0.7 μm line for this scan size. Another scan of the sample (5×5 μm^2) is shown on the bottom right. Sample S24.

4.7 Conclusion

In conclusion, this chapter has shown via preliminary growths that MOCVD growth on GaAs(111)B can produce viable buffer surfaces ready to be exploited for use in technological applications, such as QD growth, with the surface exhibiting intriguingly smooth atomic steps and step-flow growth despite being nominally on-axi (without surfactants). GaAs(111)A can be grown to have a mirror-like surface. The surface exhibits atomic scale roughness, and is relatively smooth (more so than MBE-grown surfaces). However, it is not smooth enough for SK growth mode investigation. The roughness could hypothetically be eliminated by the use of Bi/Sb as a surfactant as demonstrated with MBE, opening up the surface for QD investigation. The noticeable difference in GaAs surface morphologies for GaAs(111)A and (111)B could be

down to the difference in reactivity of the surface, and a radically higher diffusion length for GaAs(111)B. InAs was deposited on GaAs(100) and QDs were fabricated following the SK growth mode, and the TMIn flow in the reactor was found to not be calibrated, leading to over-deposition of InAs and hence optically inactive, plastically relaxed QDs. InAs deposition on GaAs(111)B above QD critical thickness was shown to produce plastically relaxed films with large 2D islands without QDs, while simultaneous Sb deposition during InAs/GaAs(111)B growth yielded large 3D structures which could suggest the Sb is inducing 3D growth. These InAs/GaAs(111)B results hint that surfactant use on this surface could cause formation of QDs as shown on other low index GaAs surfaces.

Chapter 5

Modeling of GaAs Quantum Well Photoluminescence

5.1 Motivation

In chapter 3, Bi was shown to be remarkably effective at inducing smooth surface morphologies conducive to technological applications. Extremely smooth GaAs(111) buffer layers could be employed as an ideal platform for defect-free, high quality quantum nanostructures such as QDs and QWs, and allow them to harness the novel properties of GaAs(111), such as its three-fold symmetry (c_{3v})[26]. Additionally, smooth GaAs layers could also be leveraged to fabricate smooth QWs with extremely sharp linewidth luminescence/emission, as will be shown in this chapter. GaAs(111) QWs have also been suggested to have higher PL efficiencies and thus more enhanced optical transitions than their (100) counterparts[100]. QW growths comprising these smooth GaAs layers were planned, with a view to investigate their photoluminescence, but were hampered by equipment shutdowns and delays related to the MBE system,

and the COVID-19 pandemic. Calibration was also needed for standard QW growth on GaAs(100) using the new MOCVD system, meaning comparing grown QW samples to simulated predictions would be of great benefit. Consequently, the promise of this platform, paired with the inability to carry out growths and the need for calibration, motivated an introductory exploration of the simulation of the optical properties and emission of QWs, and strategies and tools for doing so.

For quantum-confined systems and nanostructures such as the aforementioned QWs, it is important to account for several different effects and physical phenomena occurring at the quantum-level in order to obtain accurate results for important properties such as energy level eigenfunction calculations, spontaneous emission etc. In the context of obtaining accurate results for the bandstrcuture and optical properties such as the spontaneous emission rate, these effects often interfere with each other, so it is imperative to examine how these different coupled phenomena can influence nanostructure properties. One of the examples of this is the way the accumulation of carriers, such as electrons or holes, that are quantum confined in semiconductor heterostructures like QWs influence the internal electric field and thus the potential in these systems, affecting the calculation of energy levels. The value of the energy level determines the number of electrons in that level (distribution of carriers depends on Fermi–Dirac statistics), which in turn influences the potential and band profile and thus the energy level, requiring that each energy level be solved in a self consistent manner coupling both the Schrödinger and Poisson equations. Therefore, modeling GaAs QWs using a self-consistent coupled Schrödinger–Poisson solver to account for both phenomena would thus be an important step toward calculating accurate energy level values and interband excitonic transitions for the QW, energy band profiles and

offsets, and carrier densities, which are in turn important for obtaining the optical properties.

In this chapter, these properties will be simulated using a variety of software packages, and the results will be compared and discussed. These results provide a solid theoretical base for future optical investigations of GaAs QWs and calibration of the MOCVD system.

5.2 Theory & methodology

To first solve for the initial electron density $n(x)$ and electron wavefunctions $\psi(x)$ in a potential $E_c(x)$ (conduction band edge) in the quantum well, the Schrödinger equation is invoked to obtain the bound states' wavefunctions, which are subsequently used in conjunction with the density of states of the QW to calculate the carrier density (which is informed by the potential which is informed by the carrier density), constituting a collection of coupled equations as will be elaborated upon in this section.

$$\hat{H}\psi(x) = E\psi(x) = -\frac{\hbar}{2m}\nabla^2\psi(x) + E_c(x)\psi(x) \tag{5.2.1}$$

with $\hat{H} = \frac{\hat{p^2}}{2m} + E_c(x)$ being the hamiltonian, ($\hat{p} = -i\hbar\nabla$ is the momentum operator), m symbolizing carrier mass, and E the energy, ψ the wavefunction. A similar equation can be written for hole wavefunctions using the valence band edge potential $E_v(x)$.

In the context of electrostatics, the Poisson equation is a differential equation describing the electric potential in a static system. The electric potential ($\phi(x)$) (V)

in the presence of a source with a volume charge density $\rho(x)$ (m^{-3}) in a medium of permittivity ϵ is defined as

$$\nabla^2\phi(x) = {}^{-\rho(x)}/_{\epsilon} \tag{5.2.2}$$

$$\rho(x) = q(p(x) - n(x) + N_d(x) - N_a(x) \tag{5.2.3}$$

where q is the elemental charge, $n(x)$ is the electron density, $p(x)$ is the hole density, $N_a(x)$ is the acceptor density, and $N_d(x)$ is the donor density.

These equations rely on the charge density $\rho(x)$ to yield the electrical potential $\phi(x)$ which then influences the band potential E_c or E_v to be used in the Schrödinger equation, altering n etc. The link between $\phi(x)$ and the the band potential $E_{c,v}$ is given as

$$E_{c,v} = E^0_{c,v} - q\phi(x) \tag{5.2.4}$$

where $E^0_{c,v}$ is the flat-band equilibrium starting energy band value.

These coupled-equations feed each other $n(x)$ then $\phi(x)$ then $n(x)$ etc., repeating the process till convergence. The iterative process for electrons in the conduction band is outlined in Figure 5.1 (similar process holds for holes in the valence band)[101]. The iteration begins with carrier density $n^k(x)$ and solving for $\phi^{k+1}(x)$, (where k is the iteration order) using the Poisson equation. The bound states are obtained by way of the Schrödinger equation using $E_c^{k+1}(x)$ from $\phi^{k+1}(x)$. The value of the bound states are needed to find the new carrier densities $n^{k+1}(x)$ based on a density of states

(DOS) calculation as shown in equation (5.2.5)[101].

$$n(x) = \int_{E_{n,0}}^{E_{limit,i}} \sum_{\nu} g_{\nu} \frac{m_{\nu}}{\hbar^2 \pi} \sum_{i} \Theta(E - E_{n,i}) |\psi_{n,i}(x)|^2 f_{FD}(E) \, \mathrm{d}E \qquad (5.2.5)$$

where

$$\Theta(x) = \begin{cases} 0 & x < 0 \\ 1 & x \geq 0 \end{cases} \qquad (5.2.6)$$

$$f_{FD}(E) = \frac{1}{1 + e^{\frac{E - E_f}{k_B T}}} \qquad (5.2.7)$$

Here, g denotes the degeneracy, ν the valley index, $\psi_{n,i}(x)$ is the quasi-bound sate (i) wavefunction and $E_{n.i}$ is its energy. Θ is the Heaviside function and f_{FD} is the Fermi-Dirac distribution (E_f is the Fermi-level) signifying the distribution of carriers. Equation (5.2.5) calculates the carrier density by adding electron densities for all the bound states according to the Fermi-Dirac distribution giving the probability of state occupation, linking the Schrödinger and Poisson equations.

After calculating the the self-consistent potential and energy levels, it is important to calculate the optical properties of the QW. The spontaneous emission rate (A) can be calculated fully quantum-mechanically using the electric dipole moment $q\vec{r}$ for the initial and final states for the transition between energy levels (ψ_i & ψ_f) as calculated previously. The spontaneous emission rate A (s^{-1}) can be defined as[102]

$$A = \frac{\omega^3}{3\pi\hbar\epsilon c^3} \langle \psi_f | q\vec{r} | \psi_i \rangle \qquad (5.2.8)$$

where ω is the angular frequency and c is the speed of light.

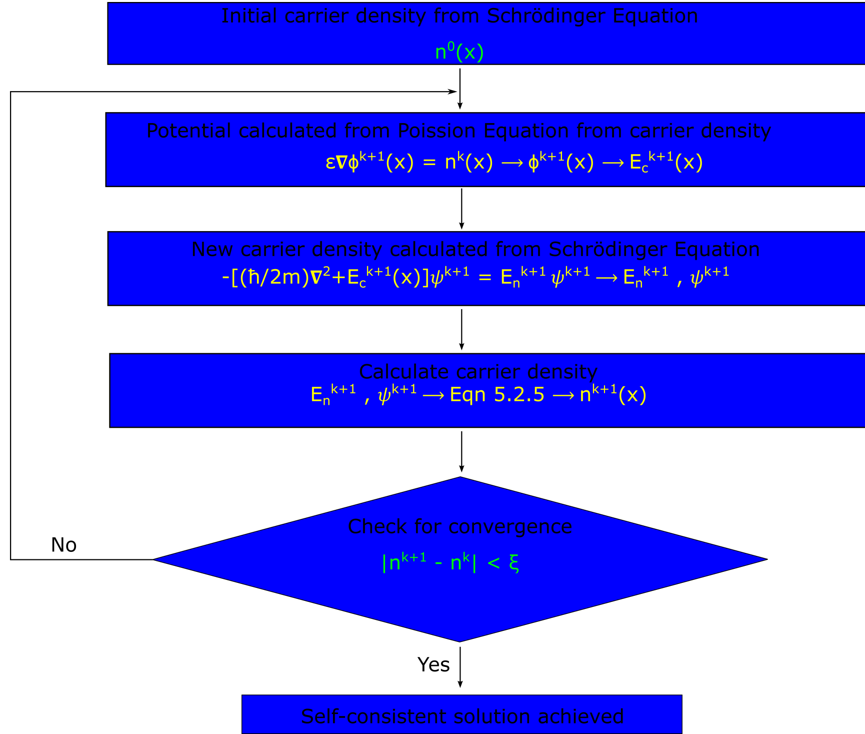

Figure 5.1: Flowchart of how the self consistent Schrödinger–Poisson solver works.

Another important concept/theory to note is k.p theory/formalism, which is also extensively used in solvers to calculate energy dispersion curves and band-structures for the Brillouin zone, and subsequently effective masses important for Schrödinger–Poisson calculations and for taking into account quantum effects[103]. The idea is based on the notion that the potential in a crystalline solid, as semiconductors are, can be modeled as having a periodic lattice potential. Invoking Bloch's theorem in this case considering the 1D Schrödinger equation, the wavefunctions in this instance can be described as Bloch states propagating in the crystal. This can be seen in Equation (5.2.9), and the wavefunction $\psi_{nk}(\vec{r})$ here can be interpreted as "free electron" plane waves modulated by the periodicity of the lattice/crystal. This

periodic function capturing the periodicity of the lattice is given as $u_{n\vec{k}}(\vec{r})$, where n is the band index and k is the wavevector.

$$\psi_{n\vec{k}}(\vec{r}) = e^{i\vec{k}\cdot\vec{r}} \cdot u_{n\vec{k}}(\vec{r}) \tag{5.2.9}$$

Plugging into the Schrödinger equation (Equation (5.2.1)), and applying the hamiltonian to both terms of $\psi_{n\vec{k}}(\vec{r})$

$$\frac{p^2}{2m}u_{n\vec{k}}(\vec{r}) + \frac{\hbar}{m}(k \cdot \hat{p})u_{n\vec{k}}(\vec{r}) + \frac{\hbar^2 k^2}{2m}u_{n\vec{k}}(\vec{r}) +_{n\vec{k}} (\vec{r}) = E_{n,\vec{k}}u_{n\vec{k}}(\vec{r}) \tag{5.2.10}$$

Therefore yielding two "hamiltonian" terms acting on $\psi_{n\vec{k}}(\vec{r})$

$$H_{free} = \frac{p^2}{2m} + \phi \tag{5.2.11}$$

$$H_k = \frac{\hbar}{m}(k \cdot \hat{p}) + \frac{\hbar^2 k^2}{2m} \tag{5.2.12}$$

with H_{free} symbolizing the contribution of the free electron, and H_k symbolizing the effect of the lattice acting as a wavevector dependent hamiltonian of the crystal. This second term is treated perturbatively to solve for the overall energy dispersion and thus the bandstructure at the band edge, allowing the calculation of the effective masses at different points in the bandstrcuture, among other important parameters. The k.p model is a semi-empirical model, and thus uses the value of the energy gap (E_g) (obtained via optical spectroscopy), where the eigenvalues H_{free} are $\pm E_g/2$ for the conduction and valence bands. This formalism will be used in the upcoming

simulations in this chapter.

5.3 QW modeling results

There are several simulation and software packages available with solvers accounting for quantum-mechanical effects, such as the Schrödinger–Poisson solver. Nanohub.org offers a free to use 1D Schrödinger–Poisson solver tool for heterostructures[104] using a variety of options for electron density, including semi-classical, effective-mass, and tight-binding models. GaAs(100) substrates were used in the simulations unless otherwise stated.

The following GaAs/AlGaAs QW heterostructure was simulated (1D) using the tool.

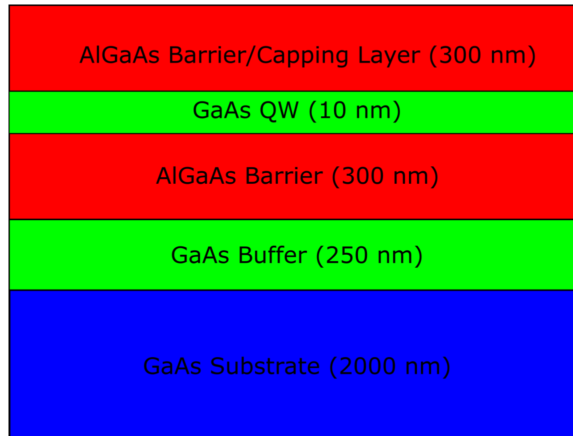

Figure 5.2: Schematic of simulated QW using Nanohub 1D Schrödinger–Poisson solver tool.

The layers were chosen to have a n-type doping concentration of 10^{14} cm^{-3}. The barrier used was $Al_{0.3}Ga_{0.7}As$. GaAs(111) was the substrate crystal orientation. E_f was set to 0.724 eV while the temperature was set to room temperature (300 K).

The other properties used to configure the solver are shown in Figure 5.3, while the results for the self-consistent wavefunction calculations for the conduction band are presented in Figure 5.4. No voltage or bias was applied, so that the structure is simulated at equilibrium, which was done for all following simulations as well.

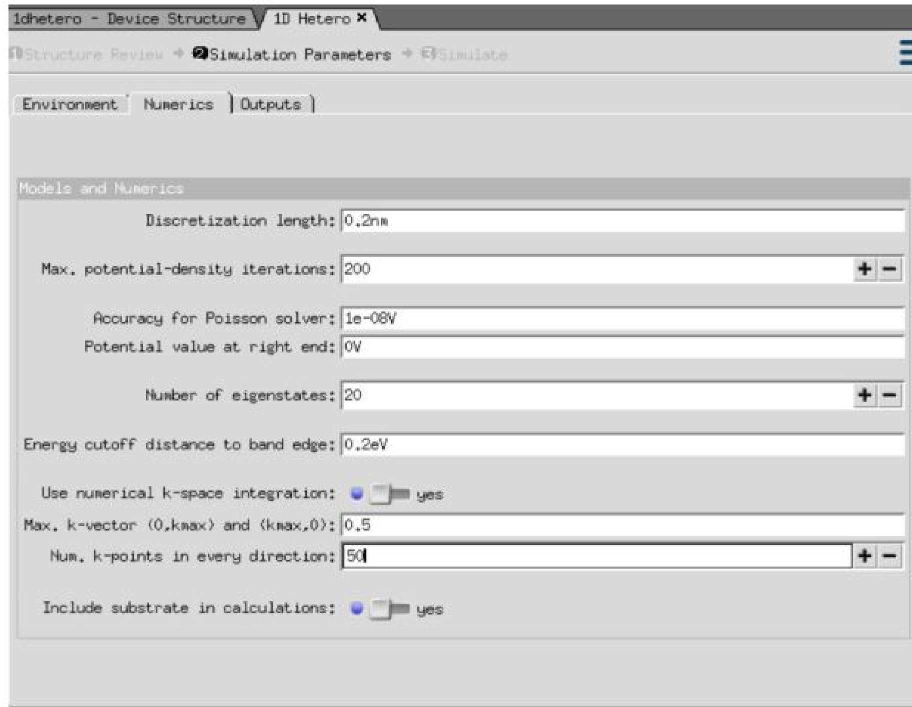

Figure 5.3: Properties for configuring the Nanohub simulation.

Two confined wavefunctions were found for this heterostructure, with the first and second energy states at 1.496 eV and 1.613 eV respectively. The non-confined states shown above are free particle traveling wave states. There is a small degree of energy band profile bending from the built-in field imparted by the carrier density on the conduction band. The electron wavefunctions presented are in line with the results expected from the particle in a box model for QWs. While the tool was successful in calculating the confined states, the tool does not take into account strain and does not

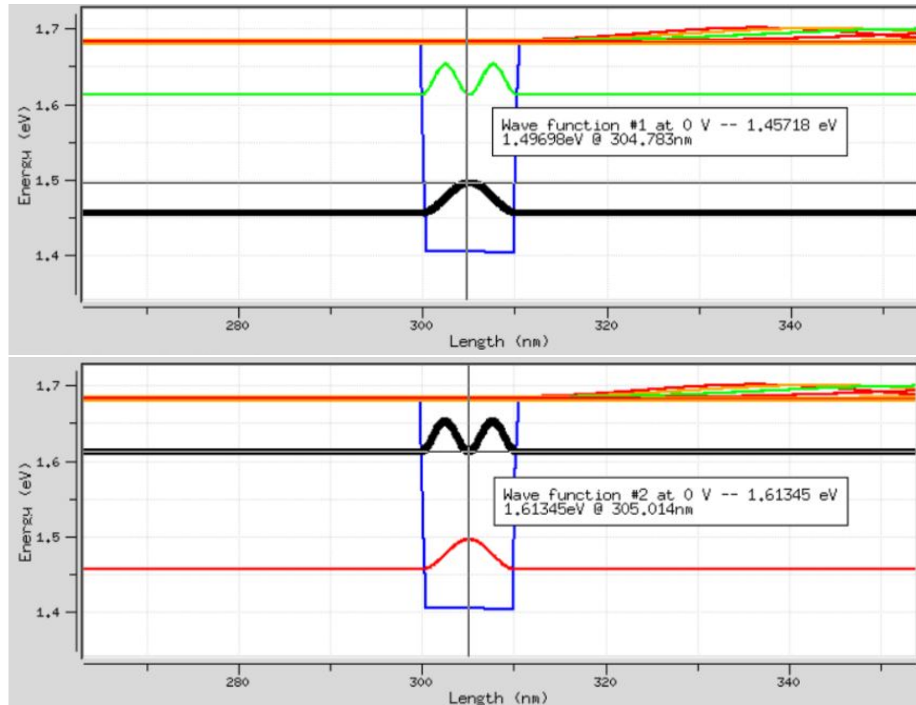

Figure 5.4: Simulated self-consistent energy levels and wavefunctions using Nanohub.

offer optical simulation or calculation of photoluminescence/spontaneous emission.

Another simulation software package was used (tiberCAD)[105], which is a popular multiphysics simulator for quantum nanostructures. The advantage of this software as opposed to the Nanohub tool is the fact that it factors in strain along with the Schrödinger–Poisson solver, along with employing k.p-theory models for bandstructure calculations. An InGaAs QW was considered for this instance, motivated by the fact that AlGaAs growth using the current MBE system was yielding defects and was not suitable as a barrier for a optically active GaAs QWs. For the excitation of a heterostructure, carriers would need to diffuse from the barriers to the heterostructure to combine and yield emission, which would be severely hindered by low quality, defective barriers. The structure simulated using tiberCAD is shown in Figure 5.5.

This particular structure was chosen in order to compare to photoluminescence data already published by Vaccaro et al.[106] for InGaAs/GaAs(111) QWs.

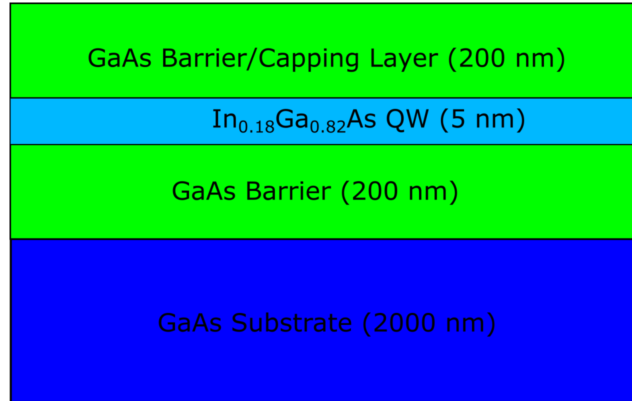

Figure 5.5: Simulated InGaAs QW structure.

The eigenvalues and eigenfunctions were calculated using a single-band effective mass model for the conduction band, and a 6 band-kp model for the valence band. The Poisson equation is solved in order to find the energy band profile with the structure being solved at equilibrium (flat-band conditions). The k.p model is invoked to calculate band edge energies and carrier masses. The stress and strain, which are present as a result of the lattice mismatch between GaAs and InGaAs, is also accounted for and the necessary corrections are made to the k.p theory-calculated bandstructure. The quantum calculations (bandstrcuture, energy level, and eigenvalue calculations) are confined to the InGaAs QW active region and into the GaAs barrier region and are carried out for both holes and electrons. The first 6 eigenstates are calculated for each. The results are presented in Figure 5.6.

Only one confined state was found at 0.641 eV, with the conduction band edge found to be at 0.5918 eV. The Fermi-level is considered to be the reference (0 eV).

The structure (Figure 5.5) was also simulated using the advanced physical models

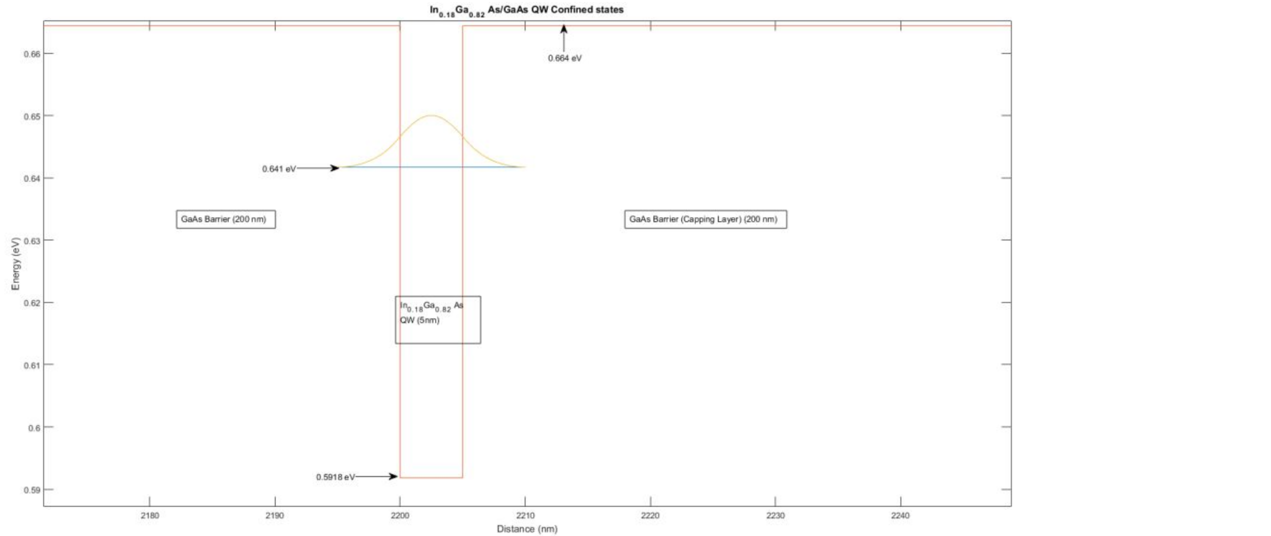

Figure 5.6: InGaAs QW structure simulated wavefunctions and energy levels for the condcution band using tiberCAD.

for semiconductor devices package (APSYS) provided by Crosslight software[107], which can also simulate quantum mechanical effects and bandstructure, strain effects, and also the structure's optical properties, such as the spontaneous emission rate as an estimation of photoluminescence spectrum. The results are illustrated in Figure 5.7. The results shown do not take into account the strain. One confined state was found in the conduction band at 0.64 eV, which is in very close agreement with the tiberCAD results in Figure 5.6. The valence band energy levels and wavefunctions were also calculated and 2 confined states were found at -0.67 eV and -0.73 eV. The Fermi-level (E_f) is at zero eV. The conduction and valence band edges were calculated to be at 0.565 eV and -0.66 eV respectively. Considering the first level electron-hole transition, the energy difference for the transition is around 1.3 eV. Compared to the photoluminescence spectrum data in[106], this is in close agreement with the unstrained peak energy data (1.34 eV), with the strained peak emission

at around 1.42 eV, signifying a blue-shift as a result of compressive strain brought about by the lattice constant mismatch ($a_{GaAs} = 0.565$ nm $< a_{InGaAs} \approx 0.574$ nm at $In_{0.18}Ga_{0.82}As$).

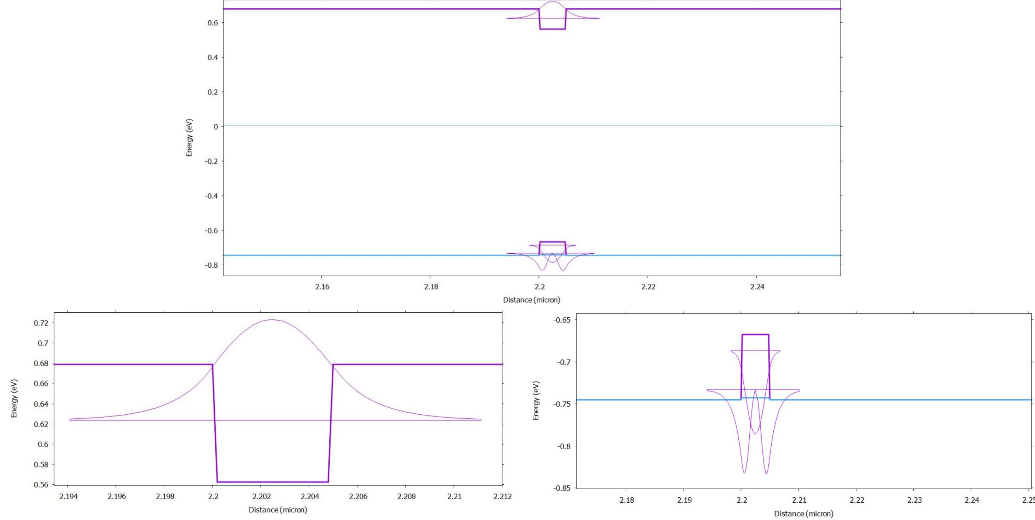

Figure 5.7: InGaAs QW structure simulated wavefunctions and energy levels (top) for both the conduction (bottom left) and valence (bottom right) bands using Crosslight APSYS.

Assuming an RMS interfacial roughness of 0.13 nm as obtained from the Bi 2.4 $^{ML}/_{s}$ MBE growth outlined in chapter 3 and showcased in Figure 3.13, using a smooth GaAs barrier region in an InGaAs QW with a similar interface roughness, the linewidth of the photoluminescence emission can be estimated using the equation[54]

$$dL \approx \frac{L \cdot dE_x}{2(E_x - E_g)} \tag{5.3.1}$$

with dL (nm) denoting the RMS interface roughness, dE_x the broadened linewidth emission, E_g the QW energy gap, and E_x the interband excitonic transition. The width of the excitonic transition (and thus emitted linewidth) can be directly mapped to the inhomogeneous spectral broadening caused by the changes in potential from

the roughness, inducing changes in excitonic binding energy (E_{bex}), the confinement energies for the holes/electrons (E_c, E_h) (eV), and the bandgap. The energy of the transition is given as

$$E_x = E_g + E_c + E_h - E_{bex} \quad (5.3.2)$$

A detailed discussion encompassing Equations (5.3.1) and (5.3.2) can be found in[108][109], and Equation (5.3.1) has been empirically verified in[54].

Using $E_g \approx = 1.225$ eV, $E_x = 1.3$ eV, $dL = 0.13$ nm, the linewidth dE_x was found to be 3.9 meV, corresponding to around 2.8 nm at 950 nm, the peak wavelength for the interband excitonic transition. This is an improvement over the smoothest QWs grown on GaAs(111)A (4.5 meV)[54].

The rate of spontaneous emission was also calculated using Crosslight APSYS (Figure 5.8). A range of carrier densities (20) were used to model excitation of the structure (0.5×10^{15} to 10^{25} cm^{-3}). The results are for room temperature photoluminescence. The peak wavelength was shown to be constant at around 950 nm (1.305 eV), which is equivalent to the first electron-hole transition discussed previously (interband excitonic transition). Intensity also increases with carrier density. It is interesting to note the absence of a blue-shift with increased electron densities, which usually occurs as a result of conduction band-filling at high excitations, with carriers occupying higher energy levels in the step-like QW density of states. It has been reported that the sizable blue-shift exhibited at higher excitations is usually intensified due to potential fluctuations as a result of interface roughness, and alloy disorder (e.g. In fluctuations)[110]. At lower excitations, only the well confined excitons contribute to the emission (lower energy) and as the excitation increases,

access to higher level bound excitons and eventually free excitons is granted, causing the blue shift, and it is understandable how this would be amplified by strong interface imperfections in alloy composition and interface roughness, causing the band profile to fluctuate and creating bound states at many different energies. Perhaps this phenomena is not evidently manifested in the simulations due to the simulation assuming ideal alloy composition (no fluctuations) and perfectly smooth/abrupt interfaces, leading to uniform confining potentials. However, some blue-shift should still occur for thicker QWs with multiple bound states. There could be a saturation of carriers due to the high excitation[111].

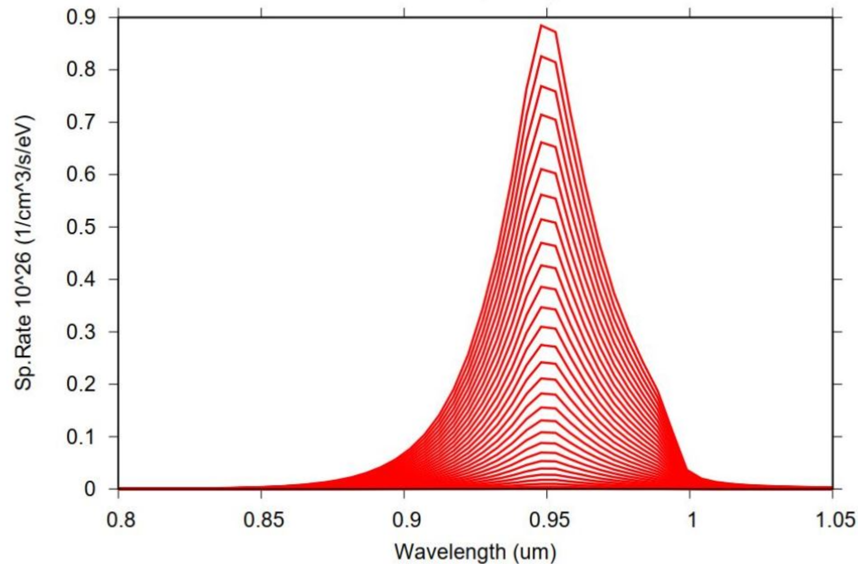

Figure 5.8: Spontaneous emission rate as an estimate of photoluminescence.

Crosslight APSYS was also used to simulate the photoluminescence from AlGaAs/GaAs QWs. A similar structure to the one in Figure 5.2 was used, with $Al_{0.3}Ga_{0.7}As$ barrier layers, and varying GaAs QW widths (3, 5, 10, and 15 nm). The goal was to simulate the red-shift and peak wavelengths as a result of the increasing QW widths, and to compare with photoluminescence from AlGaAs/GaAs QWs

grown using MOCVD to be grown in the future (calibration of MOCVD). Figure 5.9 shows the spontaneous emission rate for the various well widths. Results are at room temperature.

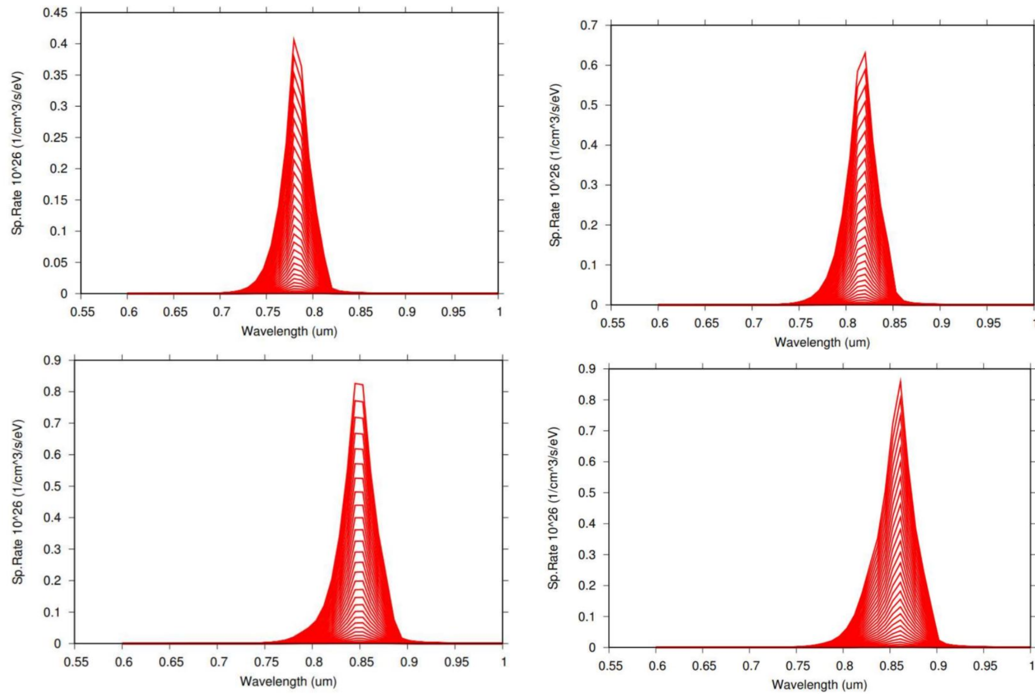

Figure 5.9: Simulated photoluminescence for AlGaAs/GaAs QWs for 3 nm QW (top left), 5 nm (top right), 10 nm (bottom left), 15 nm (bottom right). In the same order, the FWHMs are 25, 25, 40, 40, and 55 nm for the highest excitation curve.

There is a clear red-shift as QW width increases as expected. Intensities climb slightly with well width. In Figure 5.10 photoluminescence from 20 nm QWs at room temperature (300 °K) and low temperature (6 °K) are compared. The linewidth of the low temperature result is clearly significantly lower, owing to the thermal doppler broadening of carriers present at higher temperatures, and the intensity is also increased.

Peak emission energies are plotted for the different QW widths in Figure 5.9 in Figure 5.11.

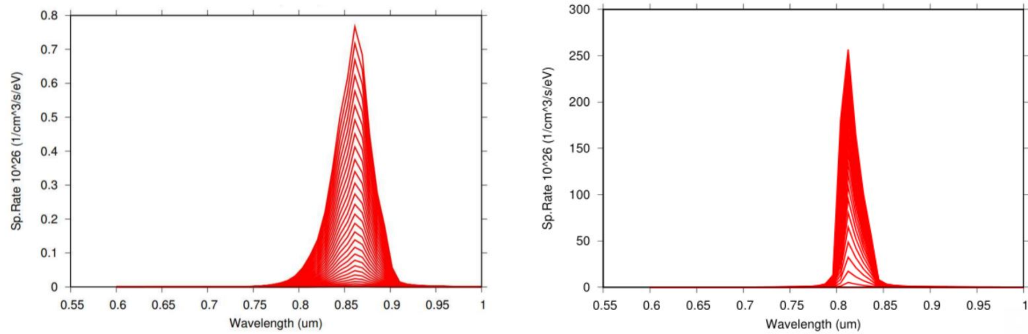

Figure 5.10: Simulated photoluminescence for AlGaAs/GaAs QWs for 20 nm QW for room temperature (left) and low temperature (6°K) (right). The FWHMs are around 45 nm and 22 nm respectively.

5.4 Conclusion

To conclude, in this chapter, the theory and background needed for the accurate modeling and simulation of QWs was presented, including the Schrödinger-Poisson solver, and the k.p formalism for bandstrcuture calculation. Several different QWs were simulated using 3 different software packages and the results were compared. The energy levels and wavefunctions were calculated, as well as the number of confined states. For the optical properties, an expected red-shift in peak emission energy was observed for QWs with larger widths, and linewidths were smaller for low temperature spontaneous emission rate spectra. Finally, an estimation of the QW photoluminescence emission linewidth was made considering the ultra-low RMS roughness obtained with Bi-assisted GaAs(111) layer MBE growths in chapter 3 (0.13 nm), with the linewidth found to be under 3.9 meV, demonstrating very low broadened linewidth emission due to the interband excitonic transition, and thus a low full width half maximum (FWHM) bandwidth for the spontaneous emission rate or photoluminescence spectrum. Finally, the comparison between simulation software and the results for QW emission provide a theoretical basis and guide for tuning and calibration of the

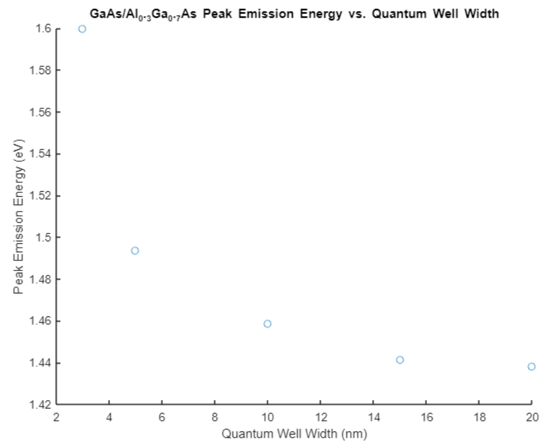

Figure 5.11: Peak emission energies for AlGaAs/GaAs QWs in Figure 5.9 vs. QW widths.

MOCVD growths in the future.

Chapter 6

Conclusion & Future Work

6.1 Summary

GaAs(111) is a remarkably promising platform for a plethora of emerging technologies, most notably for quantum dot (QD) entangled photon sources (due to its c_{3v} symmetry) for use in quantum information applications, but also for spintronics and topological insulators. The promise of this platform has been hampered by the poor quality of its homoepitaxial buffer layer (largely due to the influence of the Ehrlich-Schwöbel (ES) barrier, promoting 3D hillock nucleation), and by its inability to support the Stranski–Krastanov (SK) growth mode for the self-assembly of InAs/GaAs QDs. Surfactants such as Sb and Bi have been used in III-V epitaxy before in order to suppress rough 3D island growth, and have recently been used to induce coherent QD growth on surfaces which do not support them. This makes Bi/Sb surfactant use an enticing prospect for GaAs(111). There is a gap in the current literature regarding the use of surfactants on GaAs(111) and very little work has been done regarding provoking SK QD growth using surfactants. The work in this thesis was carried

out to address this, and has made some novel contributions towards understanding Bi surfactant behaviour on GaAs(111)A surfaces using Reflection High Energy Electron Diffraction (RHEED), and has also yielded some auspicious results pertaining to the growth of smooth GaAs buffer layers on GaAs(111)A using molecular beam epitaxy (MBE), GaAs(111)B layers using Metal-Organic Chemical Vapour Deposition (MOCVD), and the MOCVD-growth of InAs/GaAs(111) QDs induced by Sb.

The main contributions of the thesis can be summarized in the following points

- *Bi acts as a surfactant on GaAs(111):* Through observation and comparison of the surface morphology between GaAs(111)A buffer layer growths with and without a Bi surfactant, it can be confirmed that Bi does indeed act as a surfactant, modifying adatom kinetics then desorbing from the surface.

- *Bi induces atomically-smooth steps for on-axis GaAs(111)A MBE growth:* The morphological transition induced by Bi on GaAs(111)A is one which brings about atomically-smooth (RMS roughness = 0.13 nm) step-flow growth on nominally on-axis substrates, despite the ES barrier on (111) surfaces having been found to drive 3D growth by stifling downward diffusion and allowing upward diffusion on nucleating islands. The effect is further enhanced with larger Bi fluxes. This further expands on a preliminary recent investigation found in the literature. The result is encouraging for GaAs(111)A-based QD growth, (which has previously been elusive) and for quantum well (QW) growth using GaAs(111).

- *Bi may be increasing adatom diffusion on the surface, high Bi fluxes provoke step anti-bunching:* It can be theorized that adatom diffusion may have increased as evidenced by the step-flow growth, and provokes step anti-bunching (terrace

width equalization) at high Bi fluxes. This is posited to be due to the Bi inhibiting the traditional upward diffusion allowed by the ES barrier (as seen in GaAs(111) homoepitaxy) and encouraging adatom incorporation at step-edges. This is also a technologically relevant and novel result which sheds light on how Bi is affecting kinetics on the surface.

- *The activation energy for Bi desorption U_{Des} = 1.74 ± 0.38 eV*: U_{Des} for Bi/GaAs is measured by depositing Bi for a limited time at various temperatures and then fitting the desorption lifetimes (as measured by RHEED intensity changes as the pre-Bi surface reconstruction is restored) on an Arrhenius plot. The desorption barrier was found to be 1.74 ± 0.38 eV, and the attempt frequency was found to be $\nu = 2.75 \times 10^{11}$ Hz [0.31×10^{9} - 2.44 $\times 10^{14}$ Hz]. The result is both novel and intriguing, particularly in light of the Langmuir adsorption model for monolayer formation. The Bi self-desorption energy is 1.7 eV, and the Bi on GaAs(111) desorption activation energy should be higher than this for monolayer formation. The measured value is around the same value, with a sizeable uncertainty of ±0.38 eV, although the final value is nominally above 1.7 eV. It could be that the measured activation energy is for a reconstruction change rather than desorption. More experiments could be conducted to mitigate the large uncertainty and noise from the experiment (addressed in the future work section).

- *Sb could provoke 3D growth for InAs/GaAs(111), paving the way for QDs (MOCVD):* MOCVD was also explored for the growth of GaAs homoepitaxial buffer layers for both GaAs(111)A and (111)B, with GaAs(111)A layers containing nanostructures and being quite smooth overall (RMS roughness = 0.58

nm) but not enough for QD growth, and GaAs(111)B exhibiting remarkably smooth step-edges (RMS roughness = 0.09 nm). InAs/GaAs(111) films yielded plastically relaxed films with no SK growth, providing the pretext for surfactant investigation to induce QDs. Preliminary investigation of InAs/GaAs(111) deposition in the presence of an Sb surfactant show that symmetrical 3D triangular structures appear, hinting that Sb drives 3D growth and could plausibly induce SK growth under the correct conditions.

- *The extremely smooth surfaces are predicted to yield very-sharp emission from QWs:* Finally, GaAs QW modeling was also performed. Simulations for the wavefunctions, bandstructures, and energy levels of GaAs QWs were also investigated, along with an estimation of the photoluminescence (PL) spectrum for calibration purposes. The linewidth PL emission for GaAs QWs based on the ultra-smooth GaAs layers fabricated in the thesis were also estimated to be as little as 3.9 meV, promising ultra-sharp emission.

6.2 Future Work

The work in this thesis has opened up several avenues and lines of enquiry relating to different surfactants (Bi/Sb), for use on different substrates (GaAs(111)A/B), for different purposes (smooth surfaces, QD growth), and using different growth techniques (MOCVD/MBE). Many of these avenues have not been pursued to their fullest extent as a result of the equipment malfunctions and delays brought about by the COVID-19 pandemic. As a result, there are many opportunities for future work and growths for this nascent investigation of surfactants on GaAs(111), with many of these growths

having been already planned. The following avenues could be explored to get a better understanding of the state of the growth and to realize useful quantum nanostructures on this unique surface:

- *Inducing InAs QD growth using Bi and Sb on GaAs(111):* After the investigation and confirmation Bi's ability to induce technologically relevant ultra-smooth steps/surfaces on GaAs(111), the next logical step would be to investigate QD SK growth on MBE and MOCVD via (Bi/Sb) surfactant action on InAs/GaAs(111)A and (111)B. SK growth using surfactants on (111)B has yet to be demonstrated (novel investigation of Sb on this surface was presented in this thesis), and only very preliminary work exists for (111)A. This has been shown for GaAs(110) though using Bi.

- *Inducing smooth surfaces on GaAs(111)A (MOCVD) and GaAs(111)B (MBE) investigation:* The smoothing effect of Bi/Sb on GaAs(111)A using MBE could potentially be replicated with the TMSb in MOCVD growth to create smooth GaAs(111)A surfaces. GaAs(111)B MOCVD-grown surfaces are already smooth and thus present a promising stage for direct investigation of QD growth using surfactants. GaAs(111)B MBE growth with and without surfactants could be explored.

- *Revisiting and increasing confidence in the U_{Des} measurement:* The RHEED Bi desorption experiment for U_{Des} measurement can be redone in several different ways to help solidify the result, decrease uncertainties, and better comprehend how Bi is acting on the surface. The experiment can be done using a Langmuir fit as in the study by Young et al.[90]. Higher temperatures can be used and

the Bi coverage can be deduced from inspecting the RHEED signal intensity (as outlined in subsection 3.4.2), and thus allowing to fit the Langmuir model onto the Bi coverage data, providing another way to measure U_{Des}. This would be problematic however if the film growth turns out to be not following the Langmuir model. Another method would be to deposit different fluxes, and for each flux the temperature would be ramped up from a low temperature guaranteeing full coverage to a higher one (temperature sweep), observing the RHEED pattern. At the temperature which causes the pattern to revert to one indicative of the (2×2) reconstruction (signifying desorption), the temperature is noted and knowing the flux ($^{ML}/_{s}$) one can use it to estimate the desorption rate. For example, if a 2 $^{ML}/_{s}$ flux was desorbed at 500 ° C, this would give τ_{Des} = 0.5 s at this temperature. This method would eliminate issues in RHEED intensity fluctuation due to temperature instability as the RHEED is only relied upon in a qualitative manner in order to signify desorption.

- *Fabricating ultra-smooth, sharp emission GaAs(111)-based QWs:* This has been predicted from the discussion in chapter 5, and hence realizing such state of the art QWs with very smooth interfacial roughness and thus ultra-narrow linewidths would constitute a novel and important result. Smooth GaAs QWs could also be of use in spintronics and as a platform for topological insulators as stated in chapter 1, and GaAs(111) QWs may have more efficient optical transitions as mentioned in chapter 5, meaning that smooth GaAs(111) QWs would be an enticing prospect on several fronts.

- *Modeling of PL emission from rough QWs:* This would pick up were chapter 5 left off, attempting to estimate the PL spectrum and linewidth of QWs with

significant interfacial roughness (representing a GaAs(111) QW grown without Bi). A detailed treatment of characterization of interfacial quality via PL is given in[109]. Rough QWs have been previously modeled in a simple manner, by imagining the overall rough QW as an amalgamation of many QWs with varying widths (w) as seen in Figure 6.1[108]. Assuming a nominal width of w_{QW}, one can assume that there could be an amalgamation of 3 different constituent QWs with 3 different widths comprising the greater QW; $w = w_{QW} + \delta$ (peak), $w = w_{QW} - \delta$ (valley), and $w = w_{QW}$ (flat), where δ is the monolayer thickness for instance. Thermodynamic arguments are invoked to assign probabilities for each of these deviations or mini-QWs to occur and thus concentration of these peak, valley, and flat features[108]. Once this is done each QW can be solved separately to solve for the emission. Obtaining the PL spectrum, this method could be used in reverse to estimate the QW interface quality and shape by fitting the PL spectrum.

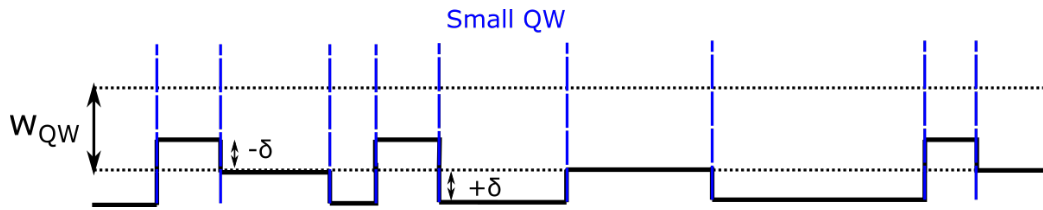

Figure 6.1: An example of a rough QW interface. The large rough QW is divided into many small QWs with varying widths.

Bibliography

[1] I. Mathews, *High-Efficiency Photovoltaics through Mechanically Stacked Integration of Solar Cells based on the InP Lattice Constant*. PhD thesis, Univeristy College Cork, 2014.

[2] C. Bayo and M. Ángel, *Title Theory of elasticity and electric polarization effects in the group-III nitrides*. PhD thesis, University College Cork, 2013.

[3] Surface Explorer version 2, "http://surfexp.fhi-berlin.mpg.de/SXinput.html."

[4] E. M. Sala, *Growth and characterization of antimony-based Quantum Dots in GaP matrix for nanomemories*. PhD thesis, Technischen Universitat Berlin, 2018.

[5] R. B. Lewis, "EP 729: Thin Film Growth and Deposition (Lectures)," 2021.

[6] G. T. Reed, G. Mashanovich, F. Y. Gardes, and D. J. Thomson, "Silicon optical modulators," 8 2010.

[7] T. Kente and S. D. Mhlanga, "Gallium nitride nanostructures: Synthesis, characterization and applications," *Journal of Crystal Growth*, vol. 444, pp. 55–72, 2016.

[8] K. Yung Cheng, *Graduate Texts in Physics: III-V Compound Semiconductors and Devices*. Springer, 2020.

[9] A. Ben-Slimane and E. Dogmus, "GaAs Wafer and Epiwafer Market: RF, Photonics, LED, Display and PV Applications 2020," tech. rep., Yole Développement, 2020.

[10] G. E. Stillman, C. M. Wolfe, and J. . Dimmock, "Hall coefficient factor for polar mode scattering in n-type GaAs*," *J. Phys. Chem. Solids*, vol. 31, no. 1, pp. 1199–1204, 1970.

[11] J. L. Pan, J. E. Mcmanis, T. Osadchy, L. Grober, J. M. Woodall, and P. J. Kindlmann, "Gallium arsenide deep-level optical emitter for fibre optics," 2003.

[12] Y. Nomura, Y. Morishita, S. Goto, Y. Katayama, and T. Isu, "Surface diffusion length of Ga adatoms on (111)B surface during molecular beam epitaxy," *Applied Physics Letters*, vol. 64, no. 9, pp. 1123–1125, 1993.

[13] C. F. Schuck, K. D. Vallejo, T. Garrett, Q. Yuan, Y. Wang, B. Liang, and P. J. Simmonds, "Impact of arsenic species on self-assembly of triangular and hexagonal tensile-strained GaAs(111)A quantum dots," *Semiconductor Science and Technology*, vol. 35, no. 10, 2020.

[14] B. A. Joyce and D. D. Vvedensky, "Self-organized growth on GaAs surfaces," 12 2004.

[15] G. Apostolopoulos, J. Herfort, L. Däweritz, K. H. Ploog, and M. Luysberg, "Reentrant Mound Formation in GaAs(001) Homoepitaxy Observed by ex situ Atomic Force Microscopy," *Physical Review Letters*, vol. 84, no. 15, p. 4, 2000.

[16] B. G. Orr, M. D. Johnson, C. Orme, J. Sudijono, and A. W. Hunt, "The surface evolution and kinetic roughening during homoepitay of GaAs (001)," *Solid-State Electronics*, vol. 37, pp. 1057–1063, 1994.

[17] J. Wu and P. Jin, *Self-assembly of InAs quantum dots on GaAs(001) by molecular beam epitaxy*, vol. 10. 2015.

[18] H. Asahi and Y. Horikoshi, *Molecular Beam Epitaxy: Materials and Applications for Electronics and Optoelectronics Edited*. Wiley, 2019.

[19] O. E. Semonin, J. M. Luther, S. Choi, H. Y. Chen, J. Gao, A. J. Nozik, and M. C. Beard, "Peak external photocurrent quantum efficiency exceeding 100% via MEG in a quantum dot solar cell," *Science*, vol. 334, no. 6062, pp. 1530–1533, 2011.

[20] G. Juska, V. Dimastrodonato, L. O. Mereni, A. Gocalinska, and E. Pelucchi, "Towards quantum-dot arrays of entangled photon emitters," *Nature Photonics*, vol. 7, pp. 527–531, 7 2013.

[21] C. L. Salter, R. M. Stevenson, I. Farrer, C. A. Nicoll, D. A. Ritchie, and A. J. Shields, "An entangled-light-emitting diode," *Nature*, vol. 465, no. 7298, pp. 594–597, 2010.

[22] M. Heiss, Y. Fontana, A. Gustafsson, G. Wüst, C. Magen, D. D. O'Regan, J. W. Luo, B. Ketterer, S. Conesa-Boj, A. V. Kuhlmann, J. Houel, E. Russo-Averchi, J. R. Morante, M. Cantoni, N. Marzari, J. Arbiol, A. Zunger, R. J. Warburton, and A. Fontcuberta I Morral, "Self-assembled quantum dots in

a nanowire system for quantum photonics," *Nature Materials*, vol. 12, no. 5, pp. 439–444, 2013.

[23] V. Le Thanh, P. Boucaud, D. Débarre, and Y. Zheng, "Nucleation and growth of self-assembled Ge/Si(001) quantum dots," *Physical Review B - Condensed Matter and Materials Physics*, vol. 58, no. 19, pp. 13115–13120, 1998.

[24] J. J. Coleman, J. D. Young, and A. Garg, "Semiconductor quantum dot lasers: A tutorial," *Journal of Lightwave Technology*, vol. 29, no. 4, pp. 499–510, 2011.

[25] H. Chen, J. He, and S. T. Wu, "Recent Advances on Quantum-Dot-Enhanced Liquid-Crystal Displays," 9 2017.

[26] R. Singh and G. Bester, "Nanowire quantum dots as an ideal source of entangled photon pairs," *Physical Review Letters*, vol. 103, 8 2009.

[27] H. J. Kimble, "The quantum internet," *Nature*, vol. 453, no. 7198, pp. 1023–1030, 2008.

[28] H.-s. Zhong, H. Wang, Y.-h. Deng, M.-c. Chen, Y.-h. Luo, J. Qin, D. Wu, X. Ding, Y. Hu, P. Hu, X.-y. Yang, W.-j. Zhang, H. Li, Y. Li, X. Jiang, L. Gan, G. Yang, L. You, Z. Wang, L. Li, N.-l. Liu, C.-y. Lu, J.-w. Pan, M. Physics, Q. Physics, I. Technology, and C. Road, "Quantum computational advantage using photons," *Science*.

[29] L. C. Bassett, A. Alkauskas, A. L. Exarhos, and K. M. C. Fu, "Quantum defects by design," *Nanophotonics*, vol. 8, no. 11, pp. 1867–1888, 2019.

[30] Quandela, "https://quandela.com."

[31] A. Schliwa, M. Winkelnkemper, A. Lochmann, E. Stock, and D. Bimberg, "In(Ga)As/GaAs quantum dots grown on a (111) surface as ideal sources of entangled photon pairs," *Physical Review B - Condensed Matter and Materials Physics*, vol. 80, no. 16, 2009.

[32] R. Singh and G. Bester, "Electronic and optical properties of strained InxGa1 -xAs/GaAs and strain-free GaAs/Al0.3Ga0.7As quantum dots on (110) substrates," *Physical Review B - Condensed Matter and Materials Physics*, vol. 88, no. 7, pp. 1–6, 2013.

[33] J. Zhao, C. Ma, M. Rüsing, and S. Mookherjea, "High Quality Entangled Photon Pair Generation in Periodically Poled Thin-Film Lithium Niobate Waveguides," *Physical Review Letters*, vol. 124, no. 16, p. 163603, 2020.

[34] O. Benson, Y. Yamamoto, C. Santori, and M. Pelton, "Regulated and entangled photons from a single quantum dot," *Physical Review Letters*, vol. 84, no. 11, pp. 2513–2516, 2000.

[35] H. Wang, H. Hu, T. H. Chung, J. Qin, X. Yang, J. P. Li, R. Z. Liu, H. S. Zhong, Y. M. He, X. Ding, Y. H. Deng, Q. Dai, Y. H. Huo, S. Höfling, C. Y. Lu, and J. W. Pan, "On-Demand Semiconductor Source of Entangled Photons Which Simultaneously Has High Fidelity, Efficiency, and Indistinguishability," *Physical Review Letters*, vol. 122, no. 11, pp. 1–6, 2019.

[36] J. Treu, C. Schneider, A. Huggenberger, T. Braun, S. Reitzenstein, and S. Ho, "Substrate orientation dependent fine structure splitting of symmetric In (Ga

) As / GaAs quantum dots Substrate orientation dependent fine structure splitting of symmetric In (Ga) As / GaAs quantum dots," *Applied Physics Letters*, vol. 022102, no. 2012, 2013.

[37] M. Gurioli, Z. Wang, A. Rastelli, T. Kuroda, and S. Sanguinetti, "Droplet epitaxy of semiconductor nanostructures for quantum photonic devices," *Nature Materials*, vol. 18, no. 8, pp. 799–810, 2019.

[38] C. F. Schuck, R. A. Mccown, A. Hush, A. Mello, S. Roy, J. W. Spinuzzi, D. L. Huffaker, P. J. Simmonds, C. F. Schuck, R. A. Mccown, A. Hush, A. Mello, S. Roy, J. W. Spinuzzi, and P. J. Simmonds, "Self-assembly of (111) -oriented tensile-strained quantum dots by molecular beam epitaxy," *Journal of Vacuum Science & Technology B, Nanotechnology and Microelectronics: Materials, Processing, Measurement, and Phenomena*, vol. 010801, no. 111, 2018.

[39] H. Q. Ye, G. Wang, B. L. Liu, Z. W. Shi, W. X. Wang, C. Fontaine, A. Balocchi, T. Amand, D. Lagarde, P. Renucci, and X. Marie, "Growth direction dependence of the electron spin dynamics in {111} GaAs quantum wells," *Applied Physics Letters*, vol. 101, no. 3, 2012.

[40] A. Hernández-Mínguez, K. Biermann, R. Hey, and P. V. Santos, "Electrical suppression of spin relaxation in GaAs(111)b quantum wells," *Physical Review Letters*, vol. 109, no. 26, pp. 1–5, 2012.

[41] D. Zhang, W. Lou, M. Miao, S.-c. Zhang, and K. Chang, "Interface-Induced Topological Insulator Transition in GaAs/Ge/GaAs Quantum Wells," *Physical Review Letters*, vol. 156402, no. October, pp. 1–5, 2013.

[42] M. Copel, E. Kaxiras, M. Tromp, and T. Stranski-krastanov, “Surfactants in Epitaxial Growth,” *Physical Review Letters*, vol. 63, no. 6, pp. 632–635, 1989.

[43] C. Y. Fong, M. D. Watson, L. H. Yang, and S. Ciraci, “Surfactant-mediated growth of semiconductor materials,” *Modelling and Simulation in Materials Science and Engineering*, vol. 10, no. 5, 2002.

[44] J. Massies and N. Grandjean, “Surfactant effect on the surface diffusion length in epitaxial growth,” *Physical Review B*, vol. 48, no. 11, pp. 8502–8505, 1993.

[45] U. W. Pohl, *Epitaxy of Semiconductors*. Springer, 2020.

[46] E. Tournié, N. Grandjean, A. Trampert, J. Massies, and K. H. Ploog, “Surfactant-mediated molecular-beam epitaxy of III–V strained-layer heterostructures,” *Journal of Crystal Growth*, vol. 150, pp. 460–466, 1995.

[47] J. C. Harmand, L. H. Li, G. Patriarche, and L. Travers, “GalnAs/GaAs quantum-well growth assisted by Sb surfactant: Toward 1.3 μm emission,” *Applied Physics Letters*, vol. 84, no. 20, pp. 3981–3983, 2004.

[48] M. R. Pillai, S.-s. Kim, S. T. Ho, S. A. Barnett, and S.-s. Kim, “Growth of In x Ga 1 x As / GaAs heterostructures using Bi as a surfactant,” *Journal of Vacuum Science & Technology B*, no. 18, p. 1232, 2000.

[49] P. T. Webster, N. A. Riordan, C. Gogineni, S. Liu, J. Lu, X.-H. Zhao, D. J. Smith, Y.-H. Zhang, and S. R. Johnson, “Molecular beam epitaxy using bismuth as a constituent in InAs and a surfactant in InAs/InAsSb superlattices,”

Journal of Vacuum Science & Technology B, Nanotechnology and Microelectronics: Materials, Processing, Measurement, and Phenomena, vol. 32, no. 2, p. 02C120, 2014.

[50] B. Kunert, R. Alcotte, Y. Mols, M. Baryshnikova, N. Waldron, N. Collaert, and R. Langer, "Application of an Sb Surfactant in InGaAs Nano-ridge Engineering on 300 mm Silicon Substrates," *Crystal Growth and Design*, vol. 21, no. 3, pp. 1657–1665, 2021.

[51] D. Guimard, M. Nishioka, S. Tsukamoto, and Y. Arakawa, "High density InAs/GaAs quantum dots with enhanced photoluminescence intensity using antimony surfactant-mediated metal organic chemical vapor deposition," *Applied Physics Letters*, vol. 89, no. 18, pp. 1–4, 2006.

[52] A. D. Howard, D. C. Chapman, and G. B. Stringfellow, "Effects of surfactants Sb and Bi on the incorporation of zinc and carbo in III/V materials grown by organometallic vapor-phase epitaxy," *Journal of Applied Physics*, vol. 100, no. 4, 2006.

[53] S. Tixier, M. Adamcyk, E. C. Young, J. H. Schmid, and T. Tiedje, "Surfactant enhanced growth of GaNAs and InGaNAs using bismuth," in *Journal of Crystal Growth*, vol. 251, pp. 449–454, 4 2003.

[54] L. Esposito, S. Bietti, A. Fedorov, R. Nötzel, and S. Sanguinetti, "Ehrlich-Schwöbel effect on the growth dynamics of GaAs(111)A surfaces," *Physical Review Materials*, vol. 1, 7 2017.

[55] T. Tiedje and A. Ballestad, "Atomistic basis for continuum growth equation:

Description of morphological evolution of GaAs during molecular beam epitaxy," *Thin Solid Films*, vol. 516, no. 12, pp. 3705–3728, 2008.

[56] S. Fuke, M. Umemura, N. Yamada, K. Kuwahara, and T. Imai, "Morphology of GaAs homoepitaxial layer grown on (111) a substrate planes by organometallic vapor phase deposition," *Journal of Applied Physics*, vol. 68, no. 1, pp. 97–100, 1990.

[57] E. Mao, S. A. Dickey, A. Majerfeld, A. Sanz-Hervás, and B. W. Kim, "High quality GaAs/AlGaAs quantum wells grown on (111)A substrates by metalorganic vapor phase epitaxy," *Microelectronics Journal*, vol. 28, no. 8-10, pp. 727–734, 1997.

[58] X. Y. Chen, Y. Gu, Y. J. Ma, S. M. Chen, M. C. Tang, Y. Y. Zhang, X. Z. Yu, P. Wang, J. Zhang, J. Wu, H. Y. Liu, and Y. G. Zhang, "Growth mechanisms for InAs/GaAs QDs with and without Bi surfactants," *Materials Research Express*, vol. 6, no. 1, 2019.

[59] D. Fan, Z. Zeng, V. G. Dorogan, Y. Hirono, C. Li, Y. I. Mazur, S. Q. Yu, S. R. Johnson, Z. M. Wang, and G. J. Salamo, "Bismuth surfactant mediated growth of InAs quantum dots by molecular beam epitaxy," *Journal of Materials Science: Materials in Electronics*, vol. 24, no. 5, pp. 1635–1639, 2013.

[60] B. N. Zvonkov, I. A. Karpovich, N. V. Baidus, D. O. Filatov, S. V. Morozov, and Y. Y. Gushina, "Surfactant effect of bismuth in the MOVPE growth of the InAs quantum dots on GaAs," *Nanotechnology*, vol. 11, no. 4, pp. 221–226, 2000.

[61] R. B. Lewis, P. Corfdir, J. Herranz, H. Küpers, U. Jahn, O. Brandt, and L. Geelhaar, "Self-Assembly of InAs Nanostructures on the Sidewalls of GaAs Nanowires Directed by a Bi Surfactant," *Nano Letters*, vol. 17, no. 7, pp. 4255–4260, 2017.

[62] R. B. Lewis, A. Trampert, E. Luna, J. Herranz, C. Pfüller, and L. Geelhaar, "Bismuth-surfactant-induced growth and structure of InAs/GaAs(110) quantum dots," *Semiconductor Science and Technology*, vol. 34, 9 2019.

[63] R. B. Lewis, P. Corfdir, H. Li, J. Herranz, C. Pfüller, O. Brandt, and L. Geelhaar, "Quantum Dot Self-Assembly Driven by a Surfactant-Induced Morphological Instability," *Physical Review Letters*, vol. 119, no. 8, pp. 1–6, 2017.

[64] P. Corfdir, R. B. Lewis, L. Geelhaar, and O. Brandt, "Fine structure of excitons in InAs quantum dots on GaAs(110) planar layers and nanowire facets," *Physical Review B*, vol. 96, 7 2017.

[65] R. B. Lewis, "Growth of InAs quantum dots on unconventional GaAs surfaces using a Bi surfactant (Conference Presentation)," in *Quantum Dots and Nanostructures: Growth, Characterization, and Modeling XVI* (D. L. Huffaker and H. Eisele, eds.), p. 6, SPIE, 3 2019.

[66] D. V. Schroeder, *An Introduction to Thermal Physics.* Oxford University Press, 2021.

[67] H. Freller and K. Gunther, "Three-temperature method as an origin of molecular beam epitaxy," *Thin Solid Films*, vol. 88, pp. 291–307, 1982.

[68] L. J. Mawst, H. Kim, G. Smith, W. Sun, and N. Tansu, "Progress in Quantum Electronics Strained-layer quantum well materials grown by MOCVD for diode laser application," *Progress in Quantum Electronics*, vol. 75, no. November 2020, p. 100303, 2021.

[69] J. Matthews and A. Blakeslee, "Defects in epitaxial multilayers," *Journal of Crystal Growth*, vol. 27, pp. 118–125, 12 1974.

[70] E. Shustorovich, *Metal-surface Reaction Energetics: Theory and Applications to Heterogeneous Catalysis, Chemisorption, and Surface Diffussion*. VCH, 1991.

[71] J. Mahan, *Physical vapor deposition of thin films*. Wiley, 2000.

[72] S. Brunauer, P. H. Emmett, and E. Teller, "Gases in Multimolecular Layers," *Journal of the American Chemical Society*, vol. 407, no. 1, 1938.

[73] L. Daweritz and K. Ploog, "Contribution of reflection high-energy electron diffraction to nanometre tailoring of surfaces and interfaces by molecular beam epitaxy," *Semiconductor Science and Technology*, vol. 9, pp. 123–136.

[74] D. A. Woolf, D. I. Westwood, and R. H. Williams, "Surface reconstructions of GaAs(111)A and (111)B: A static surface phase study by reflection high-energy electron diffraction," *Applied Physics Letters*, vol. 62, no. 12, pp. 1370–1372, 1993.

[75] SVT Associates, "https://www.svta.com."

[76] Structured Materials Industries, "https://www.smicvd.com."

[77] S. Nishida, D. Kobayashi, T. Sakurada, T. Nakazawa, Y. Hoshi, H. Kawakatsu, S. Nishida, D. Kobayashi, T. Sakurada, and T. Nakazawa, "Photothermal excitation and laser Doppler velocimetry of higher cantilever vibration modes for dynamic atomic force microscopy in liquid Photothermal excitation and laser Doppler velocimetry of higher cantilever vibration modes for dynamic atomic force mi," *Review of Scientific Instruments*, vol. 123703, no. 2008, 2010.

[78] D. Rugar, H. J. Mamin, and P. Guethner, "Improved fiberoptic interferometer for atomic force microscopy," *Applied Physics Letters*, vol. 2588, no. 1989, 2012.

[79] O. Custance, R. Perez, and S. Morita, "Atomic force microscopy as a tool for atom manipulation," *Nature Nanotechnology*, vol. 4, no. DECEMBER, pp. 803–810, 2009.

[80] Asylum Research, "https://afm.oxinst.com."

[81] Anton-Paar, "https://www.anton-paar.com/corp-en/products/details/atomic-force-microscope-toscatm-400/."

[82] A. Ichiyama and P. Cohen, *Reflection High-Energy Electron Diffraction*. Cambridge University Press, 2004.

[83] Gwyddion, "http://gwyddion.net."

[84] AXT Inc., "www.axt.com."

[85] M. R. Leys, "Fundamental growth kinetics in MOMBE / CBE , MBE and MOVPE," *Journal of Crystal Growth*, no. 209, pp. 225–231, 2000.

[86] A. Tuktamyshev, A. Fedorov, S. Bietti, S. Vichi, R. Tambone, S. Tsukamoto, and S. Sanguinetti, “Nucleation of Ga droplets self - assembly on GaAs (111) A substrates,” *Scientific Reports*, no. 111, pp. 1–11, 2021.

[87] N. V. Sibirev, V. G. Duborvskii, E. B. Arshanskii, G. E. Cirlin, Y. B. Samsonenko, and V. M. Ustinov, “On Diffusion Lengths of Ga Adatoms on AlAs (111) and GaAs (111) Surfaces,” *Technical Physics*, vol. 54, no. 4, pp. 586–589, 2009.

[88] M. Sato and M. Uwaha, “Growth law of step bunches induced by the Ehrlich-Schwoebel effect in growth,” *Surface Science*, vol. 493, no. 1-3, pp. 494–498, 2001.

[89] A. K. Jones, *Kinetically Determined Surface Morphology in Epitaxial Growth*. PhD thesis, The University of British Columbia, 2008.

[90] E. C. Young, S. Tixier, and T. Tiedje, “Bismuth surfactant growth of the dilute nitride GaNxAs 1-x,” *Journal of Crystal Growth*, vol. 279, no. 3-4, pp. 316–320, 2005.

[91] ImageJ, “https://imagej.nih.gov/ij/.”

[92] R. B. Lewis, M. Masnadi-Shirazi, and T. Tiedje, “Growth of high Bi concentration GaAs 1-xBi x by molecular beam epitaxy,” *Applied Physics Letters*, vol. 101, no. 8, pp. 1–5, 2012.

[93] K. Kato, Y. Hasumi, A. Kozen, and J. Temmyo, “AlGaAs epitaxial growth on (111)B substrates by metalorganic vapor-phase epitaxy,” *Journal of Applied Physics*, vol. 65, no. 5, pp. 1947–1951, 1989.

[94] C. T. Foxon, *Semiconductor Interfaces at the Sub-Nanometer Scale.* Springer, 1993.

[95] Y. G. Musikhin, G. E. Cirlin, V. G. Dubrovski, and Y. B. Samsonenko, "The Transition from Thermodynamically to Kinetically Controlled Formation of Quantum Dots in an InAs / GaAs (100) System," *Semiconductors*, vol. 39, no. 7, pp. 820–825, 2005.

[96] K. Kuldova, J. Oswald, E. Hulicius, and J. Humlı, "Photoluminescence and magnetophotoluminescence of circular and elliptical InAs / GaAs quantum dots," *Materials Science and Engineering C*, vol. 26, pp. 983–986, 2006.

[97] A. Hospodkova, E. Hulicius, J. Oswald, J. Pangra, T. Mates, and K. Kuldova, "Properties of MOVPE InAs / GaAs quantum dots overgrown by InGaAs," *Journal of Crystal Growth*, vol. 298, pp. 582–585, 2007.

[98] A. Ohtake and M. Ozeki, "Strain Relaxation in InAs/GaAs(111)A Heteroepitaxy," *Physical Review Letters*, vol. 84, no. 20, pp. 4665–4668, 2000.

[99] H. Yamaguchi, J. G. Belk, X. M. Zhang, J. L. Sudijono, M. R. Fahy, T. S. Jones, D. W. Pashley, and B. A. Joyce, "Atomic-scale imaging of strain relaxation via misfit dislocations in highly mismatched semiconductor heteroepitaxy : InAs / GaAs 111 ... A," *Physical Review B*, vol. 55, no. 3, pp. 1337–1340, 1997.

[100] T. Hayakawa, K. Takahashi, M. Kondo, T. Suyama, S. Yamamoto, and T. Hijikata, "Enhancement in optical transition in (111)-oriented GaAs-AlGaAs quantum well structures," *Physical Review Letters*, vol. 60, no. 4, pp. 349–352, 1988.

[101] W. Gös, *Hole Trapping and the Negative Bias Temperature Instability*. PhD thesis, TU Wien, 2011.

[102] D. Rubin, "Cornell Univeristy, Physics 443: Introduction to Quantum Mechanics (Lectures)," 2008.

[103] P. Yu and M. Cardona, *Fundamentals of Semiconductors: Physics and Materials Properties*. Springer, 4 ed., 2010.

[104] J. M. D. S. S. L. M. P. T. C. K. H.-H. P. S. A. G. K. J. F. A. T. A. G. Akkala, S. Steiger and C.-Y. C. K.-C. Wang, "1D heterostructure tool "https://nanohub.org/resources/1dhetero"," 2015.

[105] M. Auf Der Maur, M. Povolotskyi, F. Sacconi, A. Pecchia, G. Romano, G. Penazzi, and A. Di Carlo, "TiberCAD: Towards multiscale simulation of optoelectronic devices," *Optical and Quantum Electronics*, vol. 40, no. 14-15 SPEC. ISS., pp. 1077–1083, 2008.

[106] P. O. Vaccaro, M. Takahashi, K. Fujita, and T. Watanabe, "Growth by molecular-beam epitaxy and photoluminescence of InGaAs/GaAs quantum wells on GaAs (111)A substrates," *Journal of Applied Physics*, vol. 76, no. 12, pp. 8037–8041, 1994.

[107] Crosslight, "https://crosslight.com."

[108] J. Singh, K. K. Bajaj, and S. Chaudhuri, "Theory of photoluminescence line shape due to interfacial quality in quantum well structures," *Applied Physics Letters*, vol. 44, no. 8, pp. 805–807, 1984.

[109] S. Sanguinetti, M. Guzzi, and M. G. .., *Characterization of Semiconductor Heterostructures and Nanostructures*, vol. 148. Elsevier, 2008.

[110] Y. Wang, X. Sheng, Q. Guo, X. Li, S. Wang, G. Fu, Y. I. Mazur, Y. Maidaniuk, M. E. Ware, G. J. Salamo, B. Liang, and D. L. Huffaker, "Photoluminescence Study of the Interface Fluctuation Effect for InGaAs/InAlAs/InP Single Quantum Well with Different Thickness," *Nanoscale Research Letters*, vol. 12, no. 229, 2017.

[111] R. L. S. Devine and W. T. Moore, "Photoluminescence of InGaAs/GaAs pseudomorphic single quantum wells: effect of excitation intensity," *Solid State Communications*, vol. 65, no. 3, pp. 177–179, 1988.